DOE-ER-0313/32
Distribution
Categories
UC-423, -424

FUSION MATERIALS
SEMIANNUAL PROGRESS REPORT
FOR THE PERIOD ENDING
June 30, 2002

Prepared for
DOE Office of Fusion Energy Sciences
(AT 60 20 10 0)

DATE PUBLISHED: SEPTEMBER 2002

Prepared for
OAK RIDGE NATIONAL LABORATORY
Oak Ridge, Tennessee 37831
Managed by
U.T.-Battelle, LLC
For the
U.S. DEPARTMENT OF ENERGY
Under Contract DE-AC05-00OR22725

FOREWORD

This is the thirty-second in a series of semiannual technical progress reports on fusion materials science activities supported by the Fusion Energy Sciences Program of the U.S. Department of Energy. This report focuses on research addressing the effects on materials properties and performance from exposure to the neutronic, thermal, and chemical environments anticipated in the chambers of fusion experiments and energy systems. This research is a major element of the national effort to establish the materials knowledge base of an economically and environmentally attractive fusion energy source. Research activities on issues related to the interaction of materials with plasmas are reported separately.

The results reported are the product of a national effort involving a number of national laboratories and universities. A large fraction of this work, particularly in relation to fission reactor irradiations, is carried out collaboratively with partners in Japan, Russia, and the European Union. The purpose of this series of reports is to provide a working technical record for the use of program participants, and to provide a means of communicating the efforts of fusion materials scientists to the broader fusion community, both nationally and worldwide.

This report has been compiled and edited under the guidance of Ron Klueh and Renetta Godfrey, Oak Ridge National Laboratory. Their efforts, and the efforts of the many persons who made technical contributions, are gratefully acknowledged.

S. E. Berk
Facilities and Enabling Technologies Division
Office of Fusion Energy Sciences

TABLE OF CONTENTS

1.0 VANADIUM ALLOYS

Modeling of Friction Stir Welding Process for Fusion Energy Applications --
G. Aramayo, B. Radhakrishnan, S. A. David, G. Sarma and S. S. Babu (Oak Ridge National Laboratory)

OBJECTIVE

The objective of the research is to develop a process model for friction stir welding (FSW) to address the issues of coupling between the geometry of the welding tool, heat generation and plastic flow of the material, and the evolution of the material microstructure under the complex thermomechanical loading conditions experienced during welding In particular, the model will be applied to conduct parametric studies on the effect of process parameters and tool speed on the resulting temperature and strain distributions. The model will be applied to investigate optimum process parameters for fusion reactor materials, such as vanadium alloys and dispersion strengthened steels.

SUMMARY

The flow field in the work-piece in the vicinity of the tool during friction stir welding is modeled using two different approaches. In the first approach both the tool and the work-piece are modeled together using an arbitrary Eulerian Lagrangian (ALE) technique. In the second approach the work-piece is modeled separately assuming that it behaves like a viscous fluid. The current limitations in the analysis code DYNA are discussed, and preliminary computational results of flow modeling are presented.

INTRODUCTION

Vanadium alloys are excellent candidate materials for the fusion reactor first wall and the blanket structure due to their inherent low irradiation-induced activity, good mechanical properties, good compatibility with lithium, high thermal conductivity and good resistance to irradiation induced swelling and damage. Fabrication of large vanadium alloy structures for fusion reactor applications requires joining technologies without degrading the above properties. However, for joining technologies such as arc welding, electron beam welding and laser welding processes, the reactive nature of vanadium alloys leads to dissolution of oxygen and hydrogen into the liquid during welding that remain trapped as interstitial solid solution elements. This interstitial solid solution leads to embrittlement of the welds. Although techniques have been recently established to weld vanadium alloys in controlled atmosphere, there is no identified field welding technique for these alloys. Therefore, there is a need to explore an alternate joining technique.

Another potential problem related to fusion reactor materials is the repair welding of structural materials that have undergone excessive radiation damage. This damaged material contains helium bubbles. During arc welding, these bubbles coalesce at weld metal and heat-affected zone grain boundaries, due to stress and temperature gradients. This phenomenon leads to heat-affected-zone intergranular cracking and weld metal cracking. According to the current knowledge, the maximum allowable helium content in structural alloys is limited to ~ 1 appm in order to prevent micro-cracking during arc welding. This severely restricts the maximum allowable fluence for critical components such as the vacuum vessel. Therefore, alternative joining processes need to be considered to eliminate this problem.

One alternative joining process that has great potential is Friction Stir Welding (FSW), a newly developed solid-state joining process for fabrication of butt, lap, and circumferential joints in sheet

and plate material. In this process, the weld is formed by rotating a shouldered tool, that produces sufficient heat and force to move plasticized material to the rear of the joint, creating a dense, pore-free weld zone. Since there is no melting involved in this process, dissolution of gases will be minimal. In addition, due to low diffusivity in the solid state it offers the possibility of "step-change" increase in allowable helium for joining operations.

The interaction between the weld tool geometry and the generation of temperature and flow fields in the weld material are not well understood. Specifically, it is necessary to understand the influence of tool geometry and process parameters on the formation of microstructure and the temperature history of the weld metal. The objective of the proposed research is to develop such a process model.

COMPUTATIONAL MODELING EFFORTS

During the first year of the project, the existing computational resources in the lab were used to explore the possibility of modeling the flow filed and temperature field in the vicinity of the FSW tool. The finite element package LSDYNA was used for this purpose. Two analytical approaches were chosen. The first approach was based on a three-dimensional (3D) Arbitrary Lagrangian Eulerian (ALE) hydrodynamics formulation in which the geometry and kinematics of the FSW process are modeled. The advantage of this technique is the ability to model both the workpiece and the tool simultaneously, so that not only the flow and temperature fields in the work piece but also the stresses and strains and the temperature history of the tool can be calculated. The second approach was based on a computational fluid dynamics (CFD) approach in which the workpiece is modeled as a fluid with temperature-dependent viscosity. Here, the heat-flux and velocities are provided to the tool-workpiece interface as initial conditions, without actually modeling the tool. The advantage here is that it computationally much faster to achieve the steady-state temperature and velocity fields in the workpiece than in the ALE approach.

ALE MODELLING EFFORT

The objective of the modeling effort is to capture the movement of the workpiece material form the front to the back of the rotating tool. In the current version of the analysis program there are several limitations. First, it is not possible to realistically incorporate the temperature field in the analysis of the workpiece deformation. Future versions of the code will have this capability. Therefore, in the initial phase of the research, the applicability of the ALE approach was investigated with several simplifying assumptions. The workpiece was assumed to be at a constant temperature. The material model (based on Johnson-Cook plasticity model) did not include the viscous nature of the workpiece.

The FE model of the workpiece and the tool are shown in fig. 1. In the simulations, the tool was given a rotational and a translational velocity and the velocity field in the workpiece in the vicinity of the tool was investigated. The movement of the material from the front to the back of the tool was also represented as a “volume fraction” map that shows the presence of the workpiece material in an initially void space.

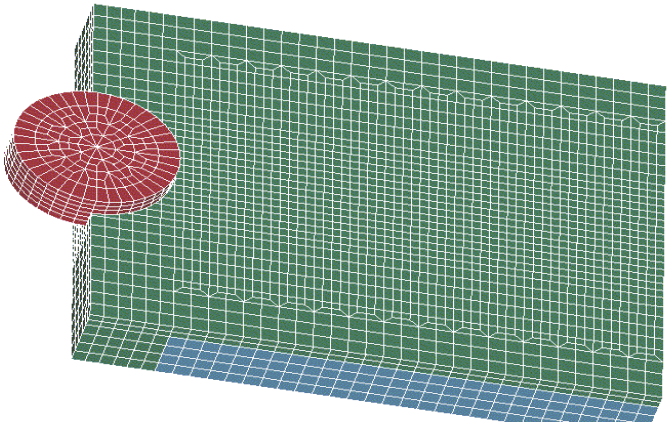

Fig1. Finite element model of the workpiece and the rotating tool.

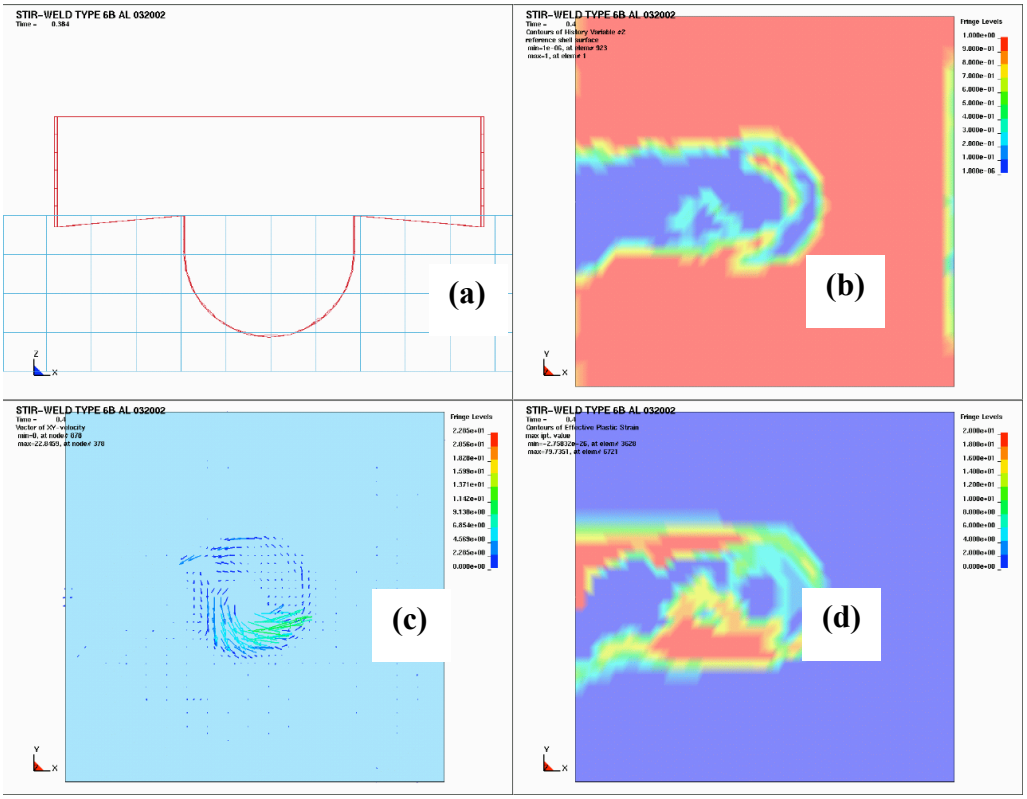

Fig. 2. Computational modeling of the FSW process using the ALE approach showing (a) position of the tool, (b) volume fraction of work piece material (red = full, blue = void), (c) velocity vectors and (d) contour of plastic strain in the workpiece material.

Fig. 2 shows a typical result from the ALE simulations that shows the location of the tool, the contours of volume fraction of workpiece material behind the rotating tool, the flow vectors and the contours of plastic strain. The current effort using the ALE approach will be expanded to real materials incorporating the temperature and flow fields when the newer versions of the analysis package become available. However, the initial results look quite encouraging and the approach is very useful in solving coupled tool-workpiece effects.

CFD MODELING

In this approach the workpiece is treated as a viscous fluid. The velocity boundary conditions are given to the interface between the tool and workpiece, while the tool itself is not explicitly modeled. The objective is to calculate the steady-state velocity and temperature fields in the work piece. Again, there is a limitation in the current CFD version that precludes coupling of the velocity and temperature fields. Therefore, simplifying assumptions were again used, with the objective of exploring the applicability of this technique for modeling FSW process. Fig.3 shows the computed steady-state velocity profile on the top surface of the workpiece when the tool is rotated and translated at the same time. The radial asymmetry in the velocity profile is a function of the ratio of rotational and translational velocities. However, the translational velocity that was used in the current simulations is very small compared to the rotational part. Therefore, significant deviations are not observed. However, the CFD approach provides a fast and efficient way to compute the effect of tool geometry and process parameters on the velocity profile in the workpiece, and will be explored further in the future.

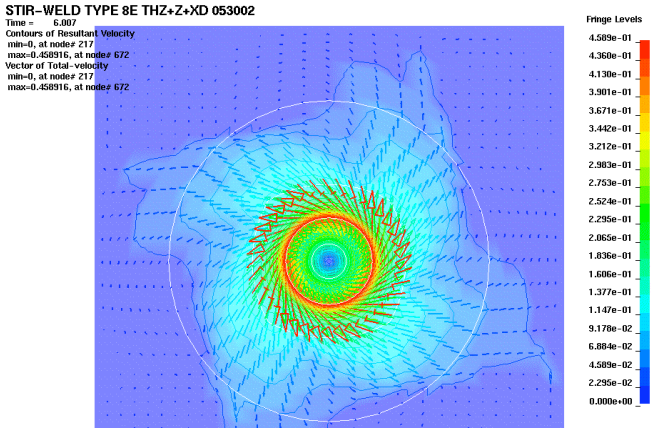

Fig. 3. Computational modeling of FSW process using CFD approach within LSDYNA showing the steady-state velocity profile in the vicinity of a rotating and translating tool.

CONCLUSIONS

The currently available FE analysis packages in the laboratory have been used to model the flow behavior of workpiece material in the vicinity of the rotating and translating FSW tool. Both the ALE and CFD packages currently available with the LSDYNA finite element package can capture the flow fields. However, there are limitations in terms of coupling the flow fields with the temperature fields generated by friction, and in using material models that incorporate temperature dependent stress-strain-strain rate and viscosity effects. Future versions of the analysis package will incorporate these features and will provide the basis for further process modeling activities in order to achieve the objectives set forth in the proposed research.

INVESTIGATION OF THE EFFECT OF A LOW-OXYGEN LITHIUM ENVIRONMENT ON THE CREEP OF THE V-4Cr-4Ti ALLOY–M. L. Grossbeck (Oak Ridge National Laboratory), R. J. Kurtz (Pacific Northwest National Laboratory), L. T. Gibson, and M. J. Gardner (Oak Ridge National Laboratory)

Objective

This investigation is being conducted to evaluate thermal creep behavior in the Fusion Energy Sciences Program reference vanadium alloy, V-4Cr-4Ti, under conditions where the oxygen concentration is not increased during the life of the test. This will allow thermal creep to be separated from irradiation and helium effects in DHCE (Dynamic Helium Charging Experiments) and will aid in interpretation of the vacuum thermal creep experiments now being performed.

Summary

In order to evaluate the effect of decreasing oxygen concentration on creep behavior in vanadium alloys, high temperature pressurized tube specimens of V-4Cr-4Ti were exposed to molten Li and the deformation in the tubes monitored periodically by laser profilometry. It was determined that at 665°C deformations were below 0.05% for all stresses in the range of 59-117 MPa effective stress at 1105 hours and below 6% at 765°C at 1927 hours. However, deformations over 20% were reached at 800°C at times as short as 100 hours for a stress level of 100 MPa and 30% at 457 hours at a stress level of 91 MPa. At all temperatures, it is evident that creep rates are higher in the Li environment where oxygen levels decreased compared to a vacuum environment where the oxygen levels increased.

Experimental Procedures

Specimen geometry and other experimental parameters were chosen to match those of the vacuum environment creep experiment conducted at PNNL [1]. Pressurized tubes were chosen as the specimens for both experiments since they permit testing a large number of specimens covering a wide range of stresses. All specimens at a given temperature can be tested in a single container and furnace. Specimens were fabricated from drawn tubing of V-4Cr-4Ti from Teledyne Wah Chang Heat 832665 [2,3]. End caps of the same alloy were electron-beam welded in place, after which the tubes received an anneal at 1000°C/1h. The tubes initially had a grain size of 10 μm, but following the heat treatment the grain size was expected to double [1]. The internal pressure was attained by sealing a small hole in one end cap with a laser welder while the specimen was in a pressure chamber at the desired pressure of He. The tubes were 25.4 mm in length by 4.57 mm in diameter and 0.25 mm wall thickness.

The specimens were held at test temperature in a retort of TZM alloy with components of Mo and Nb-1Zr in order to contain the high-temperature liquid Li. The retort, has a 25.4 mm diameter Mo tube with caps and flanges of Mo welded in place. The mating flange on top uses a knife edge seal of the ConFlat[1] design with a mating flange of Nb-1Zr for ease of welding a 4 mm Nb-1Zr tube leading to a pressure transducer used to monitor pressure, an indicator of tube rupture. A gasket of Nb-1Zr was used for the flange seal. The retort serves an additional purpose as a prototype containment for a similar proposed test with the addition of tritium to simulate the generation of helium by (n,□) reactions. For this purpose, a quartz tube was added to serve as a barrier to diffusion of tritium. At first, a thermocouple was fastened to the quartz tube in the region of the specimens and the retort placed in a tube furnace. A calibration of the thermocouple was performed by placing a shielded thermocouple directly into the molten Li through a hole in the cap for a short-term test. For the last two intervals, a thermocouple well was incorporated into

[1]Registered trademark of Varian Inc.

the retort cap so that a shielded thermocouple could be placed in the well in contact with the liquid lithium at the level of the specimens.

The entire furnace was situated inside a glove box in a high-purity argon atmosphere. The glove box had a continuously operating molecular sieve/copper purification system to maintain moisture and oxygen below 1 ppm and a Ti-sponge column heated to 850°C to maintain nitrogen below 1 ppm. This atmosphere enabled the specimens to be removed from the Li at a reduced temperature but still molten.

Pressure in the chamber was recorded at 120-300 s intervals to monitor rupture of the tube specimens. Since the retort was sealed, the increase in pressure from a leaking tube remained, producing a step change in internal pressure.

Following removal of the specimens from the Li and subsequently from the Ar atmosphere, the residual Li was removed with liquid anhydrous ammonia, followed by ethanol, followed by water. This sequence was used to prevent contamination by hydrogen [4]. The tubes were then measured by a non-contacting laser micrometer. A helical pattern of 500 measurements was made in the central 12.7 mm of the tubes to a precision of ±250 nm.

Results and Discussion

Pressurized tubes have now been exposed to a vacuum environment and to a lithium environment for a sufficiently long period to make a comparison between high and low levels of oxygen. Results from the Li environment tests are available at a temperature of 665°C for 242 and 1105 hours, at 765°C for 200, 1064, and 1927 hours, and at 800°C for 561 and 1353 hours. Vacuum environment results are available at 700°C for nearly 10,000 hours and at 800°C for over 6000 hours [1]. Results from uniaxial tests made at Argonne National Laboratory on the same alloy and heat are also used for comparison where available at similar test parameters [5]. Results of the Li environment tests appear in Table 1.

Table 1 Creep data in terms of effective stress and strain

Specimen	**Eff. Stress, MPa**	**Effective Strain, %**			
665°C		**242 Hrs**	**1105 Hrs**		
V12	59	.023	.034		
V2	75	.025	.031		
V11	75	.0074	.0022		
V9	83	.027	.040		
V6	100	.022	leaked		
V1	117	-.010	.0044		
V13	133	.014	leaked		
765°C		200 Hrs	**1064 Hrs**	**1927 Hrs**	
V5	25	-.0037	-.017	-.016	
V8	42	.017	.016	.078	
V3	59	.027	.039	.38	
V10	59	.0007	-.016	.36	
V7	75	.033	.13	2.5	
V4	84	.031	.30	5.9	
800°C		**100 Hrs**	**457 Hrs**	**561 Hrs**	**1353 Hrs**
V5	30			-0.0037	0.022
V8	52			0.95	3.3
V3	69			5.6	20.7
V10	69			leaked	
V7	91		30.5*		
V4	100	20.3*			

*Indicates tube failure by creep

Stresses are reported in terms of an effective uniaxial stress and strains are reported as an effective mid-wall uniaxial strain [6]. In cases where negative values of strain appear, the strains were below the limit of experimental error. Such tubes have either failed or have not had sufficient time to creep to a value for which reliable measurements can be obtained. In cases where the tubes leaked due to early weld or defect failures, leakage is indicated in the table. In cases where the tubes failed by creep, an asterisk appears.

Curves of strain as a function of stress for the Li-environment tests are shown in Fig. 1 for 800°C. Results of vacuum-environment tests on similar tubes and of uniaxial specimens are shown for comparison. Expressing strain rate as a power law function of stress,

$$\dot{\varepsilon} = A\sigma^{n} \qquad (1)$$

where $\dot{\varepsilon}$ is the strain rate, σ is the stress, and A and n are constants, a stress exponent in the range of 3-7 is obtained for both the Li and vacuum tests, indicative of diffusion controlled dislocation climb creep. It is clear that the low-oxygen Li-environment test has a higher creep rate than the corresponding vacuum tests and the uniaxial test, although only one datum point is available for the latter. For the case of the Li-environment, creep rate may be expressed as:

$$\dot{\varepsilon} = 0.56\,\sigma^{6.34}\exp(-3.2\text{eV}/kT) \qquad (2)$$

where k is Boltzmann's constant and T is the absolute temperature, for the range of parameters investigated. At low stresses and higher temperatures, the stress dependence becomes linear as diffusional atomic migration creep mechanisms become dominant. This was shown at low stresses in the case of vacuum-environment tests [7]. Difficulty was experienced in expressing all of the data in the present study in the form of equations (1) and (2) because the material was constantly changing in strength properties as oxygen was removed. For this reason and the onset of diffusional creep mechanisms, it is recommended to use the graphical expressions to predict behavior within the range investigated.

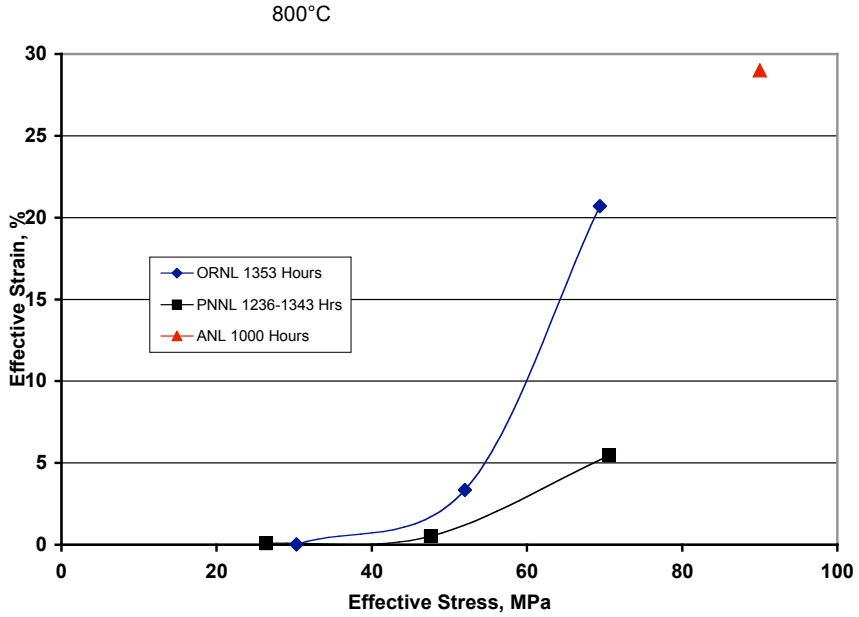

Figure 1 – Effective strain as a function of effective stress for Li-exposed specimens, ORNL. Vacuum-exposed specimens, PNNL and uniaxial specimens, ANL are shown for comparison

Creep response as a function of time is shown in Fig. 2 where curves are again shown for 800°C for stress levels of approximately 50 MPa. The early positive curvature demonstrates a very short period of steady state creep and early onset of tertiary creep. As is characteristic of pressurized tubes, there is little or no observable primary creep in the vacuum test results. For the Li tests, it is not possible to

observe primary creep due to the large deformation exhibited by the first measurement. It is again evident that the Li-environment tests demonstrate a higher creep rate than the higher-oxygen vacuum tests.
Perhaps some uncertainty remains in the interpretation of Fig 2 because the low-oxygen tests were for samples at a slightly higher stress level. In Fig. 3 results are shown for 800°C at an approximate stress level of 70 MPa where the vacuum environment tests are now at the same or slightly higher stress level. However, a higher creep rate is again demonstrated by the Li-environment tests. The very high temperature sensitivity is also shown in Fig. 3 where results from vacuum tests conducted at 700°C and Li-environment tests conducted at 765°C appear.

The observation of higher creep rates for low-oxygen, Li-environment specimens is also true at the lower temperature of 665-700°C. As seen in Fig. 4, the results from Li-environment tests exhibit higher creep deformations despite the lower temperature. In addition, small primary creep is observed for the case of the Li-environment tests.

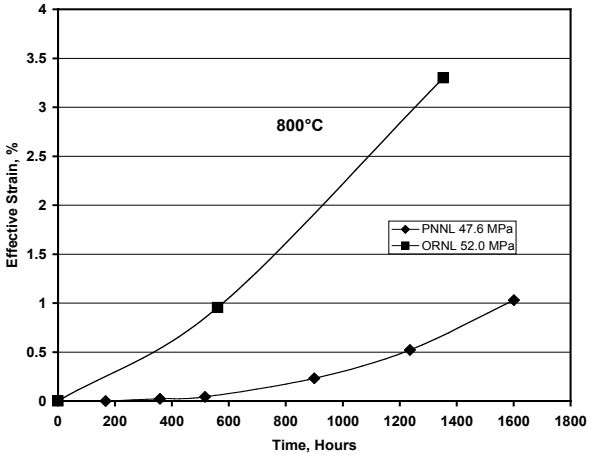

Figure 2 – Creep strain in V-4Cr-4Ti as a function of time showing enhanced creep in a lithium environment, ORNL compared to creep in a vacuum, PNNL.

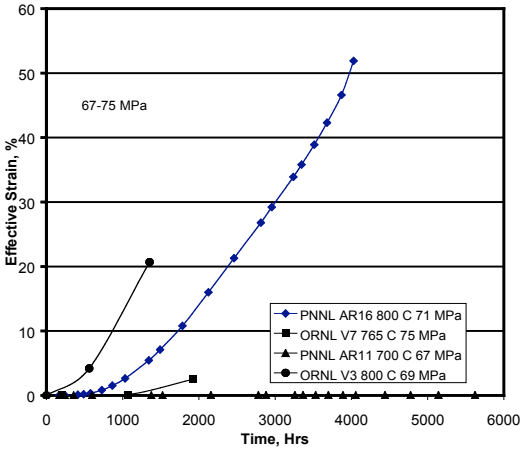

Figure 3 –Creep strain in V-4Cr-4Ti as a function of time comparine a Li-environment, ORNL, with a vacuum environment, PNNL.

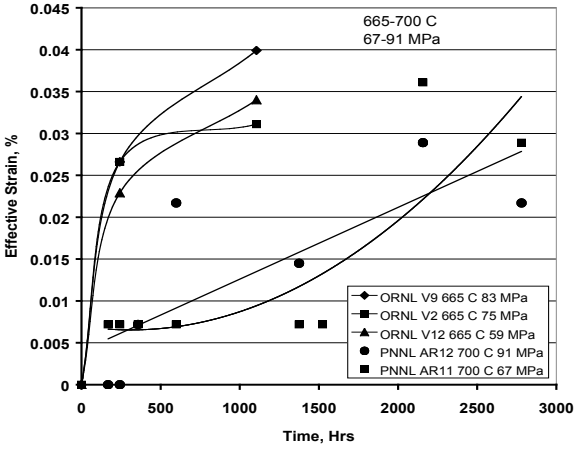

Figure 4 – Creep strain as a function of time for V-4Cr-4Ti at 665-700°C. Curves designated ORNL are for a Li environment, and curves designated PNNL are for a vacuum environment.

Oxygen has also been shown to extend creep rupture life in vanadium alloys [8-10]. In the present study, only two specimens have failed through creep rupture as shown in Table 1. A useful way to display creep rupture is through the Larson-Miller parameter:

$$P = T(\log t_r + 20)/1000 \qquad (3)$$

where T is the absolute temperature and t_r is the rupture time in hours [11]. Effective stress is plotted as a function of the Larson-Miller parameter in Fig. 5 for the two ruptured specimens from the Li-environment study as well as for the ruptured specimens from the vacuum tests. The two Li-environment samples failed prematurely compared with the vacuum-environment samples, as predicted from the previous study [8].

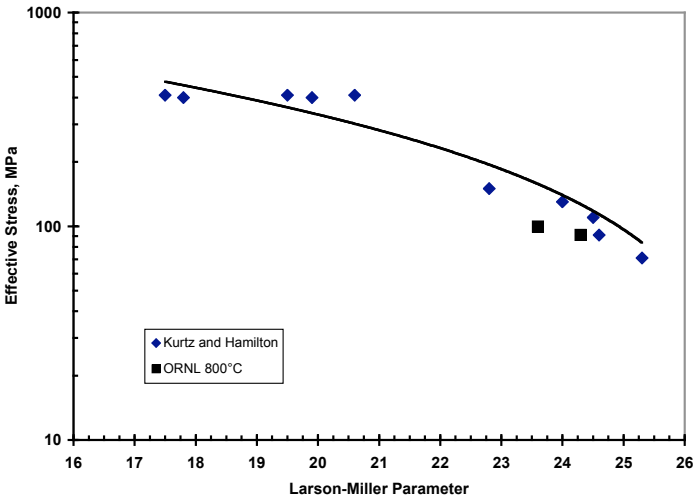

Figure 5 - Plot of effective applied stress as a function of Larson-Miller parameter showing reduced life for V-4Cr-4Ti in a Li environment, ORNL, at 800°C compared to that for a vacuum environment, Kurtz and Hamilton.

The total strain at failure is more difficult to understand. In the vacuum-environment tests at 800°C, a low-stress, long term specimen failed with a strain greater than 50%; shorter term specimens failed with lower strains, but no clear trend was observed. The 20-30% strains observed in the Li-environment tests were within the extremes of the vacuum tests. The absence of a clear trend in strain to failure could be the result of the prevalence of initial defects in portions of the tubing used for the study. Nondestructive tests were used to examine the tubing prior to making specimens, but clearly some defects were missed, and this could introduce some scatter in the results and influence the measured strain to failure.

For vanadium, it can be calculated that Li_2O has a lower free energy than the oxides of vanadium [12]. It then follows that oxygen will partition preferentially in lithium at equilibrium. The distribution coefficients for the lithium-vanadium system have been calculated by Smith and Natesan [12]. For the case of oxygen, the concentration ratio $C_V/C_{Li}=3.8x10^{-7}$, and for the case of nitrogen, $C_V/C_{Li}=186$ for 800°C at equilibrium. Thus, vanadium will be depleted of oxygen to very low levels but will be enriched in nitrogen. These trends are observed in Fig. 6 where it can be seen that the oxygen concentration increases during the vacuum tests but decreases during exposure to lithium. Nitrogen concentrations in vanadium increase slowly for both vacuum and lithium tests as predicted. The rates of change are determined by

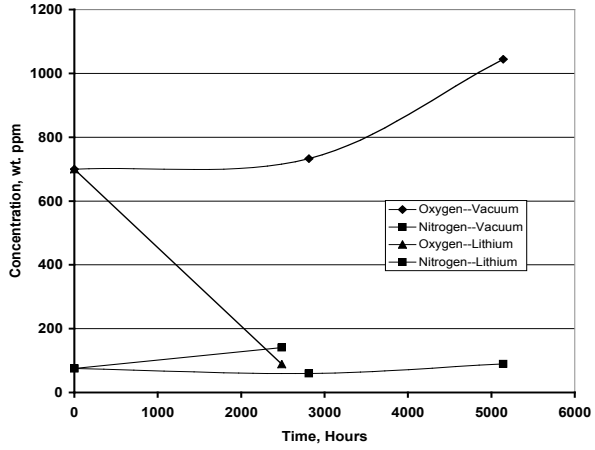

Figure 6 – Measured values of impurity concentration for V-4Cr-4Ti tubing as a function of exposure time.

the diffusivities of the species involved and the rate of impingement of the gases on the samples as well as surface effects and trapping.

This study is part of a larger effort to evaluate the mechanical behavior of vanadium alloys over a wide range of strain rates. Higher strain rates have been explored to study the plastic flow regime [13]. The present study explores the dislocation climb creep regime and the entry into the diffusional creep regime.

FUTURE DIRECTIONS

The higher creep rates and shorter rupture times in a lithium environment have been demonstrated for temperatures of 700 and 800°C. It remains to determine creep behavior in a Li-environment for lower temperatures, especially in light of the rather high creep rates at 800°C. The experiment was performed on the highest quality tubing of V-4Cr-4Ti available; however defects resulting from a heterogeneous microstructure clouded the results, making this a worst case study. Research should continue using tubing that is in preparation using careful control of the microstructure during processing. Testing should also be extended to lower temperatures.

CONCLUSIONS

1. Creep rates in a lithium environment are higher than those experienced in a vacuum environment at 700 and 800°C. This results from the hardening effect of oxygen in solution in the vanadium alloy.

2. Creep failures were observed in a Li-environment at 800°C after 100 hours at 100 MPa and after 457 hours at 91 MPa. These lifetimes are slightly below those expected from the vacuum environment tests.

3. Tertiary creep initiates early, with a short region of steady-state creep.

4. Oxygen concentration increases during exposure to an ultra-high vacuum but decreases in a Li-environment as predicted by thermodynamics. Nitrogen increases in both cases but at a slower rate.

REFERENCES

[1] R.J. Kurtz and M.L. Hamilton, J. Nucl. Mater. 283-287 (2000) 628.
[2] D.L. Smith, H.M. Chung, B.A. Loomis, H.-C. Tsai, J. Nucl. Mater. 233-237 (1996) 356.
[3] M.L. Grossbeck, R.L. Klueh, E.T. Cheng, J.R. Peterson, M.R. Woolery, E.E. Bloom, J. Nucl. Mater. 258-263 (1998) 1778.
[4] D.L. Crandall, D.J. Marts, T.R. Reed, G.R. Smolik, *Space Nuclear Poweer Systems 1987*, Ed. M.S. El-Genk, M.D. Hoover, Orbit Book, Malabar, FL (1988) 457.
[5] K. Natesan, W.K. Soppet, and D.L. Rink, "Uniaxial Creep Behavior of V-4Cr-4Ti Alloy," *Fusion Reactor Materials Semiannual Progress Report for Period Ending June 30, 2000*, DOE/ER/0313/28 (2000) p. 39.
[6] E.R. Gilbert and L.D. Blackburn, Trans ASME, J. Eng. Mater Tech. 99 Series H, No. 2 (1977) 168.
[7] R.J. Kurtz, A.M. Ermi, and H. Matsui, "An Update on Biaxial Thermal Creep of Vanadium Alloys," *Fusion Materials Semiannual Progress Report for Period Ending December 31, 2001*, DOE/ER/)313/31 (2002) p. 7.
[8] M. Schirra, KfK 2440, 2nd ed, Kernforchungszentrum Karlsruhe (1989).
[9] R.E. Gold, D.L. Harrod, R.L. Ammon, R.W. Buckman,Jr., R.C. Svedberg,COO-4540-1, Vol. 2, Westinghouse Electric Corp. (1978).
[10] M. Schirra, in: Kernforchungzentrum Karlsruhe, 2nd Edn., KfK 2440, 1989.
[11] F.R. Larson and J. Miller, Trans. ASME 74 (1952) 765.
[12] D.L. Smith and K. Natesan, Nucl. Tech. 22 (1974) 392.
[13] A.F. Rowcliffe, S.J. Zinkle, and D.T. Hoelzer, J. Nucl. Mater. 283-287 (2000) 508.

2.0 CERAMIC COMPOSITE MATERIALS

EFFECT OF FIBER/MATRIX INTERFACIAL PROPERTIES ON MECHANICAL PROPERTIES OF UNIDIRECTIONAL CRYSTALLINE SILICON CARBIDE COMPOSITES - T. Hinoki, L.L. Snead and E. Lara-Curzio (Oak Ridge National Laboratory), J. Park, Y. Katoh and A. Kohyama (Kyoto University)

OBJECTIVE

The objective of this work is to understand the role of fiber/matrix interfacial strength, including bonding strength and frictional strength, on the properties and behavior of unidirectional silicon carbide matrix composites reinforced with highly crystalline fiber and SiC-based interphase.

SUMMARY

The interfacial properties of CVI-SiC matrix composites reinforced with various fibers (Hi-Nicalon™ Type-S and Tyranno™ SA) and with various fiber/matrix interphase (C, multilayer C/SiC, 'porous' SiC) were evaluated by single fiber push-out testing, compression of double-notched specimens (DNS) and transthickness tensile testing. In turn, these results were correlated with the in-plane tensile stress-strain behavior of the material. The microstructure and fracture surfaces were studied by TEM and SEM. The composites reinforced with Tyranno SA fibers showed brittle fracture behavior, due to large interfacial shear strength and low fiber volume fraction. In the composites reinforced with same fibers, the composites with multilayer C/SiC interphase showed brittle fracture behavior compared with the other composites due to large interfacial shear strength. The transthickness tensile strength of composites reinforced with Hi-Nicalon Type-S fibers was larger than that of composites reinforced with Tyranno SA fibers, although the interlaminar shear strength of both materials determined by DNS was similar.

PROGRESS AND STATUS

Introduction

Silicon carbide has excellent high temperature mechanical properties, chemical stability and low activation properties and therefore SiC/SiC composites are expected to be used as structural material for high temperature industrial and nuclear applications [1,2]. It has been reported that conventional SiC/SiC composites degrade significantly following neutron irradiation due to fiber/matrix interfacial degradation. This degradation has been attributed to shrinkage of the SiC fibers [3] and degradation of the carbon interphase [4]. Therefore, for these materials to be used in nuclear-related applications it will be necessary to develop and evaluate SiC/SiC composites with highly-crystalline SiC fiber and SiC-based fiber/matrix interphases that are expected to be stable to neutron irradiation.

The importance of the fiber/matrix interfacial strength on mechanical properties of CMCs has long been emphasized [5]. The major roles of the interface are the transfer of load between fiber and matrix, and to arrest and deflect crack propagation in the matrix. A balance must be reached, though, to maximize load transfer from the matrix to the fibers and vice versa, while retaining the ability of the fibers to debond and slide. This balance is determined by the magnitude of the interfacial strength at the fiber/matrix interphase. Therefore, to optimize the magnitude of the interfacial strength, the conditions at the interface must be tailored by selecting an appropriate combination of constituents, and perhaps even by modifying the fiber surface topography.

Single fiber push-out test was carried out to evaluate interfacial shear strength including interfacial bonding strength and frictional strength directly. In addition the interlaminar shear strength of these materials was determined by compression of the double-notched specimen (DNS) [7,8]. This simple method was preferred in this work for post-irradiation experiments, since the specimens used in this work would be irradiated by neutrons. Because the state of stress at the fiber/matrix interphase is multiaxial, i.e.- in addition to shear stresses in involves normal tensile stresses, it became necessary to determine the transthickness tensile strength of the material. These properties are controlled by the weakest link among the fiber/matrix interfacial region and the matrix [9].

The objective of this work is to understand the characteristics of the fiber/matrix interfacial strength including bonding strength and frictional strength in unidirectional silicon carbide composites with highly-crystalline fibers and SiC-based interphase. These experimental techniques will be applied to neutron-irradiated experiments. The effects of neutron irradiation on mechanical properties for the composites used in this work will be evaluated in the near future.

Experimental

The materials used in this study were unidirectional SiC fiber-reinforced SiC matrix composites fabricated by isothermal chemical vapor infiltration (ICVI) by Hyper-Therm High-Temperature Composites, Inc. for the ORNL/Kyoto University round robin irradiation program. Fibers used were low-oxygen stoichiometric SiC fibers, Hi-Nicalon™ Type-S [10] and Tyranno™ SA [11,12]. The Tyranno SA fiber used in this work has been identified as “grade 1”. It is a research grade fiber, and its properties are slightly different from Tyranno SA “grade 3” fiber, which currently is commercially available. The tensile strength of grade 1 fibers is 2.0 GPa, while that of grade 3 fibers is larger than 2.5 GPa. Prior to matrix infiltration the fibers were coated with either carbon, multilayer C/SiC or ‘porous’ SiC by CVI. Mixtures of methyltrichlorosilane, argon, methane and hydrogen gases were used to deposit the ‘porous’ SiC interphase onto the fibers. In the multilayer C/SiC interphase, the

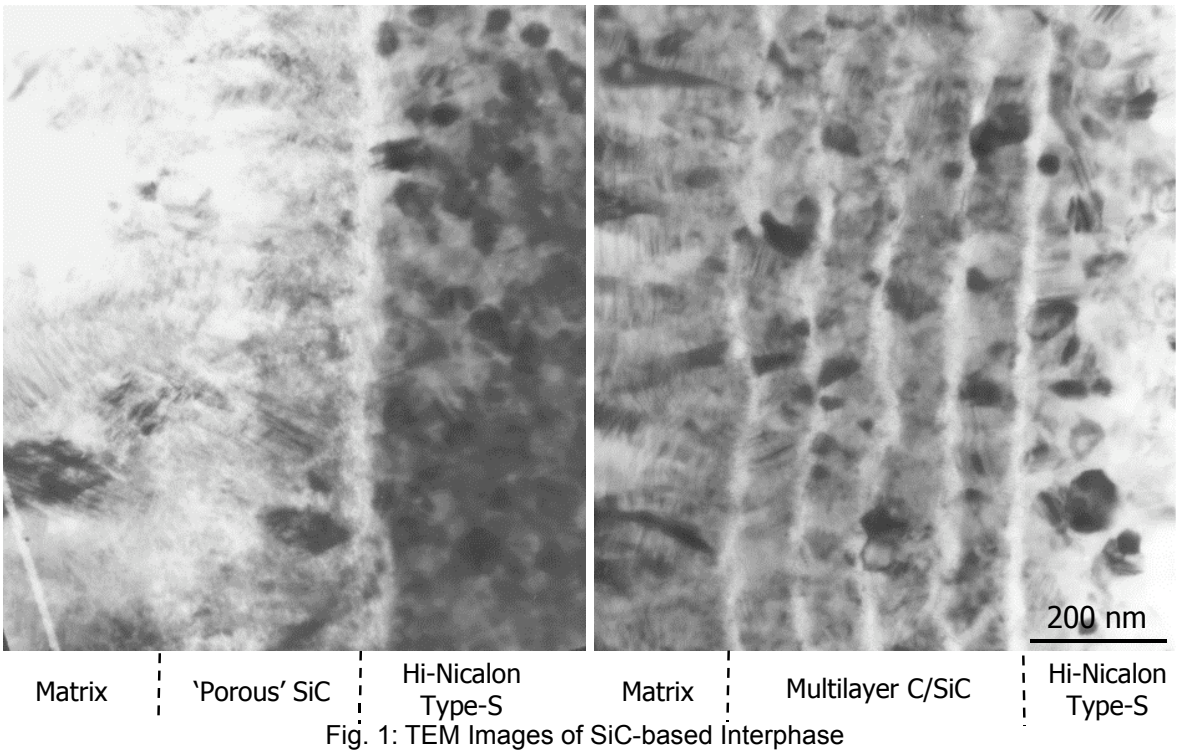

Fig. 1: TEM Images of SiC-based Interphase

first SiC layer was deposited following the deposition of a thin, interrupted layer of pyrolytic C. Four SiC layers were deposited with interrupted pyrolytic C [13]. Transmission electron microscopy (TEM) images of both 'porous' SiC and multilayer C/SiC interphase are shown in Fig. 1. The properties and characteristics of the SiC/SiC composites used in this work are presented in Table I. The thickness of the interphase and fiber volume fraction were estimated from cross sectional SEM images. One of the reasons for the low fiber volume fraction obtained was the extra SiC seal coating applied to the composites, which was 50 μm thick on average.

Table 1: Properties of unidirectional composites

ID	TST1	TST2	TSM	TSP	SAC	SAM
Fiber	Hi-Nicalon™ Type-S				Tyranno™ SA	
F/M interphase	C		Multilayer C/SiC	Porous' SiC	C	Multilayer C/SiC
Interphase Thickness (nm)	520	720	580	380	560	880
Density (Mg/m^3)	2.58	2.58	2.65	2.56	2.55	2.53
V_f (%)	29	29	38	26	21	24
Porosity (%)	19	19	16	19	19	20

Tensile tests were carried out on test specimens with fibers aligned in the loading direction. The test specimens were straight-sided with dimensions 50 mm (long) _ 4 mm (wide) _ 1.5 mm (thick) and the gauge section was 18 mm-long in the middle of the specimen. All tests were conducted at a constant cross-head speed of 10 μm/sec at ambient temperature. Details of the tensile test are reported elsewhere [14].

The double-notched specimens (DNS) for interlaminar shear strength tests were machined to dimensions 25 mm (long) _ 4.0 mm (wide) _ 1.5 mm (thick) and contained two centrally-located notches, 6 mm apart, that were machined halfway through the thickness using a dicing saw, which is an automatic fine slicer with a diamond-impregnated wheel. The shear tests by compression of DNSs were carried out at ambient temperature at a constant cross-head displacement rate of 10 μm/sec. The specimens were end-loaded using a fixture to provide lateral support to prevent specimen buckling. Fracture surfaces following the tensile tests and the shear tests of DNSs were studied by scanning electron microscopy (SEM).

Interfacial shear properties were obtained by single-fiber push-out tests. Samples were sliced from composite specimens normal to the fiber direction into 500 μm-thick sections, which were mechanically polished to a final thickness of approximately 50 μm. In a thicker specimen, the debond crack typically initiates near the top surface when the fiber is pushed in. Eventually when the debond crack propagates in a stable manner through the entire thickness of the specimen the fiber is pushed out. However when a specimen is sufficiently thin (the thickness depends on interfacial shear strength), the push-in load corresponds to push-out load, i.e.- the debond crack propagates through the thickness of the specimen in an unstable manner. The effect of specimen thickness on single fiber push-out test has been reported elsewhere [6]. For the tests the specimens were mounted on top of a holder containing a groove of 50 μm wide. Isolated fibers with the fiber direction perpendicular to the holder surface on the groove were selected with a video microscope

and were pushed out using a Berkovich-type pyramidal diamond indenter tip with maximum load capability of 1 N.

Transthickness tensile tests were also carried out. The samples were machined to dimensions, 5.0 mm (long) _ 5.0 mm (wide) _ 1.5 mm (thick). The test specimens were adhesively-bonded with epoxy to a pair of holders, with 5 mm square faces The holders were connected to the load train using a pair of universal joints to promote self-alignment of the load train during the movement of crosshead to minimize sample bending. All tests were conducted with the cross-head speed of 10 μm/sec at ambient temperature.

Results

The results of tensile testing revealed that both the average ultimate tensile strength (UTS) and proportional limit stress (PLS) of Hi-Nicalon Type-S specimens were larger than those of Tyranno SA specimens. PLS was obtained from using the 0.01 % strain offset criterion. The average modulus of elasticity, obtained from the linear region of the stress-strain curve, of composites reinforced with Tyranno SA fibers was larger than that of composites reinforced with Hi-Nicalon Type-S fibers. Composites reinforced with Hi-Nicalon Type-S showed short fiber pull-out, while composites reinforced with Tyranno SA fibers showed brittle fracture behavior as shown in Fig. 2. It was also found that the tensile properties and fracture behavior of these composites were affected by the fiber/matrix interphase. The magnitude of the UTS, the PLS and modulus of elasticity for composites containing multilayer C/SiC interphase was smaller than that of the other composites. Composites with multilayer C/SiC interphase were brittle compared to composites with the other interphase. The tensile results are presented in Table 2.

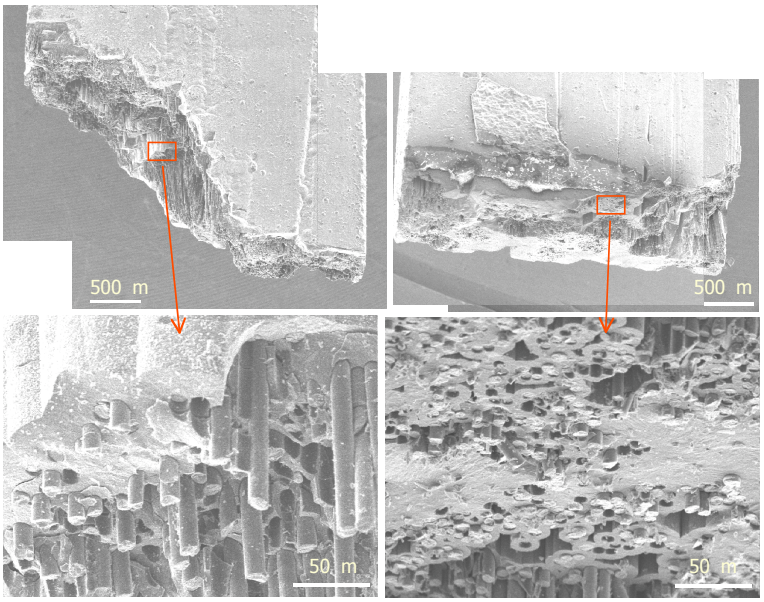

Hi-Nicalon^{TM} type-S/C/SiC^{CVI} Tyranno^{TM} SA/C/SiC^{CVI}

Fig. 3 shows a typical cross head displacement vs. shear stress curve obtained from the compression of a DNS specimen and a crack path in a DNS following a test. The resulting cross

head displacement vs. shear stress curves obtained from the compression of a DNS specimen

Table 2: Summary of mechanical properties

ID	TST1	TST2	TSM	TSP	SAC	SAM
Tensile modulus (GPa)	336	306	256	307	417	350
Flexural modulus (GPa)	296	284	237	260	219	205
Tensile PLS (MPa)	339	268	229	276	220	148
Flexural PLS (MPa)	490	533	356	422	214	199
UTS (MPa)	442	319	229	282	220	148
Flexural strength (MPa)	907	748	757	485	255	199
Shear strength (MPa)	62.8	64.1	60.7	85.8	65.8	56.7
Interfacial shear stress (MPa)	163	149	180	212	211	341
Transthickness tensile strength (MPa)	26.9	-	-	-	20.2	-

were slightly parabolic up to the peak load which was followed by a sudden load drop when the specimens failed. The apparent shear strength (_) was determined from Eq. 1, as the ratio of the peak load, P_{max}, divided by the surface area of the imaginary plane between the notches.

$$\square = \frac{P_{\max}}{wL} \tag{1}$$

where w is the specimen width and L is the notch separation. It was found that there were no significant differences among the shear strength values obtained for the composites evaluated except for the composites reinforced with Hi-Nicalon Type-S fibers and with 'porous' SiC interphase (Fig. 4). The shear strength of composites with multilayer C/SiC interphases was slightly smaller than that of composites with the other interphases.

The interfacial shear strength (ISS) ($_{is}$) of these materials was approximated from the 'push-out' load (P) in single fiber push-out testing and calculated from Eq. 2.

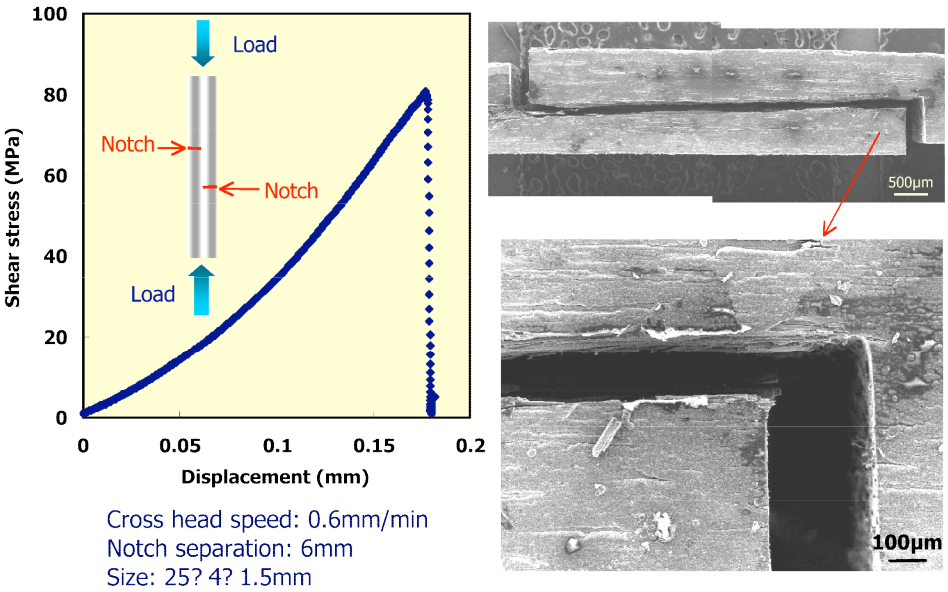

Fig. 3: A Loading Curve and a Crack Path of DNS Shear Test

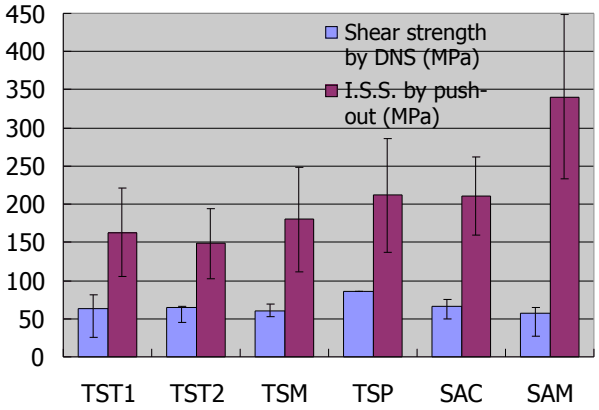

Fig. 4: Effect of fiber and interphase properties on shear strength and interfacial shear strength

$$\tau_{is} = \frac{P}{\pi D t} \tag{2}$$

where τ_{is} D is fiber diameter and t is specimen thickness. Although this is only an approximation, the objective of these tests was establishing a simple procedure for evaluating the effect of neutron irradiation on the interfacial properties of SiC/SiC composites. The results from ISS are compared with those from shear strength testing of DNS in Fig. 4. Error bars of the ISS represent one standard deviation about the mean value whereas the error bars in the DNS shear strength data represent maximum and minimum values. Although the state of stress in these two test configurations are very different, and therefore a direct comparison may not be appropriate, the results obtained from these tests will provide the means for identifying changes in the interfacial properties of these materials that may be induced by neutron irradiation. For composites with the same interphase, the ISS of composites reinforced with Tyranno SA fibers was slightly larger than that of composites reinforced with Hi-Nicalon Type-S fibers. In composites reinforced with same fiber, the ISS of composites with multilayer C/SiC interphase and 'porous' SiC interphase was slightly larger than that of composites with C interphase.

A typical fracture surface and crack path for a transthickness tensile test specimen are shown in Fig. 5. It was found that in this test the crack propagated interlaminarly between large pores in the

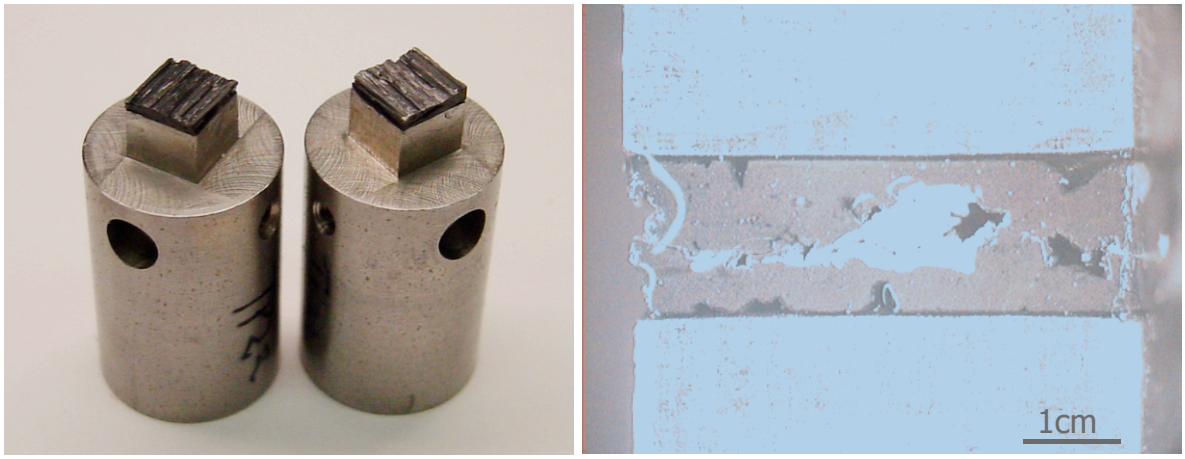

Fig. 5: Fracture surface and crack path of transthickness tensile specimen

matrix. The cross head displacement vs. stress curves obtained from transthickness tensile testing were slightly parabolic up to the peak load which was followed by a sudden load drop when the specimens failed as shown in Fig. 6. Average transthickness tensile strength of SAC (Tyranno SA/C/SiC) and TST1 (Hi-Nicalon Type-S/C/SiC) composites was 20.2 MPa and 26.9 MPa, respectively. Mechanical properties are summarized in Table 2.

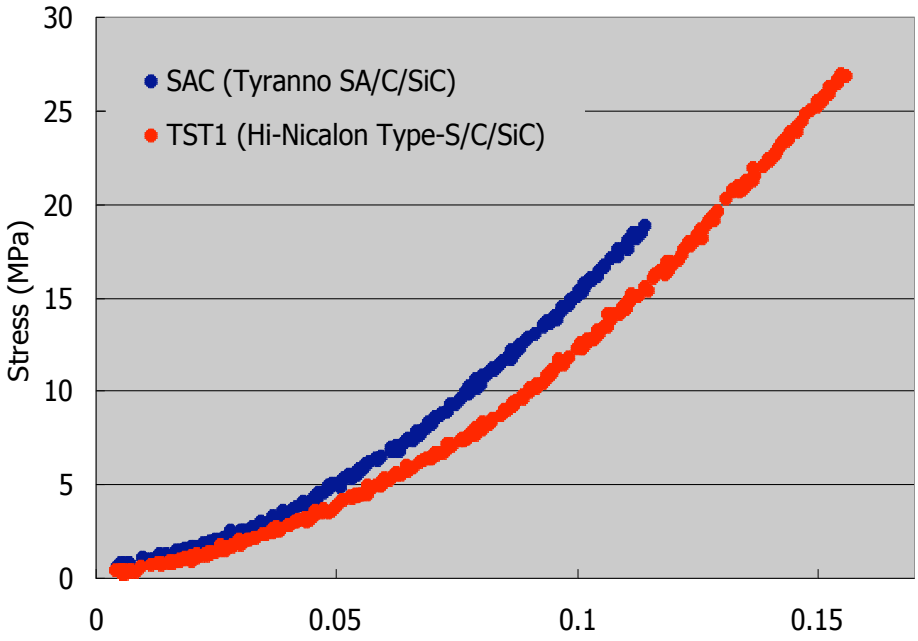

Fig. 6: Effect of fiber on displacement vs. stress curves of transthickness tensile tests

Discussions

The ISS of composites reinforced with Tyranno SA fibers obtained from single fiber push-out tests was larger than that of composites reinforced with Hi-Nicalon Type-S fibers and similar interphase. These differences can be explained from the differences in the surface topography of these fibers as a result of the differences in grain sizes. The surface roughness of these fibers was evaluated quantitatively by Micromap system. Fig. 7 shows the surface height of the single fibers, respectively. 'Rq' in the figure means the Root-Mean-Square (RMS) surface height. The average RMS surface height of Hi-Nicalon Type-S and Tyranno SA was 0.87 and 1.72 nm, respectively. These results are consistent with the difference in tensile behavior that was observed between composites reinforced with these two fibers, particularly the differences in the magnitude of fiber pull-out observed during fractographic examination which is related to the magnitude of the interfacial shear stress according to:

$$h = \frac{\sigma_m^{\ 2} r}{2\tau} \qquad (3)$$

where h is pullout length, σ_m is matrix cracking stress, r is fiber radius and τ is interfacial shear strength. The matrix cracking stress and the fiber diameter of composites reinforced with Tyranno SA fibers are smaller and the interfacial shear strength of the composites is larger than that of the composites reinforced with Hi-Nicalon Type-S fibers. So pull-out length of composites reinforced

with Tyranno SA fibers should be shorter than that of the composites reinforced with Hi-Nicalon Type-S fibers.

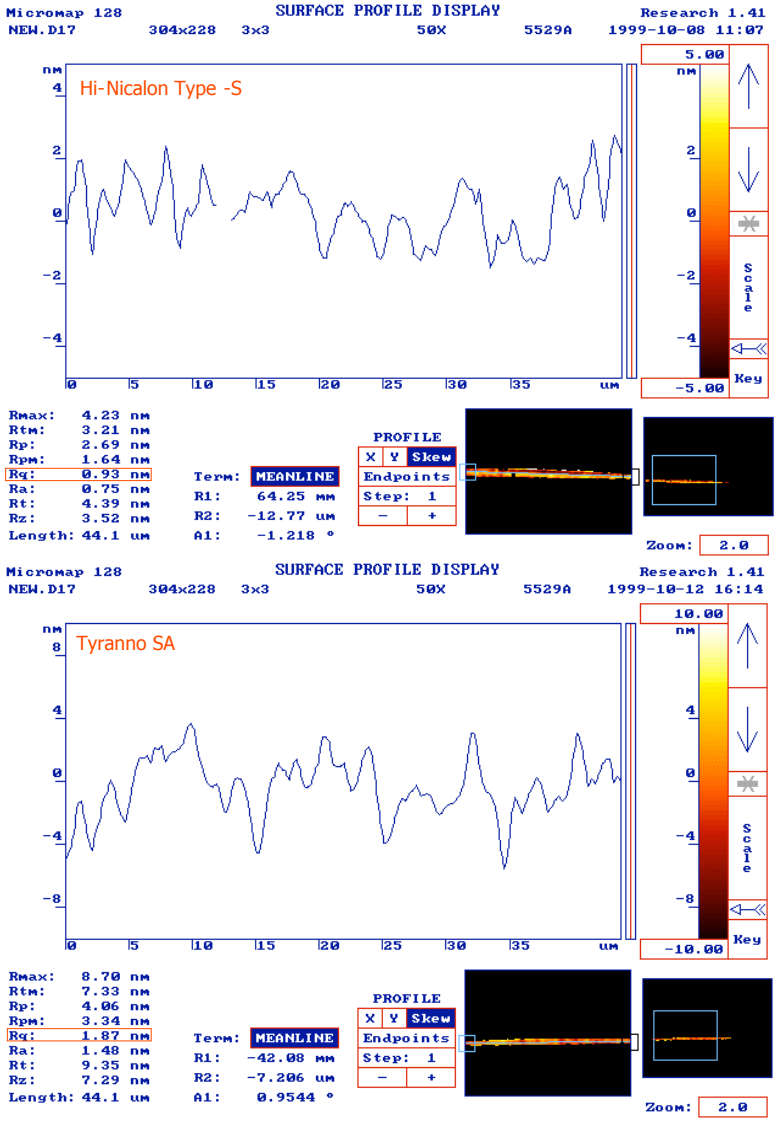

Fig. 7: Surface roughness of the fibers, Hi-Nicalon Type-S and Tyranno SA (grade 1)

The theoretical modulus of composites (E_c) is calculated from Eq. 4.

$$E_c = V_f E_f + V_m E_m \tag{4}$$

where E_f and E_m are moduli of fiber and matrix, V_f and V_m are volume fractions of fiber and matrix. From this calculation, the moduli of the composites used in this study must be comparable and in the case of composites reinforced with Hi-Nicalon Type-S and Tyranno SA fibers containing C interphase should be 363 GPa. However the modulus of the composites reinforced with Tyranno SA fibers is larger than that of the composites reinforced with Hi-Nicalon Type-S. The modulus of composites reinforced with Tyranno SA fibers is larger than the modulus obtained from Eq. 4 and

therefore, it is likely that the actual modulus of Tyranno SA fiber is larger than the value reported by the manufacturer.

In composites reinforced with the same fiber, the magnitude of the ISS for composites containing multilayer C/SiC interphase and 'porous' SiC interphase was larger than that of composites containing C interphase. In the particular case of composites reinforced with Tyranno SA and multilayer C/SiC interphases, the magnitude of the ISS was much larger than of composites containing C interphases. In composites with multilayer C/SiC interphase, the fiber surface roughness is reflected in the rough features of the fracture surface with large interfacial frictional strength, since the first C layer is very thin. The results of ISS do not correlate with the results of DNS shear strength. Shear strength by DNS is affected by porosity, fiber volume fraction and pore size. To understand the different trends between ISS and DNS shear strength, further investigations are required.

There was no significant effect of fiber type on the magnitude of the interlaminar shear strength determined by the compression of double-notched specimens. However, the transthickness tensile strength of composites reinforced with Hi-Nicalon Type-S fibers was much larger than that of composites reinforced with Tyranno SA fibers. DNS shear strength is affected by the roughness of fracture surface, while transthickness tensile strength does not affected significantly. Porosity of composites reinforced with Hi-Nicalon Type-S fibers was lower than that of composites reinforced with Tyranno SA fibers. The average pore size of composites reinforced with Tyranno SA fibers seemed larger than that of composites reinforced with Hi-Nicalon Type-S fibers. These results induce that the large interfacial strength of composites reinforced with Tyranno SA fibers is attributed to larger interfacial frictional strength.

CONCLUSIONS

(1) The interfacial frictional stresses were larger in composites reinforced with Tyranno SA fibers that in composites reinforced with Hi-Nicalon Type-S fibers, and this difference was explained based on the difference in surface topography between these fibers. As a result, composites reinforced with Tyranno SA fibers showed brittle fracture behavior compared with composites reinforced with Hi-Nicalon Type-S fibers. It was also found that the interfacial bonding in composites reinforced with Hi-Nicalon Type-S was larger than that of composites reinforced with Tyranno SA fibers.

(2) Composite materials containing multilayer C/SiC interphases exhibited less and shorter fiber pull-out and brittler behavior than composites containing other interphases, since the average interfacial shear strength in composites with multilayer C/SiC interphases is larger than that of composites containing C interphases. It was found that the magnitude of the difference of interfacial shear strength was the largest for composites reinforced with Tyranno SA fibers.

ACKNOWLEDGEMENT

This work was supported by Japan-USA Program of Irradiation Test for Fusion Research (JUPITER) and by Core Research for Evolutional Science and Technology (CREST) program under the title of "R & D of Environment Conscious Multi-Functional Structural Materials for Advanced Energy Systems".

REFERENCES

[1] P. Fenici, A.J. Frias Rebelo, R.H. Jones, A. Kohyama and L.L. Snead, J. Nucl. Mater., 258-263 (1998) 215.

[2] L.L. Snead, R.H. Jones, A. Kohyama and P. Fenici, J. Nucl. Mater., 233-237 (1996) 26-36.

[3] G.W. Hollenberg, C.H. Henager, Jr., G.E. Youngblood, D.J. Trimble, S.A. Simonson, G.A. Newsome and E. Lewis, J. Nucl. Mater., 219 (1995) 70-86.

[4] J.H.W. Simmons, Radiation Damage in Graphite, Pergamon Press, (1965).

[5] E. Lara-Curzio and M. K. Ferber, Numerical Analysis and Modeling of Composite Materials, Ed. J. W. Bull, Blackie Academic & Professional (1995) 357-399.

[6] T. Hinoki, W. Zhang, A. Kohyama, S. Sato and T. Noda, J. Nucl. Mater., 258-263 (1998) 1567-1571.

[7] E. Lara-Curzio and M.K. Ferber, Thermal and Mechanical Test Methods and Behavior of Continuous-Fiber Ceramic Composites, ASTM STP 1309, Edited by M.G. Jenkins, S.T. Gonczy, E. Lara-Curzio, N.E. Ashbaugh and L.P. Zawada, American Society for Testing and Materials, (1997) 31-48.

[8] E. Lara-Curzio and M. Singh, J. Mater. Sci. Lett., 19 (2000) 657-661.

[9] E. Lara-Curzio, Comprehensive Composites Encyclopedia, Elsevier, (2000) 533-577.

[10] M. Takeda, A. Urano, J. Sakamoto and Y. Imai, J. Nucl. Mater., 258-263 (1998) 1594-1599.

[11] T. Ishikawa, Y. Kohtoku, K. Kumagawa, T. Yamamura and T. Nagasawa, Nature, 391 (1998) 773-775.

[12] T. Ishikawa, S. Kajii, T. Hisayuki, K. Matsunaga, T. Hogami and Y. Kohtoku, Key Eng. Mater., 164-165 (1999) 15-18.

[13] L.L. Snead, M.C. Osborne, R.A. Lowden, J. Strizak, R.J. Shinavski, K.L. More, W.S. Eatherly, J. Bailey and A.M. Williams, J. Nucl. Mater., 253 (1998) 23-30.

[14] T. Hinoki, L.L. Snead, E. Lara-Curzio, Y. Katoh and A. Kohyama, Fusion Materials Semi-Annual Progress Reports, DOE/ER-0313/29 (2000) 74-84.

3.0 FERRITIC/MARTENSITIC STEELS

FRACTURE SURFACE OF A REDUCED-ACTIVATION MARTENSITIC STEEL IRRADIATED IN HFIR - N. Hashimoto (Oak Ridge National Laboratory), H. Tanigawa (Japan Atomic Energy Research Institute), K. Shiba (JAERI), and R.L. Klueh (ORNL)

OBJECTIVE

The objective of this effort is to provide information of postirradiation deformation mechanisms controlling in ferritic/martensitic steels

SUMMARY

A reduced activation ferritic/martensitic steel, F82H (IEA heat), developed for fusion energy applications was irradiated at 300 and 500°C to 5 dpa in the High Flux Isotope Reactor (HFIR). In order to investigate test temperature and strain-rate effects on deformation mode, fracture surfaces were examined by scanning electron microscopy (SEM). Changes in yield strength, deformation mode, and strain-hardening capacity were seen, with the magnitude of the changes dependent on irradiation temperature. Irradiation at 300°C led to a significant loss of strain-hardening capacity with a large change in yield strength. Irradiation at 500°C had little effect on strength. The fracture surface of the specimens irradiated at 500°C and 300°C in tests at –100°C with a strain rate of $1x10^{-4}$ s^{-1} showed a martensitic mixed quasi-cleavage and ductile-dimple fracture in the center. On the other hand, in the specimen irradiated at 300°C, tensile test at –100 °C with a strain rate of $1x10^{-1}$ s^{-1} resulted in brittle (cleavage) fracture.

PROGRESS AND STATUS

Introduction

For structural applications in fusion energy systems, the ferritic/martensitic steels have several advantages based upon their resistance to void swelling, good thermal stress resistance, and well-established commercial production and fabrication technologies. Ferritic/martensitic steels, however, undergo radiation-induced hardening during neutron irradiation at temperatures up to 400°C, with a transition to fluence-dependent radiation softening at temperatures above 400-450°C. Radiation hardening is often accompanied by a reduction in strain-hardening capacity and uniform elongation, an increase in the temperature delineating the transition from quasi-cleavage to ductile fracture, and increased propensity for brittle failure under certain combinations of temperature and loading conditions. In order to investigate test temperature and strain rate effects on deformation mode, scanning electron microscopy (SEM) was performed on tested (fractured) tensile specimens of irradiated reduced activation F82H (IEA heat).

Experimental Procedures

The material studied was F82H (IEA heat), austenitized at 1040°C for 38 minutes, air cooled, and tempered at 750°C for 60 minutes. The chemical composition of the F82H (IEA heat) is shown in Table 1. SS-3 sheet tensile specimens with gage section of 7.62 mm x 0.76 mm x 1.5 mm were irradiated in the HFIR RB-11J and -12J capsules with europium thermal neutron shields for neutron spectrum tailoring. Irradiation conditions for these capsules are summarized in Table 2, and further information on the experiment can be found elsewhere [2-5]. Using an Instron universal testing machine for the tensile testing, the specimens irradiated at 300 and 500°C were tested at –100 °C with strain rates of $1x10^{-1}$ s^{-1} and $1x10^{-4}$ s^{-1}. The 0.2% offset yield strength (YS), ultimate tensile strength (UTS), uniform elongation (E_U), and total elongation (E_t) were

calculated from the engineering load-elongation curves. Following deformation, the specimens were examined using SEM to investigate the fracture surfaces.

Table 1. Chemical composition of F82H-IEA (wt.%) (Balance Fe).

	Cr	W	V	Ta	Mn	Al	C	B	Si	P	S	N
82H (IEA heat)	7.71	1.95	0.16	0.02	0.16	0.003	0.090	0.0002	0.11	0.002	0.002	0.006

Table 2. Summary of irradiation conditions.

Capsule	Nominal Irradiation Temperature (°C)	Neutron fluence (n/cm^2) Thermal (E<0.5eV)	Neutron fluence (n/cm^2) Fast (E>0.1MeV)	Dose (dpa)	He (appm)
11J Shielded	307±19	1x10^{21}	1x10^{22}	4.5~4.8	3
12J Shielded	497±22	1x10^{21}	1x10^{22}	4.7~4.8	3

Results and discussion

Tensile Behavior

Stress-strain curves of F82H (IEA heat) irradiated at 300 and 500°C in tests at –100°C at two strain rates are shown in figure 1. The tensile test data are summarized in Table 3. The irradiation at 300°C led to significant hardening and loss of strain-hardening capacity. The specimen irradiated 300°C in test with a strain rate of 1x10^{-1} s^{-1} showed brittle failure, while, the test with a strain rate of 1x10^{-4} s^{-1} resulted in ductile fracture. In contrast, the specimens irradiated at 500°C did not show irradiation hardening or degradation in ductility.

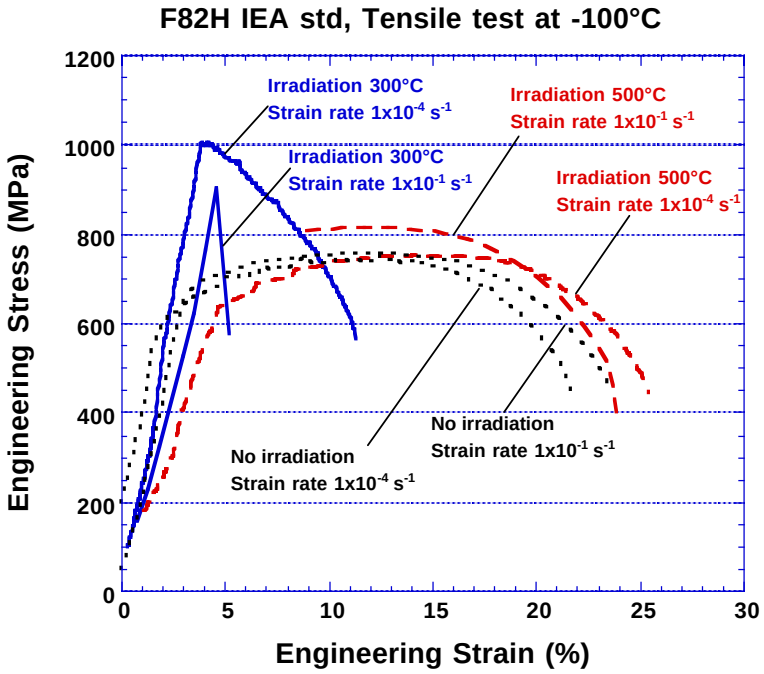

Fig. 1. Stress-strain curves of F82H-IEA irradiated at 300 and 500°C and tested at –100°C.

Table 3 Summary of tensile test at –100°C

ID	Dose (dpa)	Irr. Temp. (°C)	Test Temp. (°C)	Strain Rate (s^{-1})	YS (MPa)	UTS (MPa)	E_u (%)	E_t (%)	Remark
A048	-	-	-100	$1x10^{-4}$	571	742	10	20.1	
A050	-	-	-100	$1x10^{-1}$	664	758	7.0	20.5	
A008	4.5	307±19	-100	$1x10^{-4}$	1002	1002	0.2	7.2	
A012	4.8	307±19	-100	$1x10^{-1}$	903	903	0	0	Brittle
A029	4.7	497±22	-100	$1x10^{-4}$	651	752	8.9	20	
A031	4.8	497±22	-100	$1x10^{-1}$	-	814	-	-	Ductile

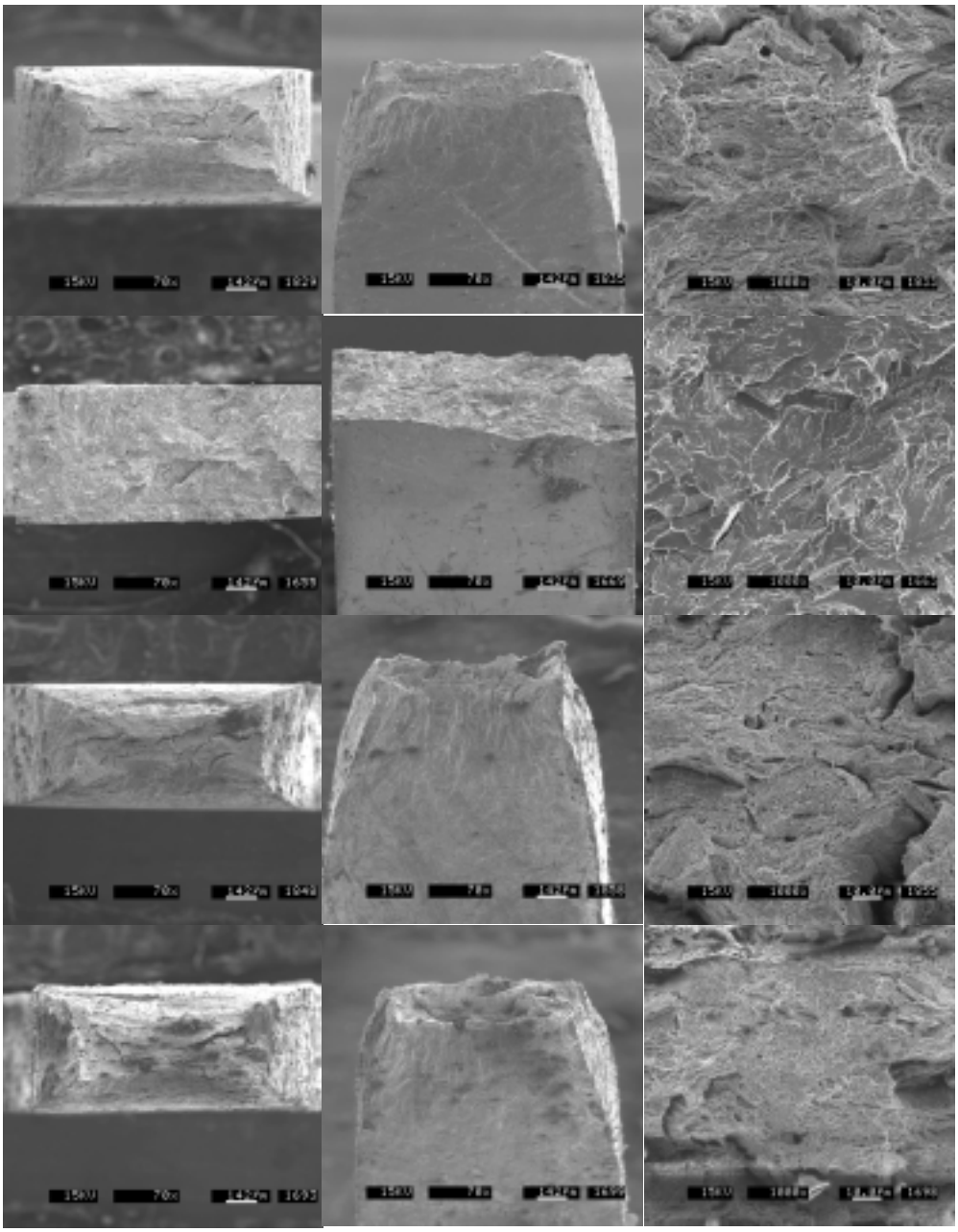

Figure 3. Fracture surfaces of irradiated specimens tensile-tested at -100°C with strain rates of $1x10^{-4}$ and $1x10^{-1}$ s^{-1}.

Fracture Surface Features

Fracture surfaces of the specimens irradiated at 300 and 500°C in tests at -100°C with strain rates of $1x10^{-4}$ and $1x10^{-1}$ s^{-1} are shown in figure 3. At lower magnification, it can be shown that strain of A008, A029 and A031 is very localized following irradiation. The grain size is on the order of 100 μm, and each grain contains slip steps appearing as wavy lines. At higher magnification, fracture surfaces of A008, A029 and A031 showed a typical martensitic mixed quasi-cleavage and ductile-dimple fracture in the center. The sizes of large and small dimples were about 4-5μm and 0.5μm, respectively. As shown in figure 1, the specimen irradiated at 300°C showed a loss of strain-hardening capacity with a large change in yield strength compared with 500°C. However, the fracture surface of the specimens irradiated at 300°C showed similar fracture features as specimens irradiated at 500°C. Hashimoto *et al.* reported similar tensile behavior and fracture surfaces in the irradiated F82H-IEA tested at 25°C [5], TEM observation for the specimens suggested that irradiation-induced dislocation loops are responsible for the irradiation hardening, and dislocation channeling appears to be the dominant deformation mechanism. For a specimen irradiated at 500°C, there was little effect of irradiation on the tensile behavior and little change in microstructure, indicating a change in the deformation process with temperature.

Shiba *et al.* reported that the strain-rate effect on tensile behavior in F82H-IEA [6] tested at 25°C at $1x10^{-4}$ and $1x10^{-2}$ s^{-1} showed an increase in yield stress and a decrease in elongation with increasing strain rate. The specimens irradiated at 500°C did not exhibit any change in strength, although the slowest strain rate produced less total elongation. In the present experiment, the change of strain rate did not affect yield stress and elongation, but fracture mode was effected. As seen in figure 3, the fracture surface of the A012, irradiated at 300°C in tests at –100°C with a strain rate of $1x10^{-1}$ s^{-1}, showed transgranular cleavage fracture with some splitting (figure 2), meaning faster strain rate led to brittle fracture.

ACKOWLEDGEMENT

The authors would like to thank Dr. T.S. Byun and Messrs. J.L. Bailey, A.M. Williams and J.J. Duff for technical support. This research was sponsored by the Office of Fusion Energy Sciences, US Department of Energy under contract DE-AC05-96OR22464 with UT-Battelle, and the Japan Atomic Energy Research Institute.

REFERENCES

1. J.E. Pawel, K.E. Lenox, and I. Ioka, *Fusion materials semiannual progress report*, DOE/ER-0313/**19**, 312 (1995).
2. J.E. Pawel, K.E. Lenox, I. Ioka, and E. Wakai, *Fusion materials semiannual progress report*, DOE/ER-0313/**21**, 249 (1996).
3. M.L. Grossbeck, K.E. Lenox, M.A. Janney, T. Muroga, W.W. Heatherly, and K.R. Thoms, *Fusion materials semiannual progress report*, DOE/ER-0313/**22**, 254 (1997).
4. K.E. Lenox and M.L. Grossbeck, *Fusion materials semiannual progress report*, DOE/ER-0313/**25**, 307 (1998).
5. N. Hashimoto, S.J. Zinkle, R.L. Klueh. AF. Rowcliffe, and K. Shiba, Microstructural Process in Irradiated Materials–2000, Mat. Res. Soc. Symp. Proc. Vol. **650** (2000) R1.10.
6. K. Shiba, R.L. Klueh, Y. Miwa, N. Igawa, and J.P. Robertson*, Fusion materials semiannual progress report*, DOE/ER-0313/**28**, 131 (2000).

EFFECT OF HEAT TREATMENT AND TANTALUM ON MICROSTRUCTURE AND MECHANICAL PROPERTIES OF Fe-9Cr-2W-0.25V STEEL—R. L. Klueh, N. Hashimoto, and M. A. Sokolov (Oak Ridge National Laboratory)

OBJECTIVE

The objective of this work is to develop an understanding of the effect of microstructure on the ferritic/martensitic steels that are of interest for fusion applications and to use that knowledge to develop steels with improved properties.

SUMMARY

A reduced-activation steel with a nominal composition of Fe-9Cr-2W-0.25V-0.07Ta-0.1C (9Cr-2WVTa) was developed for fusion reactor applications. The steel has excellent Charpy impact properties and shows superior resistance to irradiation embrittlement. The impact properties of a similar steel composition but without the Ta (9Cr-2WV) are inferior to those of 9Cr-2WVTa when the steels are given the same normalizing-and-tempering heat treatment (austenitized at 1050ºC and tempered at 750ºC). Tantalum refines the grain size, and to determine the effect of grain size on the Charpy impact properties of the 9Cr-2WV and 9Cr-2WVTa steels, specimens of the two steels were given different normalization heat treatments to produce different prior austenite grain sizes, and the tensile and impact properties were determined. Under the conditions that the microstructures were generated by these different heat treatments, the 9Cr-2WV steel had impact properties similar to or better than those of the 9Cr-2WVTa steel. Differences in the microstructures of the steels were used to explain the observations and what they mean for developing steels with improved properties for fusion applications.

PROGRESS AND STATUS

Introduction

A reduced-activation steel with a nominal composition (in wt. %) of Fe-9.0Cr-2.0W-0.25V-0.07Ta-0.1C (9Cr-2WVTa) developed for fusion applications had excellent mechanical properties [1] and superior resistance to irradiation embrittlement, as demonstrated by a relatively small increase in the ductile-brittle transition temperature ΔDBTT) when irradiated up to 28 dpa at 250-400ºC [2-9]. The shift in DBTT was only 32ºC (Fig. 1). The impact properties of a similar composition but without the tantalum (9Cr-2WV) showed a shift of almost twice as much (61ºC) when the steels were given the same normalizing-and-tempering heat treatment (austenitized at 1050ºC and tempered at 750ºC) (Fig. 1) [2-5,9].

The 9Cr-2WVTa steel had a smaller prior-austenite grain size after the 1050ºC austenitization treatment, but otherwise the microstructures were similar before irradiation and showed similar changes during irradiation. In addition to the difference in embrittlement behavior, the irradiation behavior of the 9Cr-2WVTa steel differed from the 9Cr-2WV steel and most similar 8-12% Cr steels in two ways. First, the shift in DBTT of the 9Cr-2WVTa steel did not saturate with fluence by 28 dpa, whereas for the 9Cr-2WV steel and most similar steels, saturation occurs at <10 dpa. This is shown in Fig. 1, and although the increase for 9Cr-2WVTa was gradual and small, it did appear to continue to increase. The second difference was that the shift in DBTT for the irradiated 9Cr-2WVTa steel increased with increasing irradiation temperature (Fig. 1), whereas it decreased for the 9Cr-2WV steel, as it does for most similar steels [4-6]. In this case, because the DBTT of the 9Cr-2WV steel before irradiation was considerably higher than that of the 9Cr-2WVTa, after irradiation it was still higher than that of the 9Cr-2WVTa. However, they developed similar increases in DBTT during irradiation [8].

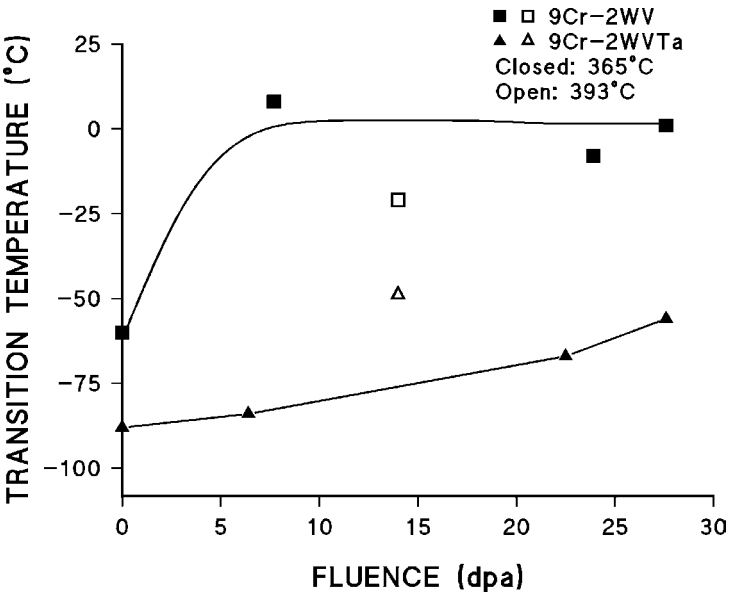

Figure 1. Transition temperature of as a function of fluence.

The improved properties of the 9Cr-2WVTa steel and the differences from other steels during irradiation were attributed to tantalum in solution [5,8,9-11]. Tantalum was determined to be in solution from transmission electron microscopy (TEM) studies that analyzed the amount of tantalum in precipitates [10] and by atom probe analyses [11]. Tantalum in solution caused a grain refinement and affected the impact properties partly due to the smaller prior austenite grain size and partly due to an effect on the fracture stress of the steel [5,8,9]. It was hypothesized that the different behavior of 9Cr-2WV and 9Cr-2WVTa during irradiation was caused by a loss of tantalum from solution by precipitation [5,8]. Since the loss of tantalum will be diffusion controlled, it should proceed throughout the irradiation, leading to a continued increase in the DBTT, as observed, if tantalum has an effect other than just the effect on grain size. Likewise, an increase in the irradiation temperature should increase the rate of precipitation, as equilibrium will be achieved at a higher rate. A precipitation of tantalum was confirmed by Kimura et al. for a 9Cr-2WVTa steel irradiated in FFTF at 460ºC, when they found that tantalum-rich M_6C precipitated [11]. They did not observe any tantalum-rich precipitates when irradiated at the lower temperature of 390ºC for the fluence used, which is in agreement with the observations on the unusual temperature effect discussed above.

From these observations, it was postulated that if the effect of tantalum in solution was lost by precipitation, then once equilibrium for the tantalum is reached, the difference in the behavior of the 9Cr-2WV and 9Cr-2WVTa steels would be caused by the difference in prior-austenite grain size and any tantalum remaining in solution, which could be quite small. This appears to be the case, since there is little difference in the ΔDBTT of the steels after irradiation at the higher temperature (Fig. 1). Therefore, it might be possible to get similar irradiation resistance without the tantalum [5,6] if the prior-austenite grain size of the 9Cr-2WV could be reduced. In this paper, different heat treatments were used to vary the prior-austenite grain size of 9Cr-2WV and 9Cr-2WVTa steels. The effect of the heat treatments on the microstructure and the tensile and Charpy properties were determined.

Experimental Procedure

The 9Cr-2WV and 9Cr-2WVTa steels are nominally Fe-9Cr-2W-0.25V-0.1C without and with 0.07% Ta, respectively. They were prepared as 18 kg electro-slag remelted heats by Combustion Engineering, Inc, Chattanooga, Tennessee. Compositions for the two steels were given previously [1].

Specimens were taken from a 6.35-mm plate after pieces of the plate were given several normalizing-and-tempering heat treatments. Normalization involved an austenitization treatment followed by cooling in flowing helium gas. Specimens were austenitized as follows: 0.033, 0.25, and 0.5 h (5, 15, and 30 min) at 950ºC, 0.5 h at 1000ºC, and 0.5 h at 1050ºC. All specimens were tempered 1 h at 750ºC.

Tensile specimens 25.4-mm long with a reduced gage section 7.62-mm long by 1.52-mm wide by 0.76-mm thick were machined from the 6.35-mm plate. Tensile tests were at room temperature on a 120-kN Instron universal test machine at a nominal strain rate of 1×10^{-3} s^{-1}. Two tests were conducted for each test condition.

Charpy specimens were one-third size V-notch specimens measuring 3.3 x 3.3 x 25.4 mm with a 0.51-mm-deep 30º V-notch and a 0.05- to 0.08-mm-root radius that were machined from normalized-and-tempered 6.35-mm plates. Specimens were machined from normalized-and-tempered plate along the rolling direction with the notch transverse to the rolling direction (L-T orientation). The DBTT was determined at an energy level midway between the upper and lower shelf energies. Details on the test procedure for the subsize impact specimens have been published [13-15].

Results

Mechanical Properties

The tensile and Charpy data are given in Table 1 for the five normalizing conditions: 950ºC/5min, 950ºC/15min, 950ºC/30min, 1000ºC/15min, 1050ºC/30min; all were tempered 1 h at 750ºC.

Table 1. Tensile and Charpy Data

Steel	Austenitization Conditions	Yield Stress[a]	Ultimate Strength	Uniform Elongation	Total Elongation	Charpy DBTT[b]	Charpy USE
9Cr-2WV	950C/5m	560	698	8.1	18.8	-109	11.8
9Cr-2WV	950C/15m	548	716	8.2	19.1	-105	11.9
9Cr-2WV	950C/30m	551	698	8.2	18.5	-85	12.6
9Cr-2WV	1000C/15m	548	691	7.8	18.8	-95	11.8
9Cr-2WV	1050C/1h	549	659	4.7	12.3	-60	8.4
9Cr-2WVTa	950C/5m	549	691	7.9	17.4	-99	11.6
9Cr-2WVTa	950C/15m	559	691	8.1	18.4	-99	11.0
9Cr-2WVTa	950C/30m	563	693	7.9	18.7	-94	12.1
9Cr-2WVTa	1000C/15m	572	700	7.2	17.6	-89	11.4
9Cr-2WVTa	1050C/1h	544	652	4.3	12.3	-88	11.2

[a] The tensile data represent the average of two tests.
[b] The DBTT was calculated as one-half the difference between the upper shelf and lower shelf.

Figure 2(a) shows the room-temperature yield stress for the five normalizing conditions. Despite the differences in normalizing conditions, there was little difference among the specimens of the 9Cr-2WV and 9Cr-2WVTa and little difference between the two different steels. A similar observation was made on the ultimate tensile strength (Table 1). The total elongations [Fig. 2(b)] also showed no change when the austenitizing temperature was 950 or 1000ºC, but for 1050ºC, there was about a 30% decrease in elongation. A similar effect was observed for the uniform elongation (Table 1).

The effect of the different heat treatments on the DBTT values [Fig. 3(a)] measured for the 9Cr-2WVTa steel with 1/3-size Charpy specimens was rather small for all of the heat treatments. For the 9Cr-2WV,

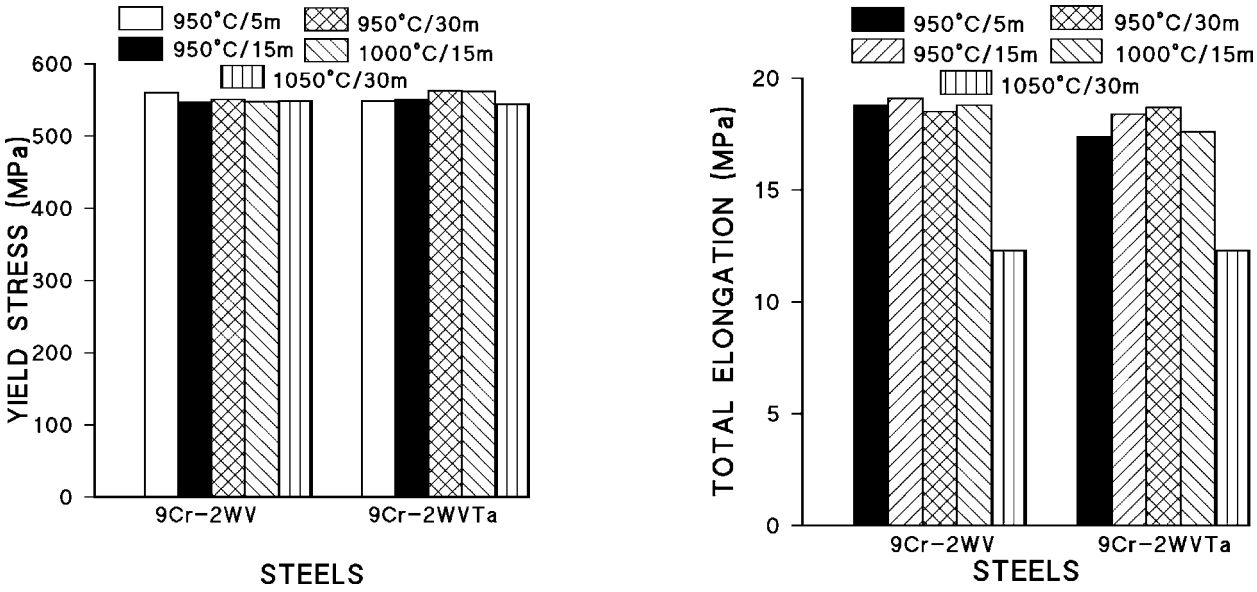

Figure 2. Room temperature yield stress (left) and total elongation (right) of 9Cr-2WV and 9Cr-2WVTa steels given different heat treatments.

on the other hand, there was more change, especially for the 1050ºC austenitization treatment. The upper-shelf energy (USE) [Fig. 3(b) showed essentially no change with austenitization temperature for the 9Cr-2WVTa. Likewise, there was no change for the 9Cr-2WV for the 950 and 1000ºC austenitization treatments. However, just as was the case for the total elongation, there was a relatively large change (decrease) when austenitized at 1050ºC.

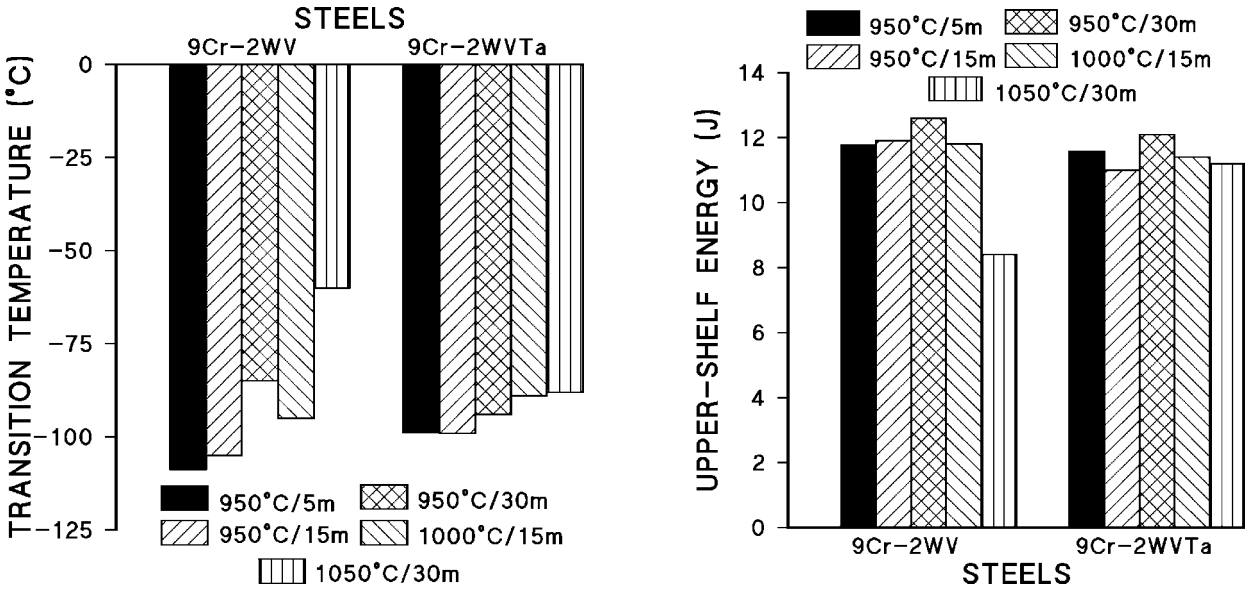

Figure 3. Charpy transition temperature (left) and upper-shelf energy (right) of 9Cr-2WV and 9Cr-2WVTa steels given different heat treatments.

Microstructure

The effect of tantalum on the prior-austenite grain size for the 9Cr-2WV and 9Cr-2WVTa steels is obvious in the 100% tempered martensite microstructures of the two steels in Fig. 4 for the austenitization at 1050ºC for 0.5 h. Grain sizes were estimated by optical microscopy after the different anneals (Fig. 5). There was a large increase in the grain size of the 9Cr-2WV steel with an increase in time at 950ºC and with an increase in temperature from 950 to 1000 to 1050ºC. Less change occurred for the 9Cr-2WVTa than the 9Cr-2WV for all of the heat treatment conditions. The largest difference in grain size for the two steels occurred for those austenitized at 1050ºC. The results indicate that tantalum is very effective in reducing austenite grain growth.

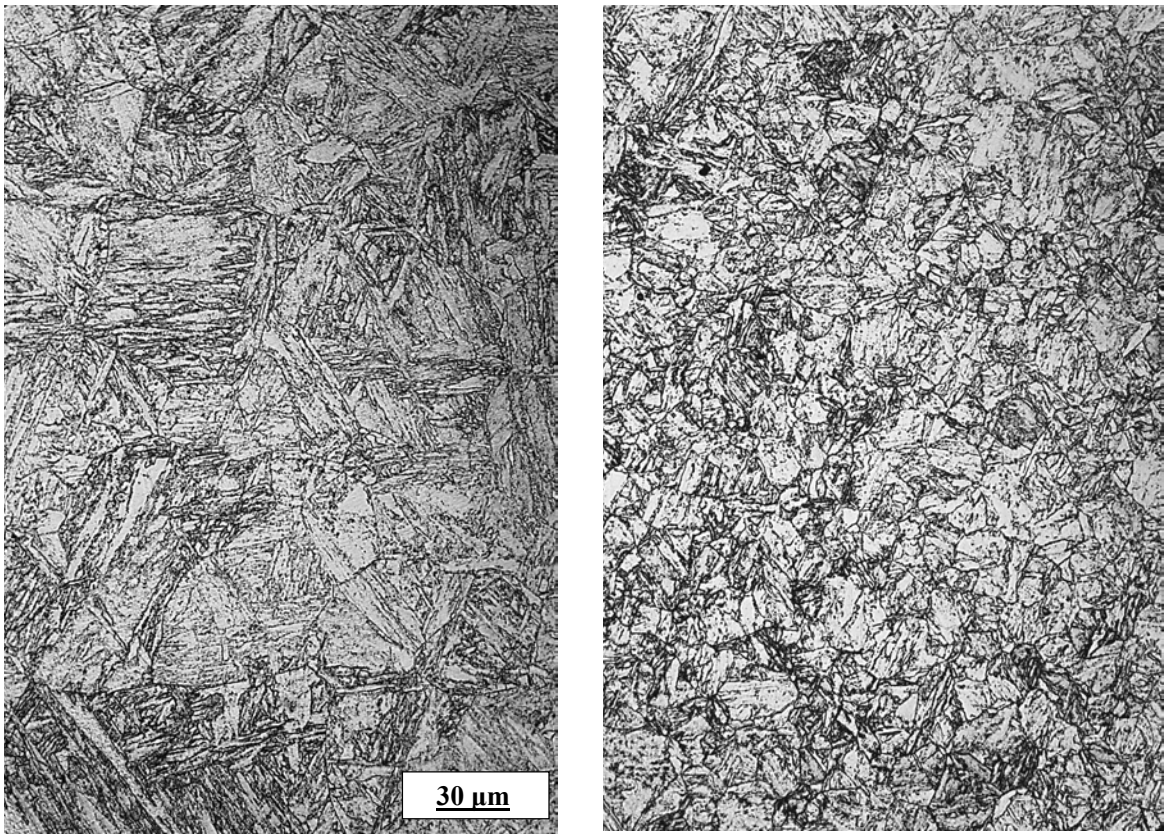

Figure 4. Photomicrographs of 9Cr-2WV (left) and 9Cr-2WVTa (right) steels austenitized for 0.5 h at 1050ºC.

Grain-size measurements were made at low magnification (100X), and it appeared that the microstructures for all of the different heat treatments were 100% martensite for both steels. Examination of the 9Cr-2WV by transmission electron microscopy (TEM) verified that this steel was 100% martensite for all heat treatment conditions; a typical tempered martensite structure was observed, as shown in Fig. 6(a) for the steel austenitized 5 min at 950ºC. With the exception of the prior-austenite grain size, there was little difference in the structure of the 9Cr-2WV steel heat treated for different times at 950ºC and at the other two temperatures [Figs. 6(b), 6(c), and 6(d)]. The lath sizes also did not vary substantially for the different heat treatments. The average lath width was estimated at 0.3-0.6 µm.

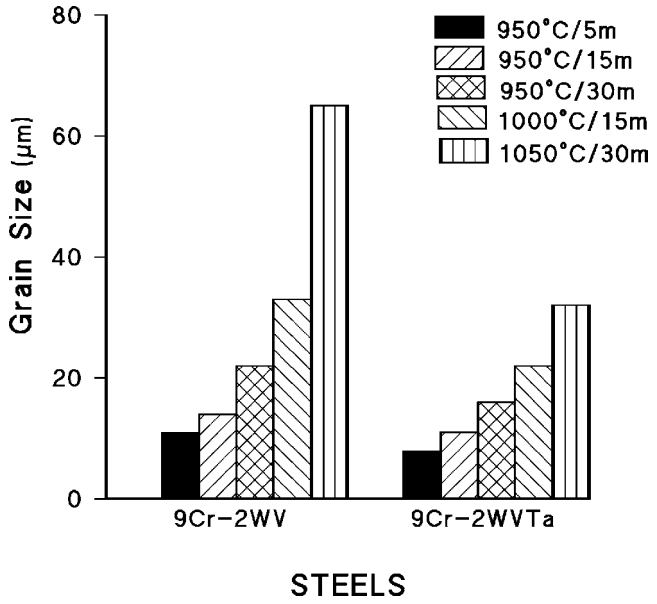

Figure 5. Prior-austenite grain size of 9Cr-2WV and 9Cr-2WVTa steels given different heat treatments.

The 9Cr-2WVTa steel, on the other hand, had a somewhat different microstructure after it was austenitized at 950ºC for 5 min: it contained regions of ferrite [Fig. 6(a)] that evidently had not transformed to austenite during the exposure at 950ºC. The amount of ferrite was estimated at around 10-15%. A smaller amount of ferrite (3-6%) was found in the specimen heat treated at 950ºC for 15 min [Fig. 6(b)]. A small amount (<1%) of ferrite was also observed in the steel austenitized 30 min at 950ºC, but none was present after the 1000 and 1050ºC heat treatment. Neither was there any after the 1050ºC heat treatment.

Since the presence of ferrite had not been detected by optical microscopy when the specimens were examined for prior-austenite grain size at low magnification, the steels were re-examined and the ferrite identified. At high magnification (500X), ferrite could be easily observed (Fig. 7). None was detected for the steel austenitized for 15 min at 1000ºC by either optical microscopy or TEM (none was observed by TEM after the 30 min anneal at 950ºC, although a small amount was observed by optical microscopy.

The lath structure of the martensite in the 9Cr-2WVTa steel was similar to that of the 9Cr-2WV steel with a similar lath size (Fig. 8).

Although no attempt was made to identify the precipitates in this work, the precipitate morphology and distribution are typical of those in most 9-12Cr steels (Fig. 9). Precipitates have been studied and identified in the 9Cr-2WV and 9Cr-2WVTa steels previously [13,14], and the majority of the precipitates are $M_{23}C_6$ (estimated at 100-200 nm diameter at a number density of 10^{19}-10^{20} m^{-3} in both steels). These are the large precipitates on the prior-austenite grain boundaries and lath boundaries in Fig. 12. The other precipitate that has been identified is small MX particles in the matrix. These are present at a lower number density (estimated at 20-50 nm diameter and 10^{17}-10^{18} m^{-3}) than the $M_{23}C_6$ [13,14].

Discussion

The results indicate that tantalum plays a complicated role in the mechanical properties and microstructural behavior of the 9Cr-2WVTa steel. Despite the difference in prior-austenite grain sizes of the 9Cr-2WV and 9Cr-2WVTa steels and the change in the grain size with different heat treatments, the room temperature yield stress and ultimate tensile strength were essentially unaffected, indicating that the

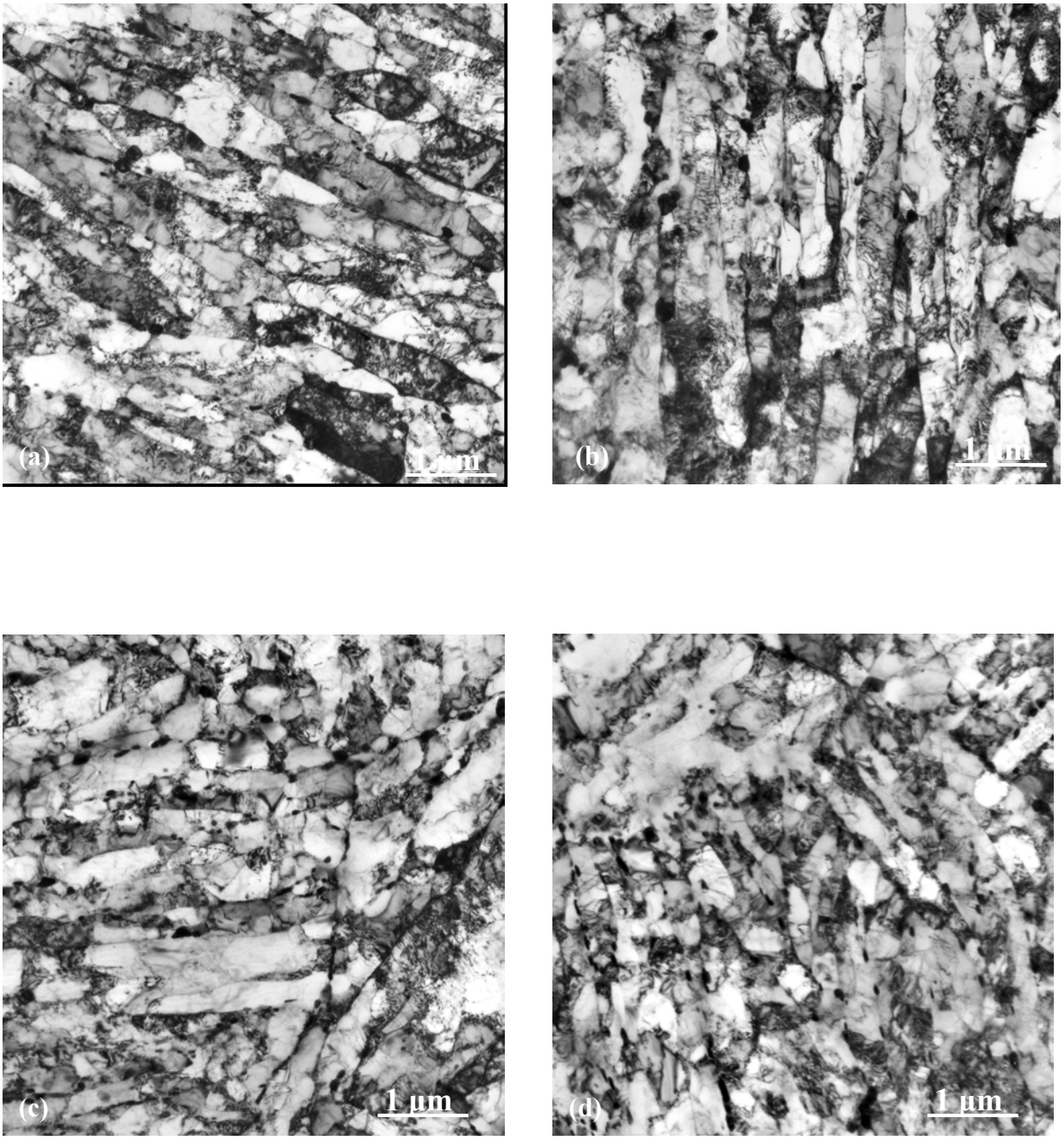

Figure 6. TEM micrographs of the 9Cr-2WV steel austenitized at (a) 5 min at 950ºC (b) 15 min at 950ºC, (c) 30 min at 950ºC, and (d) 15 min at 1000ºC.

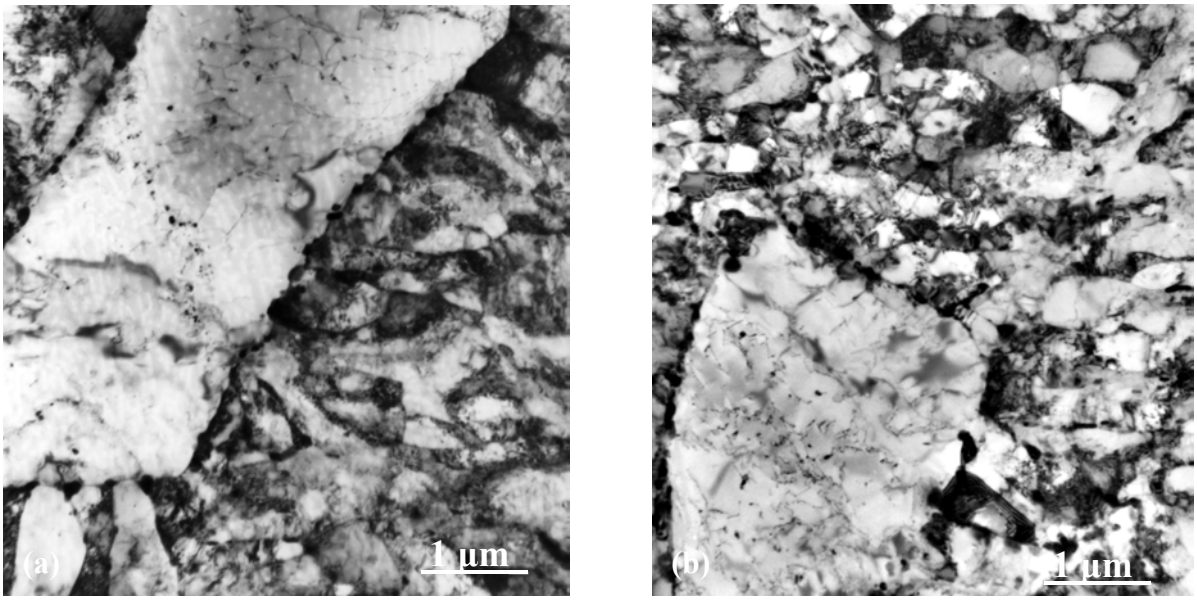

Figure 7. TEM micrographs of 9Cr-2WVTa steel austenitized (a) 5 min and (b) 15 min at 950ºC.

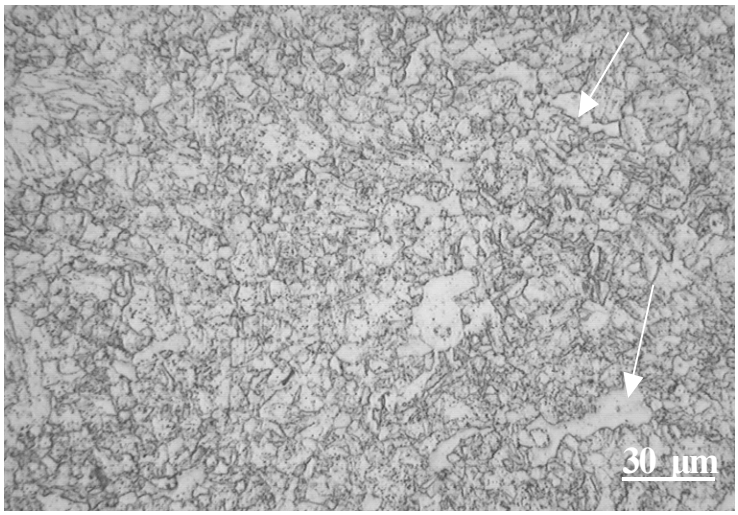

Figure 8. Photomicrograph of 9Cr-2WVTa steel austenitized 5 min at 950ºC; arrows indicate ferrite.

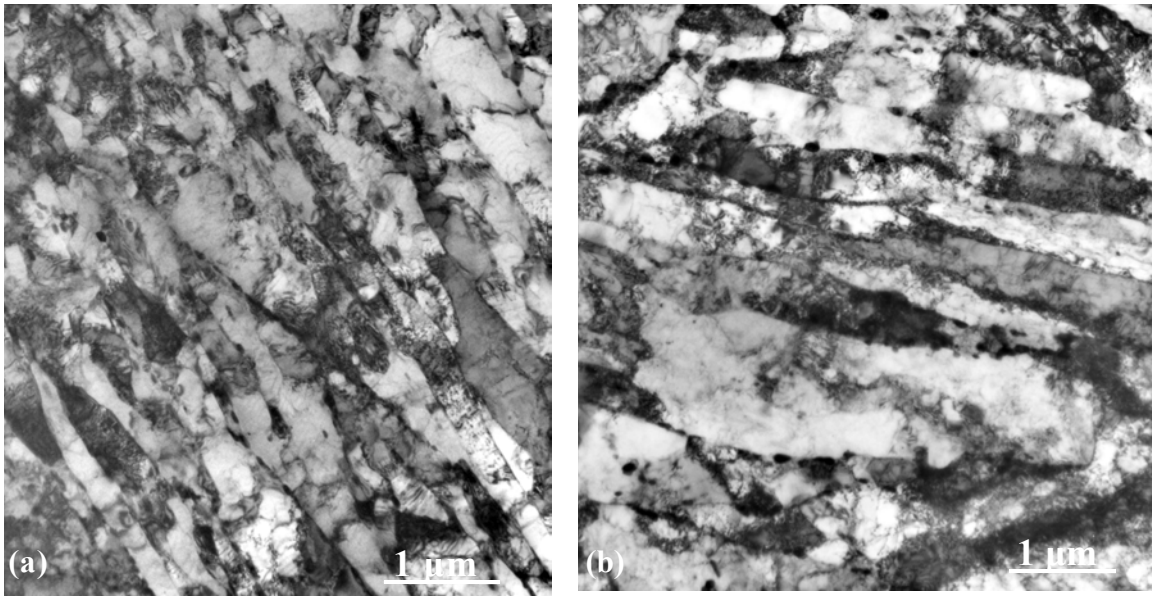

Figure 9. TEM photomicrographs of (a) 9Cr-2WV and (b) 9Cr-2WVTa showing similar lath sizes.

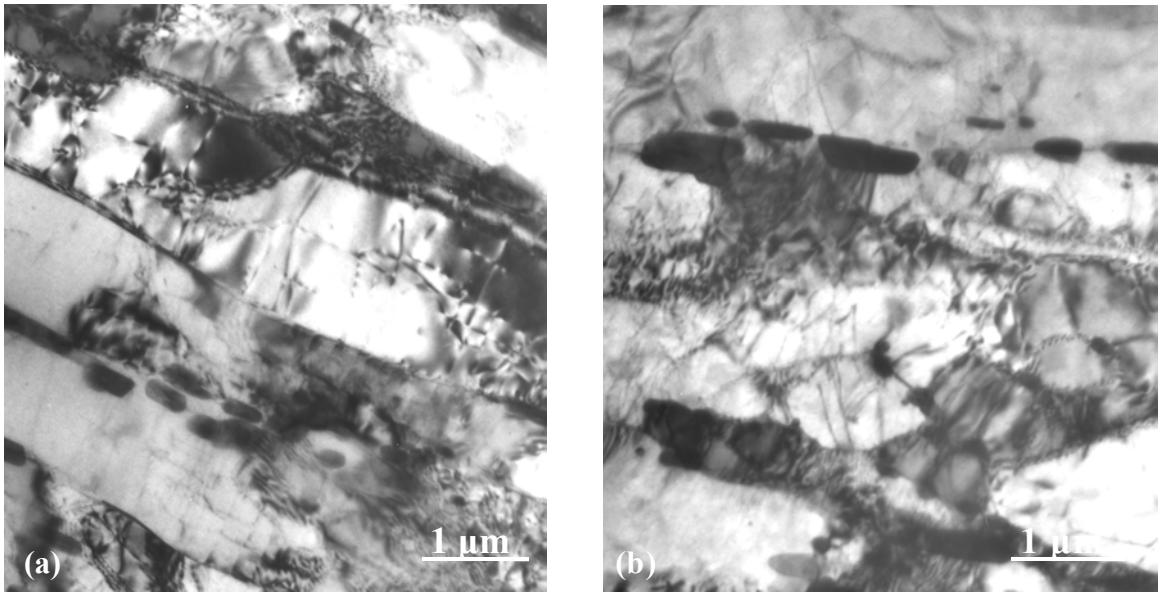

Figure 10. TEM photomicrographs of (a) 9Cr-2WV and (b) 9Cr-2WVTa showing typical precipitate microstructures of the steels (austenitized at 1050ºC).

strength is determined primarily by the martensite microstructure and is unaffected by the prior austenite grain size. The ductility was only affected at the highest austenitization temperature (1050ºC), and again, there was little difference between the 9Cr-2WV and 9Cr-2WVTa. Thus, it is difficult to see how this could be affected by prior-austenite grain size, since there was quite a large difference in grain size of the two steels after the 1050ºC heat treatment (Fig. 5) but essentially no difference in uniform or total elongation.

This similarity in strength and ductility has previously been observed in both the unirradiated and irradiated conditions [5,8].

The DBTT change of the 9Cr-2WV steel for the different heat treatments appears reflective of a prior-austenite grain size effect, since there did not appear to be any other obvious microstructural changes to account for the change of the DBTT. Precipitation appeared to be similar for the different heat treatments. This might be expected, since most of the precipitates form during the tempering treatment. The USE appeared much less affected than the DBTT; it changed (decreased) only after the 1050ºC anneal, similar to the change in ductility.

Charpy properties of the 9Cr-2WVTa steel showed relatively little change: there was a slight increase with an increase in time and temperature of the austenitization treatment. This change probably reflects the much smaller change in prior-austenite grain size, and it may also reflect the previous observations that there is a component of the fracture resistance of this steel that can be attributed to tantalum in solution [5,8].

Despite the smaller grain size of the tantalum-containing steel after the 950ºC heat treatment for 5 and 15 min, the 9Cr-2WV steel had a lower DBTT than the 9Cr-2WVTa steel for these heat treatments. This is probably caused by the ferrite in these two samples. The presence of δ-ferrite has been shown to affect the transition temperature of other 9 and 12% Cr steels [16,17], and the ferrite in the present steels could act in the same way.

The interesting observation that after the two short-time (5 and 15 min) heat treatments at 950ºC the 9Cr-2WVTa contained ferrite and the 9Cr-2WV did not is another indication of the effect of tantalum. It is assumed that the transformation of ferrite to austenite on heating proceeds by nucleation and growth, which means this is another observation that tantalum retards the growth of austenite (it could also retard nucleation), the same conclusion reached by the observations on grain size differences between 9Cr-2WV and 9Cr-2WVTa.

In light of the observation that tantalum is lost from solution during irradiation, the objective for this work was to determine if the steel without tantalum could be made to perform as well as the steel with tantalum. Since irradiation has an effect on fracture properties by increasing the transition temperature, this comparison was to be made on the Charpy properties. If the comparison is made between the low-temperature anneals (950 and 1000ºC) of the 9Cr-2WV and the 1050ºC anneal used for the 9Cr-2WVTa previously, then it is possible to improve the Charpy properties of the 9Cr-2WV to be as good or better than those of the 9Cr-2WVTa. That is, a 1000ºC austenitization temperature with a DBTT of ≈-90ºC (Table 1) could be used to get a comparable DBTT to that of the 9Cr-2WVTa annealed at 1050ºC. Assuming that because of the finer prior-austenite grain size, the ΔDBTT for similar irradiations at 365ºC to those of Fig. 1 should be less than observed previously and may approach that of the 9Cr-2WVTa. Likewise, at 393ºC, where the ΔDBTT of the 9Cr-2WV and 9Cr-2WVTa steels was similar (Fig. 1), the steels would be expected to have similar DBTTs after irradiation to a fluence similar to that used previously [8]. Therefore, by decreasing the prior-austenite grain size of the 9Cr-2WV steel, it is expected that the Charpy properties of the steel could be as made as good or better than the 9Cr-2WVTa steel.

Although the grain size of the 9Cr-2WV—and the 9Cr-2WVTa—could be reduced by using a lower austenitizing temperature or another thermomechanical processing technique, it is not clear that it would be advisable. No effect of the small grain size on creep properties has been determined. The fine grain size could reduce the creep strength. Therefore, it appears that the use of tantalum to reduce the grain size and contribute in other ways to the fracture resistance may be the best way to achieve the properties required. However, if it were necessary to remove tantalum—say for nuclear considerations [18]—then it should still be possible to produce a comparable steel without tantalum.

Summary and Conclusions

The effect of prior-austenite grain size and tantalum on a nominal Fe-9Cr-2W-0.25V-0.10C (9Cr-2WV) steel was determined by examining the effect of austenitization time and temperature on the room-temperature tensile properties and Charpy properties of the 9Cr-2WV steel and this steel with 0.07% Ta (9Cr-2WVTa). To vary the prior-austenite grain size of the normalized steel, specimens were austenitized for 5, 15, and 30 min at 950ºC, 15 min at 1000ºC, and 30 min at 1050ºC, followed by a rapid cool in flowing helium gas. All specimens were tempered 1 h at 750ºC.

The results can be summarized as follows:

- Tantalum causes grain refinement in the 9Cr-2WVTa, but it does not cause other significant differences in microstructure (martensite lath size and precipitates) with 9Cr-2WV.
- Neither the prior-austenite grain size nor tantalum affected the strength.
- Ductility was unaffected except after the 1050ºC heat treatment, where total and uniform elongation decreased; similar decreases occurred for the 9Cr-2WV and 9Cr-2WVTa steels.
- The DBTT of the 9Cr-2WV steel showed significant increases with increasing prior- austenite grain size, whereas, the 9Cr-2WVTa was much less sensitive to prior-austenite grain size.
- The USE of the 9Cr-2WVTa was unaffected by the different heat treatments, and the USE of the 9Cr-2WV was unaffected except after the 1050ºC austenitization, where it was reduced significantly.

It should be possible to produce a 9Cr-2WV steel with tensile and impact properties as good as those of the 9Cr-2WVTa by reducing the prior-austenite grain size. The effect of such a small grain size on the creep properties has not been determined.

References

[1] R. L. Klueh, "Heat Treatment Behavior and Tensile Behavior of Cr-W Steels," *Met. Trans.* Vol. 20A, 1989, pp. 463-470.
[2] R. L. Klueh, D. J. Alexander, and P. J Maziasz, "Impact Behavior of Reduced-Activation Ferritic Steels Irradiated in the Fast Flux Test Facility," *J. Nucl. Mater.,* Vo. 186, 1992, pp.185-195.
[3] R. L. Klueh and D. J. Alexander, "Impact Toughness of Irradiated Reduced-Activation Ferritic Steels," *J. Nucl. Mater.*, Vo. 212-215, 1994, pp. 736-740.
[4] R. L. Klueh and D. J. Alexander, "Impact Behavior of Reduced-Activation Steels Irradiated to 24 dpa," *J. Nucl. Mater.*, Vol. 233-237, 1996, pp. 336-341.
[5] R. L. Klueh and D. J. Alexander, “Tensile and Charpy Impact Properties of Irradiated Reduced-Activation Ferritic Steels,” *Effects of Radiation on Materials: 18th International Symposium*, *ASTM STP 1325*, R. K. Nanstad, M. L. Hamilton, F. A. Garner, and A. S. Kumar, Eds., American Society for Testing and Materials, Philadelphia, 1999, pp. 911-930.
[6] M. Rieth, B. Dafferner, and H. D. Röhrig, “Charpy Impact Properties of Low Activation Alloys for Fusion Applications after Neutron Irradiation,” *J. Nucl. Mater.*, 233-237, 1996, pp. 351-355.
[7] M. Rieth, B. Dafferner, and H. D. Röhrig, “Embrittlement Behavior of Different International Low Activation Alloys after Neutron Irradiation,” *J. Nucl. Mater.*, 258-263, 1998, pp. 1147-1152.
[8] R. L. Klueh and D. J. Alexander, “Effect of Heat Treatment and Irradiation Temperature on Impact Properties of Cr-W-V Ferritic Steels,” *J. Nucl. Mater.*, Vol. 265, 1999, pp. 262-272.
[9] R. L. Klueh, D. J. Alexander, and M. Rieth, “The Effect of Tantalum on the Mechanical Properties of a 9Cr-2W-0.25V-0.07Ta-0.01C Steel,” *J. Nucl. Mater.*, Vol. 273 (1999, pp. 146-154.
[10] J. J. Kai and R. L. Klueh, “Microstructural Analysis of Neutron-Irradiated Martensitic Steels,” *J. Nucl. Mater.*, Vol. 230, 1996, pp. 116-123.
[11] R. Jayaram and R. L. Klueh, “Microstructural Characterization of 5-9% Cr-2%W-V-Ta Martensitic Steels,” *Metall. and Matls Trans.*, Vol. 29A, 1998, pp. 1551-1558.
[12] A. Kimura, M. Narui, T. Misawa, H. Matsui, and A. Kohyama, Dependence of Impact Properties on Irradiation Temperature in Reduced-Activation Martensitic Steels,” J. Nucl. Mater., Vol. 258-263, 1998, pp. 1340-1344.

[13] D. J. Alexander, R. K. Nanstad, W. R. Corwin, and J. T. Hutton, “A Semi-Automated Computer-Interactive Dynamic Impact Testing System,” *Automation Technology to Fatigue and Fracture Testing*, *ASTM STP 1092*, A. A. Braun, N. E. Ashbaugh, and F. M. Smith, Eds., American Society for Testing and Materials, Philadelphia, 1990, pp. 83-94.
[14] D. J. Alexander and R. L. Klueh, “Specimen Size Effects in Charpy Impact Testing,” *Charpy Impact Test: Factors and Variables*, *ASTM STP 1072*, J. M. Molt, Ed., American Society for Testing and Materials, Philadelphia, 1990, pp. 179-191.
[15] M. A. Sokolov and R. K. Nanstad, “On Impact Testing of Subsize Charpy V-Notch Type Specimens,” *Effects of Radiation on Materials: 17th International Symposium*, *ASTM STP 1270*, D. S. Gelles, R. K. Nanstad, A. S. Kumar, and E. A. Little, Eds., American Society for Testing and Materials, Philadelphia, 1996, pp. 384-414.
[16] K. Anderko, L. Shäfer, and E. Materna-Morris, Effect of the δ-Ferrite Phase on the Impact Properties of Martensitic Chromium Steels,” J. Nucl. Mater., Vol. 179-181, 1991, pp. 492-495.
[17] L. Shäfer, J. Nucl. Mater., “Influence of Delta Ferrite and Dendritic Carbides on the Impact and Tensile Properties of a Martensitic Chromium Steel,” Vol. 258-263, 1998, pp. 1336-1339.
[18] E. T. Cheng, “Concentration Limits of Natural Elements in Low Activation Fusion Materials,” *J. Nucl. Mater*. Vol. 258-263, 1998, pp. 1767-1772.

4.0 COPPER ALLOYS

5.0 REFRACTORY METALS AND ALLOYS

No contributions.

6.0 AUSTENITIC STAINLESS STEELS

No contributions.

FINAL RESULTS ON AN EXPERIMENT TO DETERMINE THE LOWER TEMPERATURE LIMIT OF VOID SWELLING OF STAINLESS STEELS AT RELATIVELY LOW DISPLACEMENT RATES –

S. I. Porollo, Y. V. Konobeev, A. M. Dvoriashin, and V. M. Krigan (Institute of Physics and Power Engineering, Obninsk, Russia) and F. A. Garner (Pacific Northwest National Laboratory)*

OBJECTIVE

The objective of this effort is to determine the lower temperature limit of void swelling when reactor components are exposed to relatively low displacement rates.

SUMMARY

Recent studies associated with light water reactors (LWR) in both the USA and Russia have raised the question of void swelling in austenitic components of core internals. One question of particular interest is the range of temperatures over which voids can develop, especially the lowest temperature. This question is equally relevant to fusion reactors, especially those operating with water cooling and therefore exposed to temperatures below those attainable in various high-flux fast reactors used to generate most of the relevant high fluence data.

To address this question a flow restrictor component manufactured from annealed X10H18T was removed from the reflector region of the BN-350 fast reactor. During operation this component spanned temperatures and dpa rates of direct interest not only to pressurized water reactors (PWRs) in the West and VVERs in Russia, but also to various proposed fusion devices. This steel is analogous to AISI 321 and is used in Russian reactors for applications where AISI 304 would be used in the West. This component was sectioned on a very fine scale to determine in what range of conditions voids existed. Microstructural data were obtained for 157 separate locations, with 111 specimens showing voids over the relevant range of temperatures and displacement rates, allowing construction of a parametric map of swelling with temperature, dpa and dpa rate. These data show that void swelling at 10 to 50 dpa persists down to ~306°C for dose rates in the range 0.1 x 10^{-7} to 1.6 x 10^{-7} dpa/sec.

Introduction

Voids as a new type of radiation defect were discovered in fuel pin cladding made from austenitic stainless steels irradiated in the DFR fast reactor (Cawthorne and Fulton, 1967). For a long time it was perceived that the phenomenon of void formation is characteristic only for fast reactor irradiation with its high displacement rates and elevated irradiation temperatures. Recently data have became available providing evidence that void formation may occur in structural materials of PWR and VVER internals, in which neutron damage doses of 50 dpa and higher can be accumulated during operating lifetimes. In addition to dimensional changes, swelling in structural materials of PWR and VVER internals (in particular, austenitic stainless steels such as AISI 304 and X18H10T) will lead to appearance of mechanical stresses caused by the non-uniformity of swelling and can also lead to irradiation embrittlement if the swelling level exceeds some critical value.

As a rule, the temperature dependence of swelling in austenitic steels such as X18H10T and other metals and alloys often exhibits a bell-shaped form with a maximum, height and location of which are determined by the initial microstructural condition of a material, but especially by irradiation conditions. Specifically, the most important parameters are the inlet and outlet temperatures of the reactor component and the neutron flux profile across the reactor, which for small reactors is often bell-shaped. The actual low temperature limit of void formation in a material should be related to low vacancy mobility and/or to the ability of vacancies to aggregate and form voids, a condition that may exist below the inlet temperature of a given reactor. Likewise, the upper temperature limit of void formation is usually related to a low super-saturation of vacancies at high temperatures, often well above the maximum temperature of the material in any given reactor.

Data on swelling of steels such as X18H10T in fast reactors are reasonably available. However, most

* Pacific Northwest National Laboratory (PNNL) is operated for the U.S. Department of Energy by Battelle Memorial Institute under contract DE-AC06-76RLO-1830.

of these data have been obtained for neutron irradiation temperatures above 350-370°C, and only scarce data on swelling are available for temperatures in the range 280 - 350°C. The same can be said concerning data for the austenitic steel 304, which is a steel of type X18H9 in the Russian notation. The reason is simply that most Western and some Russian fast reactors have relatively high inlet sodium temperatures, on the order of 365°C or higher.

Experimental data on swelling in austenitic stainless steels irradiated at temperatures below 350°C at dose rates relevant to PWRs and VVERs are of significant interest, since the inlet temperatures of these reactors is usually below 300°C. Potential sources of such data are core components and internal devices of pressurized water reactors, but it is often very difficult to remove components from such devices at high enough neutron exposure. Such devices usually operate at much lower flux levels than used in fast reactors.

Another approach is to examine components of fast reactor cores irradiated to high doses with inlet temperatures significantly lower than 350°C. This approach introduces a significant influence of neutron flux when the components are extracted from the core region. A third and better approach is to examine a very long-lived component from the low-flux reflector region of a fast reactor with a low inlet temperature, which is the path used in this study.

In this report the results are presented of a microstructural study to determine the swelling of type 12X18H9T austenitic stainless steel after irradiation in the BN-350 fast reactor at temperatures ranging from 280°C to 334°C and doses from 9 to 56 dpa. Extensive sectioning of the component followed by electron microscopy was the approach employed.

This effort is now complete after four years duration. Several earlier reports presented fractions of these data as it was collected (1,2).

Material and irradiation conditions

To study the swelling and mechanical properties of type 12X18H9T steel after low-temperature neutron irradiation, one of the BN-350 components was chosen. This component served as a coolant flow restrictor in the line connecting the reactor vessel to a sodium tank. The component is a hexagonal tube of 96 mm flat-to flat size, having a central cylindrical hole of 65 mm in diameter. The total length of the flow restrictor component equals the length of reference driver subassemblies of the BN-350 fast reactor (3.435 m). This flow restrictor component was made from type 12X18H9T austenitic stainless steel of nominal composition (wt. %): C≤ 0.12; Cr -17-19. Ni -8-9.5; Mn ≤2; Si ≤0.8; Ti –0.5-0.7. The (wt.%) composition was checked using an x-ray micro-analyzer "Kamebax" and was found to be Cr – 18.5; Ni – 9.5; Mn – 1.5; Si – 0.6-0.8; Ti –0.6-07. Thus, the steel composition corresponds to the nominal specification.

The component was exposed without replacement or rotation for 46,536 h (from November, 1972 till June, 1984) in the BN-350 core at the radial distance of 94.5 cm from the core axis. The maximum neutron fluence at the core midplane was equal to 3.3×10^{23} n/cm^2 (E>0) or 1.6×10^{23} n/cm^2 (E>0.1 MeV). These fluences correspond to maximum neutron damage dose of 56 dpa at a maximum dose rate of 3.34×10^{-7} dpa/s. The relative values of the total and fast neutron fluence as well as dose in the component are shown in Figure 1.

The calculated distribution of irradiation temperatures for both nearest and farthest flats from the core axis is shown in Table 1. The distribution of irradiation temperature in the component was calculated at the average level of reactor capacity equal to 60% nominal reactor capacity for the period from 1973 to 1984. The inlet sodium temperature was 280°C. Throughout the irradiation period the average heating of sodium in surrounding subassemblies of the lateral breeder zone was ~60°C.

Cutting of specimens

From the data shown in Table 1 it follows that in each section of the component there is a complicated distribution of dose, neutron fluence and irradiation temperature. Due to different cooling conditions the maximum difference of temperature between internal and outer component surfaces reaches

Table 1. The distribution of irradiation temperature (°C) in different cross sections of the flow restrictor component

Distance from midplane, mm	Outer surface, inboard flat	Internal surface, inboard flat	Outer surface, outboard flat	Internal surface, outboard flat
-750	282	282	281	281
-450	290	287	288	286
-150	306	296	303	293
0	317	302	313	299
+150	324	304	321	301
+450	334	307	333	306
+750	337	307	336	306

30°C. The neutron fluence and dose between two arbitrary points in a cross section of the component may differ by factor of two and more.

In the hot cell of the BN-350 site the central section of the flow restrictor component was cut into 5 pieces, each of 300 mm length. The pieces designated #1, #3 and #5 (see Figure 2) corresponding to the bottom, middle and top parts of the component, were transported to the hot laboratory of IPPE. In Figure 2 a map is presented illustrating the accessible dose-temperature irradiation conditions for each component section. The areas of the map corresponding to absent pieces 2 and 4 are shaded. As seen in Figure 2., the accessible area of dpa and irradiation temperatures has a complicated form and is limited by doses of 4 and 56 dpa and irradiation temperatures of 282 and 335°C. Since the dpa-temperature areas corresponding to different pieces of the component overlap partially, this allows one to get some information that one would otherwise like to obtain from lost pieces #2 and #4.

To obtain the most complete information on swelling the scheme of cutting of TEM specimens shown in Figure 3 was chosen. To prepare specimens for electron microscopy investigation (disks of 3 mm in diameter and of 0.3-0.4 mm in thickness) several samples were cut out from each corner of the component (7 specimens) and from the middle of each face (5 specimens). The scheme of cutting of TEM specimens shown in Figure 3 was realized for three cross sections located at distances of 0, -150 and +590 mm from the core midplane. For the cross section located at the distance of -670 mm, TEM specimens were cut out only from three faces. Such a scheme of cutting the TEM specimens allowed us to fill rather uniformly the area of the dpa–irradiation temperature map with sufficient experimental points (shown as crosses in Figure 2).

Microstructure and swelling of 12X18H9T stainless steel

Data on irradiation conditions and swelling for the cross sections located at distances of -670, -150 and 0 mm from the core midplane are shown in Table 2. In Figure 4 the dose-irradiation temperature map of the void formation in type 12X18H9T stainless steel is shown. Out of 157 conditions examined, 111 specimens were found to contain voids.

The microstructure of 12X18H9T steel in the sections investigated is characterized by the presence of voids, dislocation loops, dislocation segments, two types of precipitates, and deformation stacking faults. Voids were observed in sections -150, 0 and +590 (Figure 5), but no voids were detected in sections -670 and - 450 mm. The void characteristics are listed in Table 2.

The dislocation structure of the irradiated steel consists of both faulted and perfect dislocation loops and linear dislocations (Figure 6). The total length of dislocations per unit volume depends only slightly on the irradiation temperature.

In the irradiated steel two types of precipitates were observed. The first type are spherical particles with the mean diameter of 58.7 nm and concentration of 5.0×10^{14} cm^{-3}. The volume fraction of these precipitates equals 0.72%. From electron diffraction patterns it appears that the diffraction reflections most likely correspond to TiC precipitates, most probably formed in the steel during solidification. It

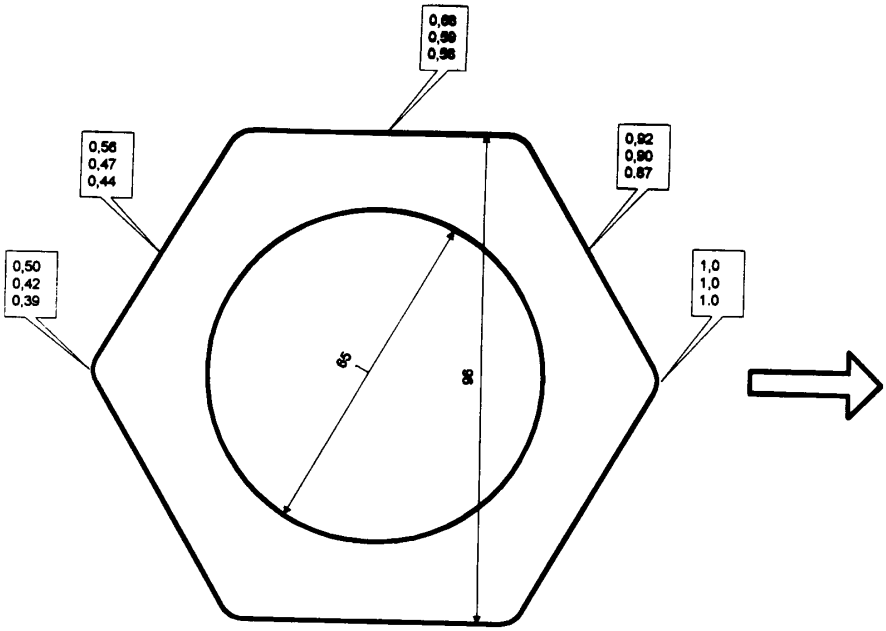

Figure 1. Normalized distribution (listed from the top downward) of neutron fluences E>0 and E>0.1 MeV and dpa dose over cross section of the BN-350 flow restrictor component. The arrow points toward the core axis.

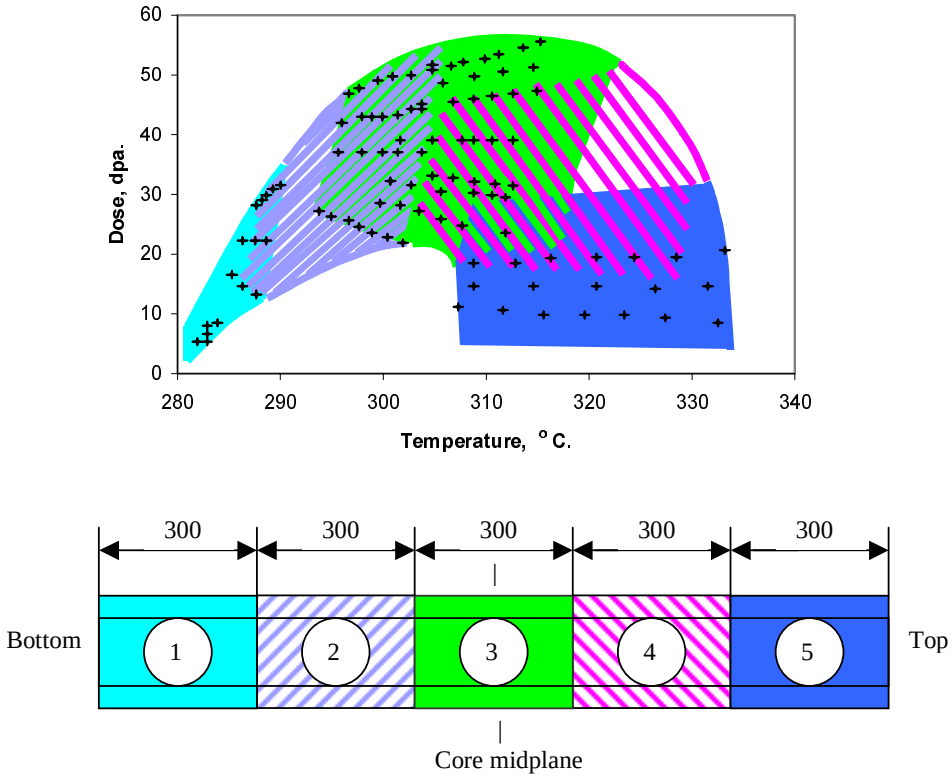

Figure 2. The dose-temperature map of irradiation conditions and the scheme of initial cutting of the flow restrictor component (lengths in mm).

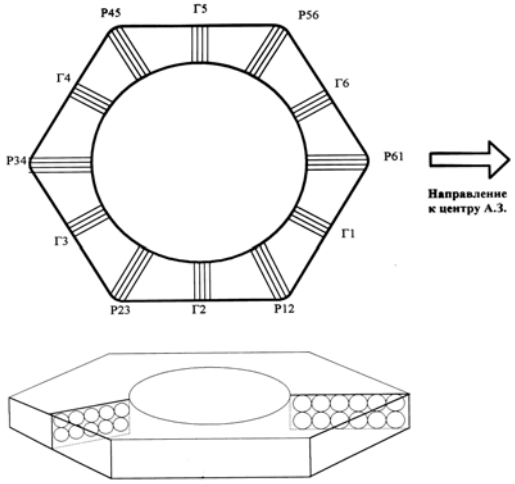

Figure 3. The scheme of cutting the TEM- specimens for component cross-sections located at distances of 0, -150 and +590 mm from the core midplane. Р and Г are derived from the Russian words for “corner” and “face” respectively. The Russian under the arrow note that it points to the core axis.

Table 2. Microstructural data for the 12Х18Н9Т steel

Sample number	Dose. dpa	Temperature. °C	Mean void diameter. nm	Void concentration. 10^{14} см$^{-3}$	Void volume fraction. %
-150_Р34.1	21.6	302	4.4	Voids in single grains	
-150_Р56.3	43.4	302	4.9	0.82	0.0008
-150_Р56.3	43.6	302	4.9	0.8	0.001
-150_Р61.3	50.3	302	5.1	1.2	0.001
-150_Р56.2	43.8	303	4.9	1.9	0.002
-150_Р56.2	44	303	4.9	1.9	0.002
-150_Р56.1	42.2	304	4.4	1.4	0.00144
-150_Р61.2	51.2	304	5.0	1.4	0.02
-150_Р56.1	44.5	305	4.4	1.4	0.0014
-150_Р61.1	52.1	305	4.8	1.7	0.02
0_Р34.4	25.7	306	7.9	1.5	0.006
0_Г4.3	30.5	306	5.2	0.5	0.001
0_Р23.4	32.5	307	6.4	0.78	0.002
0_Р56.5	45.5	307	4.7	1.96	0.002
0_Р61.5	51.7	307	4.7	1	0.001
+750_Р34.7	4.5	308	9.9	28	0.23
590_Р34.7	10.0	308	9.4	8.4	0.06
+590	10.3	308	8.1	12.6	0.056
+590_Р34.7	10.3	308	9.4	8.4	0.06
0_Р34.3	24.8	308	9.2	3.1	0.02
0_Г2.3	39.2	308	5.4	0.84	0.001
0_Г5.3	39.2	308	5.3	0.52	0.001
0_Р61.4/5	52.1	308	4.9	0.9	0.001
+750_Р61.7	7.9	309	10.7	21	0.19
590_Г5.5	13.7	309	9.5	6	0.04

590_Г2.5	13.7	309	8.0	6	0.03
+590_Г2.5	14.1	309	8.3	6	0.03
+590_Г5.5	14.1	309	9.5	6.3	0.04
590_61.7	17.5	309	9.0	8	0.05
+590_Р61.7	18	309	9.0	7.9	0.05
0_Г4.2	29.9	309	6.0	0.91	0.002
0_Р23.3	32.0	309	8.1	1.2	0.006
0_Г2.2/5	39.2	309	5.4	0.78	0.001
0_Р56.4	45.9	309	6.2	4.7	0.01
0_Г1.3	49.8	309	6.0	1.08	0.002
+750_Г2.5	6.2	310	9.7	14	0.1
0_Р61.4	52.6	310	5.0	1.4	0.002
0_Г4.1/5	29.5	311	7.0	2.1	0.007
0_Р23.2	31.6	311	8.5	2.9	0.013
0_Г2.2	39.2	311	6.6	1.7	0.004
0_Г5.2	39.2	311	6.6	1.8	0.005
0_Р56.3	46.4	311	6.2	4.75	0.01
+750_Р34.6	4.4	312	11.8	36	0.46
+590_Р34.6	9.9	312	9.0	21	0.12
+590	10.0	312	7.0	6	0.002
+590	10.3	312	7.5	9	0.003
0_Р34.1	23.0	312	9.0	7.1	0.044
0_Г3.1	29.2	312	8.7	0.28	0.001
0_Г4.1	29.2	312	8.0	2.6	0.012
0_Г1.2	50.6	312	6.6	2.7	0.006
0_Р61.3	53.6	312	5.9	4.5	0.009
+750_Р61.6	8.1	313	10.9	27	0.25
+590_Р61.6	18.3	313	10.1	22	0.19
0_Р23.1	31.1	313	9.1	2.1	0.013
0_Г2.1	39.2	313	8.7	0.85	0.004
0_Г5.1	39.2	313	7.2	8.6	0.024
0_Р56.2	46.8	313	6.9	13.9	0.037
0_Р61.2	54.5	314	6.7	10	0.026
+590	10.0	315	8.6	19	0.09
+590_Г2.4	14.1	315	9.0	15	0.09
+590_Г5.4	14.1	315	10.4	18	0.16
0_Р56.1	47.3	315	7.0	15.8	0.049
0_Г6.1	51.4	315	7.1	7.9	0.021
+750_Г2.4	6.2	316	14.0	15	0.3
+590_Р34.5	9.6	316	11.0	38	0.4
0_Р61.1	55.4	316	7.1	9.2	0.024
+750_Р34.5	4.2	317	12.8	33	0.53
+590_Р61.5	18.6	317	11.4	20	0.24
+750_Р61.5	8.2	318	11.1	27	0.27
+590	9.4	319	10.5	19	0.09
+590_Р34.4	9.3	320	13.1	37	0.65
+590	18.7	320	10.5	20	0.18
+750_Р34.4	4.1	321	13.7	23	0.60
+590_Г2.3	14.1	321	10.4	19	0.18
+590_Г5.3	14.1	321	11.8	22	0.3
560	16.8	321	12.4	12	0.17
+590	18.9	321	9.9	25	0.18
+590_Р61.4	19	321	12.5	27.5	0.44
+750_Г2.3	6.2	322	14.5	18	0.4
+750_Р61.4	8.4	322	11.2	21	0.23
+590_Р34.3	8.9	324	14.0	27	0.6

+750_Р34.3	3.9	325	18.0	22	0.9
+590_Р61.3	19.3	325	14.2	22	0.5
+750_Р61.3	8.5	326	16.5	16	0.5
+590	9.5	327	13.7	18	0.38
+590_Г2.2	14.1	327	11.1	29	0.32
+590_Г5.2	14.1	327	12.8	21	0.35
+750_Г2.2	6.2	328	15.4	19	0.53
+590_Р34.2	8.6	328	18.0	25	0.95
590_Р34.2	8.4	329	18.0	25	0.96
+590_Р61.2	19.6	329	14.0	21	0.45
+750_Р61.2	8.7	331	17.2	16	0.6
+750_Р34.2	3.8	332	18.3	19	0.9
+590_Р34-Г4	8.4	332	16.9	22	0.69
+590	8.9	332	14.5	26	0.57
+590	9.4	332	12.3	31	0.43
+590_Г5.1	14.1	332	15.0	24	0.67
+590_Г2.1	14.1	332	13.8	22	0.47
590	14.5	332	17.3	6.4	0.28
590_Р34.1	8.1	333	18.0	18	0.77
+590_Р34.1	8.3	333	17.0	20	0.70
590_Г2.1	13.7	333	14.0	22	0.50
590_Г5.1	13.7	333	15.0	24	0.70
+750_Г2.1	6.2	334	20.0	10	0.5
590_Р61-Г1.1.4	18.8	334	16.7	18	0.65
590_Р61-Г1.1.3	19.0	334	14.4	22	0.50
590_61.1	19.4	334	17.0	14	0.50
+590	19.8	334	12.4	28	0.43
+590_Р61.1	19.9	334	17.0	14	0.49
+750_Р61.1	8.8	335	17.3	16	0.6

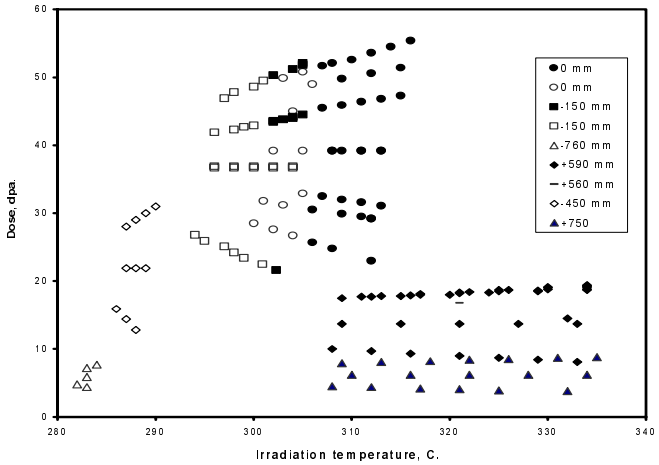

Figure 4. The dose-irradiation temperature map of void formation in the 12X18H9T steel irradiated in BN-350. Filled symbols indicate that voids were observed, and empty symbols signify no voids were present.

should be noted that this type of precipitate is observed in all investigated sections of the flow restrictor component. Another type of precipitate is much smaller, finely dispersed precipitates in the grain interior (Figure 7). Analysis has shown that these precipitates are G-phase, most likely induced by irradiation.

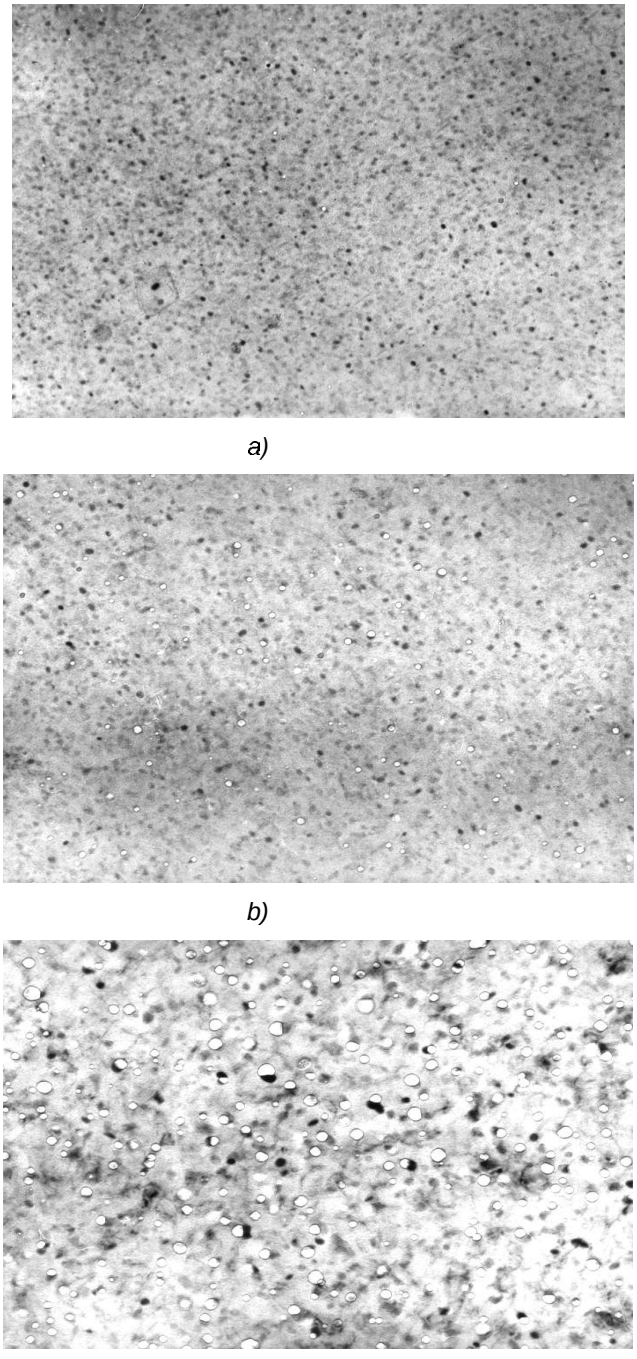

a)

b)

c)

Figure 5. Voids in 12X18H9T steel after neutron irradiation: a) at 302°C to 50.3 dpa, b) at 308°C to 10.3 dpa, and c) at 324°C to 8.9 dpa.)× 100,000.

Along with the defects mentioned above, flat stacking faults were observed in the irradiated steel (Figure 8), probably, due to deformation of TEM specimens during handling and thinning.

Results and discussion

In Figures 9 - 12 the temperature dependence of the mean void diameter $<d_v>$, void concentration N_v, void volume fraction and product $<d_v>N_v$ are shown. Despite significant scatter within the data field, it

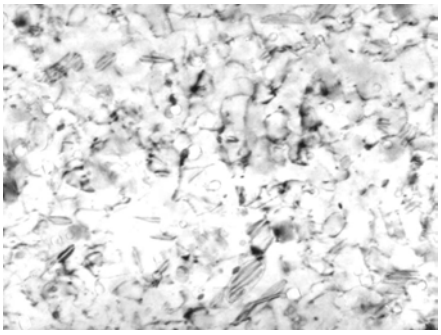

Figure 6. Dislocation structure of the 12X18H9T steel after neutron irradiation at 329°C to 19.6 dpa (cross section at +590 mm).

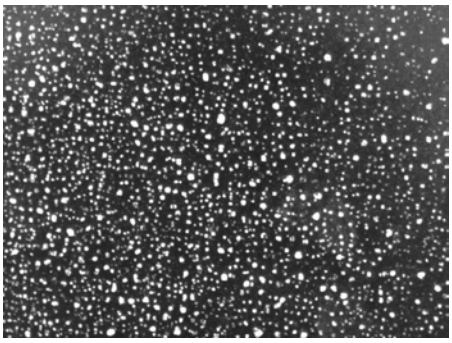

Figure 7. G-phase precipitates in the 12X18H9T steel after neutron irradiation: at 302°C to 27.6 dpa (cross section at 0 mm).

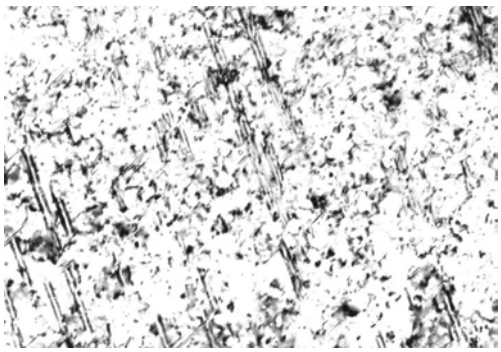

a)

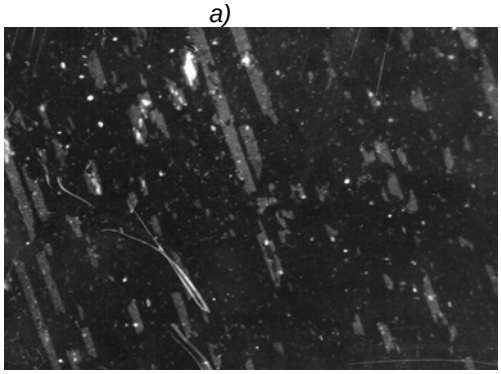

b)

Figure 8. Deformation stacking faults in the 12X18H9T steel after neutron irradiation at 314°C to 54.5 dpa (cross section at 0 mm). a) bright-field image, b) dark-field image.

is seen in Figure 9 that the mean void diameter increases monotonically with increase of irradiation temperature, with an activation energy of about 1 eV.

In contrast to the mean void diameter, the void concentration and void volume fraction appear to behave non-monotonically with increasing temperature, but this perception arises primarily from the shape of the dpa-temperature field shown earlier in Figure 2, but altered by the strong temperature dependence of swelling. A maximum swelling of ~1% was observed.

The increment of the yield strength caused by voids can be expressed in terms of void mean diameter $<d_v>$ and concentration N_v as follows: $\Delta\sigma_{0.2} = \alpha_v Gb\sqrt{< d_v > N_v}$, where G is the shear modulus, b the Burgers vector, α_v is the void barrier constant. It is seen in Figure 12, that the product of $< d_v >$ and N_v has a temperature maximum in the range of 323-330°C. Taking for steels G=60 GPa, b=0.25 nm and α_v=2.0, for magnitudes of <dv>Nv ranging from 3 $\times 10^{13}$ m^{-2} to 5 $\times 10^{13}$ m^{-2} one obtains that the increment of yield strength lies in the range from 160 MPa to 210 MPa, in excellent agreement with the difference of 160 to 200 MPa in yield strengths of 316 steel measured in Ref. [*3*] for irradiation temperatures of 60°C and 330°C. Thus, the maximum of the yield strength observed at 330°C for 316 steels can be attributed to hardening the material by voids formed at irradiation temperatures higher than 200°C.

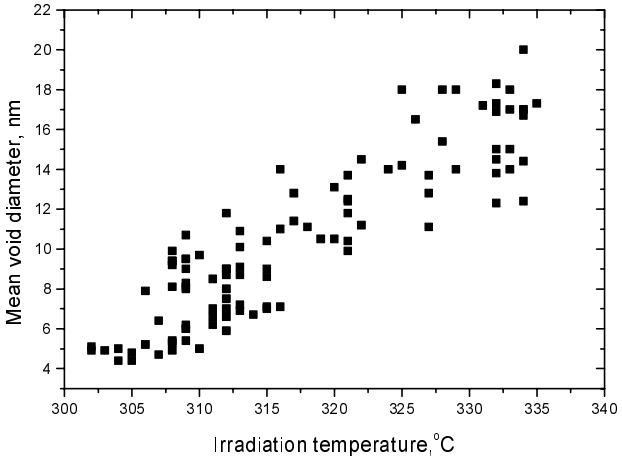

Figure 9. Temperature dependence of the mean void diameter.

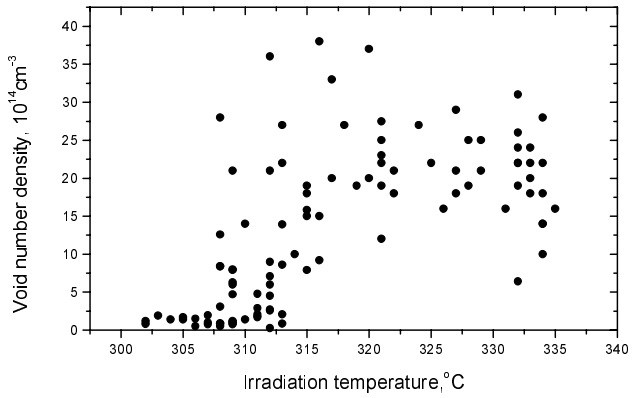

Figure 10. Temperature dependence of the void concentration.

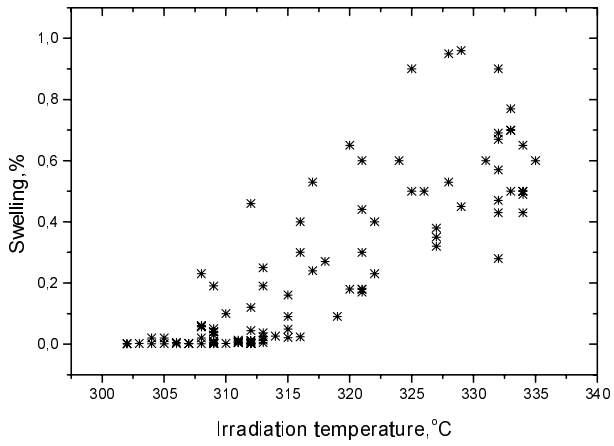

Figure 11. Temperature dependence of void swelling.

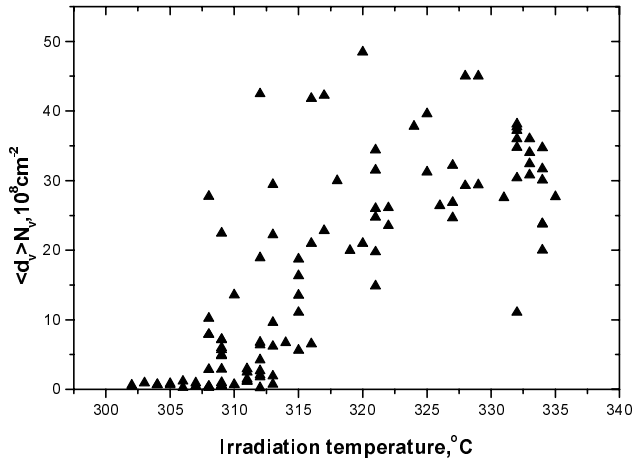

Figure 12. Temperature dependence of the product $<d_v>N_v$, determining the contribution of voids to the yield strength increment in the 12X18H9T steel.

Figure 13 shows that one of the major sources of data scatter arises from the flux dependence of void swelling. Note that when relatively small ranges of temperature are chosen, swelling appears to decrease with increasing dpa. This is a counterintuitive observation, but is consistent with the results of several recent studies showing that increases in the dpa rate delay the onset of accelerated swelling (4-6).

Another conclusion concerning the temperature range of void swelling can be seen in Figure 14 when comparing the swelling data from the flow restrictor with those data published earlier in various Russian journals, but derived from the BR-10 fast reactor. The inlet temperature of BR-10 during this period was ~420°C. It is obvious that the peak swelling temperature in BR-10 reflects more the peak in the flux profile across this relatively small core. The lower temperature limit of void swelling is only an artifact of the inlet temperature.

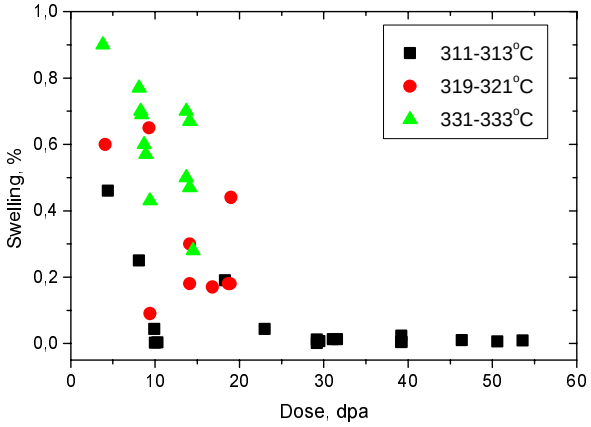

Figure 13. Dependence of swelling on temperature, dpa and dpa rate for selected small increments of temperature. Since the dpa rate is proportional to the dpa level in this constant time experiment, the data also suggest a strong dependence of swelling on dpa rate.

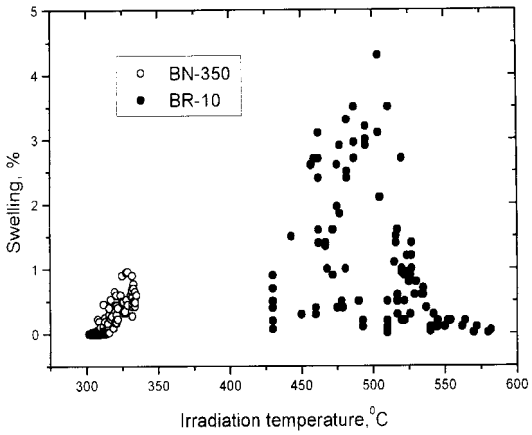

Figure 14. Comparison of swelling data for two fast reactors with very different inlet temperatures.

The lower temperature limit observed in the flow restrictor data set, however, is most likely a real lower limit determined by the severely limited vacancy migration at such a low temperature, and it is quite likely that there is a continuum in swelling not observable in the temperature range shown in Figure 14.

Conclusions

On the basis of the present microstructural study it is possible to make the following conclusions.

1. Voids in type 12X18H9T austenitic steel irradiated in the BN-350 fast reactor at dose rates ranging from 1.6×10^{-7} dpa/s to 3.1×10^{-7} dpa/s were observed in the temperature range of 302-334°C at doses ranging from 26.3 to 55.4 dpa. At lower irradiation temperatures voids resolvable by electron microscopy were not found, even though the dpa level approaches 50 dpa.
2. The mean void diameter increases monotonically with increasing neutron irradiation temperature in the range of 302°C - 334°C, from 4.4 - 5.1 nm at doses ranging from 22 to 50 dpa to14.4 – 17.0 nm at doses of 19-20 dpa.
3. At the temperature of 330°C and doses ranging from 8 to 20 dpa the swelling is between 0.3 and 1.0 %.

4. There appears to be some support in this data set to expect a reduction in swelling as the dpa rate increases, consistent with the results of other studies.

REFERENCES

[1] S. I. Porollo, A. N. Vorobjev, Yu. V. Konobeev, A. M. Dvoriashin, and F. A. Garner, "The Influence of PWR-Relevant Atomic Displacement Rates and Temperatures on Void Swelling in the Russian Equivalent of AISI 304 Stainless Steel", *International Symposium on "Contribution of Materials Investigation to the Resolution of Problems Encountered in Pressurized Water Reactors,* 14-18 Sept. 1998, Fontevraud, France, pp. 271-280.

[2] S. I. Porollo, Yu. V. Konobeev, A. M. Dvoraishin, V. M. Krigan and F. A. Garner, "Determination of the Lower Temperature Limit of Void Swelling of Stainless Steels at PWR-relevant Displacement Rates", *10th International Conference on Environmental Degradation of Materials in Nuclear Power Systems – Water Reactors,* 2001,in CD format only. Also published in Fusion Materials Semiannual Progress Report for Period Ending June 30, 2001, pp. 111-126.

[3] J. P. Robertson, I Ioka, A. F. Rowcliffe, M. L. Grossbeck and S. Jitsukawa, "Temperature Dependence of the Deformation Behavior of Type 316 Stainless Steel After Low Temperature Neutron Irradiation", *Effects of Radiation on Materials: 18th International Symposium, ASTM STP 1325*, R.E. Nanstad, M.L. Hamilton, F.A. Garner, and A.S. Kumar, Eds., American Society for Testing and Materials, West Conshohocken, PA, 1999, pp. 671-688.

[4] T. Okita, N. Sekimura, F. A. Garner, L. R. Greenwood, W. G. Wolfer and Y. Isobe, "Neutron-Induced Microstructural Evolution of Fe-15Cr-16Ni Alloys at ~400°C During Neutron Irradiation in the FFTF Fast Reactor", *10th International Conference on Environmental Degradation of Materials in Nuclear Power Systems – Water Reactors*, 2001, in CD format only.

[5] G. M. Bond, B. H. Sencer, F. A. Garner, M. L. Hamilton, T. R. Allen and D. L. Porter, "Void Swelling of Annealed 304 Stainless Steel at ~370-385°C and PWR-Relevant Displacement Rates", *9th International Conference on Environmental Degradation of Materials in Nuclear Power Systems – Water Reactors*, 1999, pp. 1045-1050.

[6] F. A. Garner, M. L. Hamilton, D. L. Porter, T. R. Allen, T. Tsutsui, M. Nakajima, T. Kido, T. Ishii, G. M. Bond and B. H. Sencer, to be submitted to *Journal of Nuclear Materials*.

THE EFFECT OF VOID SWELLING ON ELECTRICAL RESISTANCE AND ELASTIC MODULI IN AUSTENITIC STEELS - A. V. Kozlov, E. N. Shcherbakov, S. A. Averin (Research & Development Institute of Power Engineering Zarechny**,** Russia) and F. A. Garner (Pacific Northwest National Laboratory)*

OBJECTIVE

The objective of this effort is to determine for austenitic steels the impact of void swelling and precipitation on physical properties such as elastic moduli and thermal or electrical resistivity. The results of this study will allow the development of nondestructive diagnostic procedures for materials irradiated in either fission or fusion devices.

SUMMARY

Measurements are presented of electrical resistance and elastic moduli (Young's modulus and shear modulus) of stabilized austenitic fuel pin cladding after irradiation in the BN-600 reactor. Additional data are presented on changes in electrical resistivity of another stabilized austenitic steel irradiated in the BN-350. The elastic moduli are reduced and the electrical resistance is increased as the neutron dose increases. These changes are correlated with void swelling measured on the same specimens.

Dependencies of these changes in physical properties on neutron irradiation dose, temperature and swelling level are plotted and it is shown that to the first order, the property changes are dependent on the swelling level in agreement with earlier U.S. and Russian data, and also in agreement with various theoretical predictions. It is also observed, however, that changes in electrical resistance and elastic moduli frequently differ slightly for specimens with equal swelling, but which were obtained at different combinations of temperature and dose. These second-order differences appear to arise from contributions of other radiation-induced structural changes, especially in precipitation, which depends strongly on irradiation temperature in stabilized steels.

PROGRESS AND STATUS

Introduction

Nuclear power plants, both fission and perhaps fusion driven, can operate from 30 to 60 years under some circumstances, allowing near-core structural components to achieve radiation doses ranging from 10 to 120 dpa at irradiation temperatures varying from 280 to 400°C. Void swelling in this temperature range is a potential concern for further operation of such reactors [1,2]. Furthermore, much time is needed to accumulate high damage doses in existing facilities, and therefore experimental examination possibilities are somewhat limited, especially since it usually requires the removal of structural elements from the reactor that still serve as necessary operational components.

Another way to determine the state of swelling within a given plant component is to *in-situ* measure non-destructively properties affected by swelling. Such an approach requires a demonstration that swelling-induced changes induced in physical properties can indeed be measured and correlated with the swelling level. This paper demonstrates such swelling-sensitive dependencies, focusing on electrical resistance and elastic moduli of two stabilized austenitic steels after irradiation to high doses in several fast reactors.

Material and examination procedure

Two sets of specimens were examined. First, specimens of 20 mm length were cut from 1 mm diameter spacing wire irradiated in the BN-350 fast reactor. This wire is made of 0.1C-16Cr-15Ni-3Mo-1Nb austenitic steel and is wrapped in a spiral around fuel pins to provide spacing between adjacent pins. Average temperatures and irradiation doses of these specimens are listed in Table 1.

* Pacific Northwest National Laboratory (PNNL) is operated for the U.S. Department of Energy by Battelle Memorial Institute under contract DE-AC06-76RLO-1830.

The second set contains cladding tube specimens removed from two fuel elements designated "central" and "peripheral" according to their different location in the BN-600 fast reactor core. The cladding was made of 0.1C-16Cr-15Ni-3Mo-1Mn steel in the 20% cold-worked condition. Average temperatures and irradiation doses of these specimens are listed in Table 2. Tested specimens are 30 mm long, 6.9 mm outer diameter and 0.4 mm thickness. The fuel was removed before testing and the tube cleaned to remove contamination deposits. Table 3 contains the detailed composition of the two steels.

Electrical resistance *R* was determined by comparison of voltage reduction in a reference specimen and the measured specimen. The procedure of electrical resistance measurement is described in detail in Ref. [3]. The relative error in this measurement did not exceed 1%.

For measurement of elasticity characteristics (Young's modulus *E* and shear modulus *G*) an ultrasonic resonant method was employed. The method is based on excitation of ultrasonic oscillations, with measurement of natural frequencies of longitudinal and shear oscillations in the specimen [3]. Using dynamic elasticity theory, values of both Young's modulus *E* and shear modulus *G* were calculated using measured values of resonant frequencies. The error in the measurement did not exceed 1%.

Table 1. Average temperatures and neutron irradiation dose of 0.1C-16Cr-15Ni-3Mo-1Nb steel

T_{irr}, °C	595	580	560	530	495	440	335
D, dpa	40	46	45.5	43	35	32	28

Table 2. Average temperatures and neutron irradiation dose of 0.1C-16Cr-15Ni-3Mo-1Mn steel

Central fuel element cladding									
T_{irr}, °C	370	431	439	488	500	522	561	570	586
D, dpa	3	53	56	69	71	72	70	68	63
Peripheral fuel element cladding									
T_{irr}, °C	370	427	435	510	518	567	586		
D, dpa	3	52	55	69	69	65	63		

Table 3a. Chemical composition of fuel pin cladding of 0.1C 16Cr-15Ni-2Mo-1Mn steel

Element	C	Cr	Ni	Mo	Mn	Si	Ti	V	B	N	Co	P	S
wt %	0.06-0.07	15.9-16.7	14.0-14.7	2.09-2.24	1.4 1.6	0.39-0.50	0.30-0.41	0.10-0.24	0.001-0.003	0.009-0.015	0.004-0.010	0.006-0.018	0.003-0.007

Table 3b. Chemical composition of spacing wire of 0.1C-16Cr-15Ni-3Mo-1Nb steel

Element	C	Cr	Ni	Mo	Mn	Nb	Si	Ti	B	N	P	S
wt %	0.04-0.06	15.0-16.5	15.0-16.0	2.7 - 3.2	0.4 - 0.8	0.6 0.7	0.3 - 0.6	0.05	0.002	0.03	0.02	0.010

The void swelling *S* in % was determined by hydrostatic weighing to determine the density by

$$S = (\delta_0 / \delta - 1) \cdot 100\% \quad (1)$$

where δ_0 and δ are the density in the initial state and after irradiation, respectively. The error in the measurement did not exceed 0.02 g/cm^3.

Values of both electric resistance and swelling were measured on the spacing wire specimens. Similar measurements were made on the tube specimens, but elastic moduli also were determined. All measurements were performed in hot cells.

Results

Figure 1 presents the temperature dependence of swelling and the relative change in electrical resistance of the 0.1C-16Cr-15Ni-3Mo-1Nb spacing wire irradiated in the BN-350 fast reactor. The correlation of the two dependencies is quite obvious. Peak swelling was 9.5% in this specimen set, achieved at a dose of 43 dpa and an irradiation temperature of 540°C. The resultant effect on electrical resistance was an increase of 8.2%.

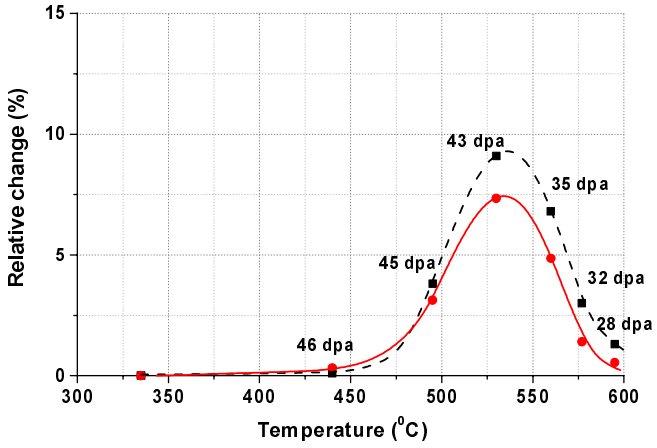

Figure 1. Dependence of swelling (■ - S) and relative changes in electrical resistance (● - $\Delta R/R_0$) on irradiation temperature for 0.1C-16Cr-15Ni-3Mo-1Nb austenitic steel irradiated in the BN-350 reactor.

Figure 2 shows the measurement results for cladding specimens of 0.1C-16Cr-15Ni-2Mo-1Mn irradiated in the BN-600 reactor. The peak swelling of peripheral fuel element specimens was 7%, the resultant electrical resistance was increased 6.2%, while Young's modulus and shear modulus were each reduced 15%. The central fuel element cladding had a value of peak swelling of 13.6%, an increase in electrical resistance of 8.3%, and reductions of Young's modulus and shear modulus of 21.1% and 25%, respectively.

Changes in electrical resistance, Young's modulus and shear modulus obviously correlate with swelling for both sets of cladding. Moreover, the relative changes in elastic moduli are approximately two times larger than the concurrent change in electrical resistance.

Discussion

Changes in physical and mechanical properties of irradiated metallic materials are caused by changes in their microstructure and elemental composition of the alloy matrix, [4]. Formation of voids and second-phase precipitates, along with a modification of the dislocation microstructure are the major microstructural factors affecting moduli and resistivity. Additionally, second order contributions may arise from point defect populations and their impact on the distribution of alloying elements, which can

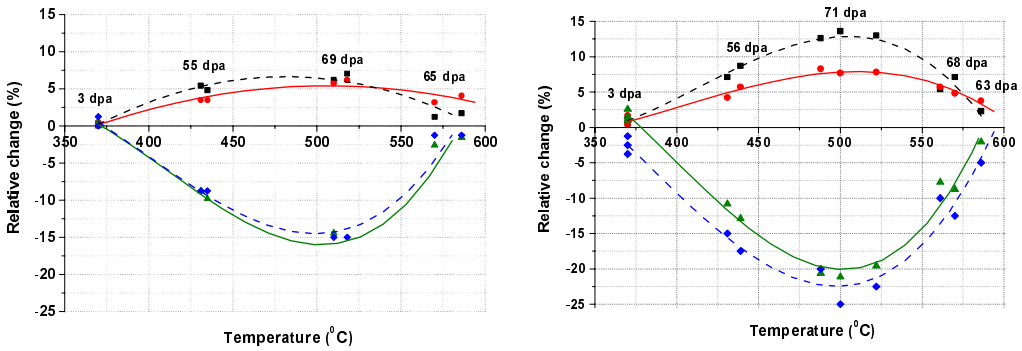

a b

Figure 2. Dependence of swelling (■ - S) and relative changes in electrical resistance(● - $\Delta R/R_0$), Young's modulus (▲ - $\Delta E/E_0$) and shear modulus (♦ $\Delta G/G_0$) on irradiation temperature for 0.1C-16Cr-15Ni-3Mo-1Mn steel (20% c.w.) irradiated in the BN-600 reactor; a – peripheral fuel element, b - central fuel element.

serve as scattering centers for moving electrons in the alloy matrix.

Changes in electrical resistance

Voids can be viewed as second phase particles with zero conductivity. The aggregate electrical resistance of a two-phase system (a system of a single-phase matrix with unconnected second phase particles) is determined by the equation described in [5].

$$\gamma = \gamma_0 \cdot (1 + \frac{c}{(1-c)/3 + \gamma_0/(\gamma_1 - \gamma_0)}) \tag{2}$$

where γ is specific electric conductivity of an alloy, γ_0 and γ_1 are electric conductivities of the matrix and second phase, respectively, and c and $(1-c)$ are volume contents of the second phase and matrix phases. For the case of voids $\gamma_1 = 0$, the volume content c is the porosity P. Taking into account that $\rho = 1/\gamma$, the aggregate resistance has the following description,

$$\rho = \rho_m \cdot \frac{(2+P)}{2 \cdot (1-P)} \tag{3}$$

where ρ_m is specific resistance of the matrix phase. Expressing porosity P through the fractional swelling S_f the following equation can be written.

$$\frac{\rho}{\rho_m} = \frac{3 \cdot S_f + 2}{2} \tag{4}$$

To express relative change in electric resistance, it is necessary to take into account an increasing of cross-section area F of an irradiated specimen in comparison with the cross-section of an unirradiated specimen F_0 arising from swelling.

$$F = F_0 \cdot (1 + \frac{2}{3} \cdot S_f) \tag{5}$$

Using equations (4) and (5) and expressing the electrical resistance *R* in terms of its specific electrical resistance and the specimen size, the final equation is attained.

$$\frac{\Delta R}{R_o} = \frac{\rho / \rho_o - F / F_o}{F / F_o} = \frac{5 \cdot S_f}{4 \cdot S_f + 6} \qquad (6)$$

Figure 3a shows the relationship between changes in electrical resistance and swelling for specimens of 0.1C-16Cr-15Ni-3Mo-1Nb steel irradiated in BN-350, and also shows the predicted dependence on swelling describing by equation (6). The similar dependencies for specimens of 0.1C-16Cr-15Ni-3Mo-1Mn steel irradiated in the BN-600 are shown in Figure 3b. One can see that dependence of relative changes in electrical resistance on swelling for different steel and initial thermal treatment and irradiated in different reactors is in good agreement with equation (6). At the same time it should be noted that are some differences.

Specimens of 0.1C-16Cr-15Ni-3Mo-1Mn steel irradiated above 570°C in general have higher electrical resistance compared with the value predicted by equation (6). Formation of rather large G-phase precipitates at these higher temperatures is most likely the cause of this divergence [5]. Precipitates of this phase are small and their volume fraction is much lower at temperatures near 400°C, as shown in Figure 4a. The size of G-phase precipitates and their volume fraction increases as temperature increases, as seen in Figure 4b. G-phase is known to contain 42-57% of nickel and to concentrate other elements such as silicon, removing these elements from the alloy matrix [7]. According to data on physical properties of Ni-based alloys [8] the electrical resistance of such precipitates may be on 30 – 50% higher than that of the original matrix. Of course there are concurrent changes in the matrix composition and the aggregate change will reflect the sum of these two contributions.

Considerable changes in relative distribution of various elements are also observed at high swelling levels, especially at void surfaces, a process which may also result in changes in aggregate electrical resistance.

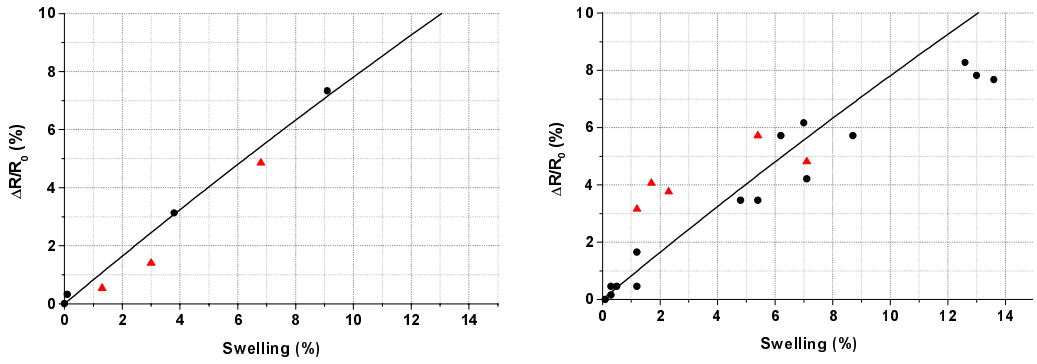

a b

Figure 3. Dependence of relative changes in electrical resistance on swelling of 0.1C-16Cr-15Ni-3Mo-1Nb steel irradiated in the BN-350 reactor (a) and 0.1C-16Cr-15Ni-2Mo-1Mn (20% c.w.) steel irradiated in the BN-600 reactor (b): ● - low-temperature range T_{irr}<530°C, ▲ - high-temperature range T_{irr}> 530°C; —— - dependence calculated by the equation (6).

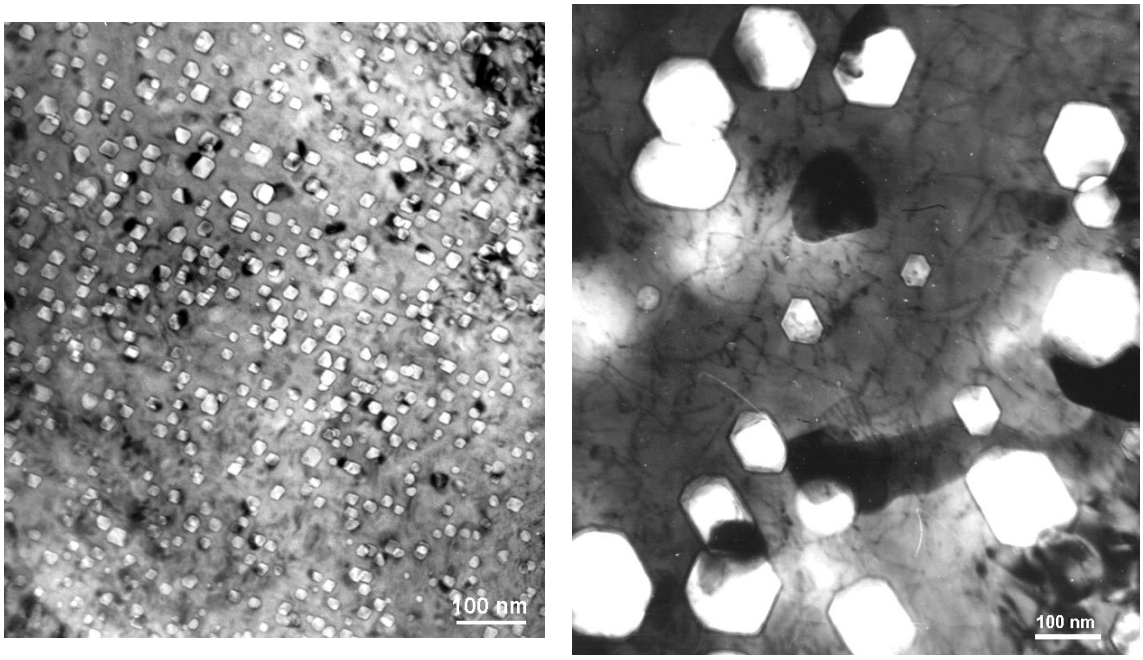

a b

Figure 4. G-phase precipitates in 0.1C-16Cr-15Ni-2Mo-1Mn steel irradiated in the BN-600: a – $T_{irr.}$= 420°C, D = 49 dpa; b – $T_{irr.}$= 580°C, D= 65 dpa.

Changes in elastic moduli

Similarly, in order to examine Young's modulus *E* of metal materials containing voids we apply the same two-phase material approach. Voids are considered to be particles of second phase with *E=0*. The modified equation for Young's module is [8].

$$E_i = E_m \cdot (1 - P) \tag{7}$$

where E_i is Young's modulus of an irradiated material containing voids, and E_m is Young's modulus of the unvoided matrix.

Young's modulus is calculated by equation [4] during determination of elastic characteristics by the ultrasonic resonant method.

$$E = 4 \cdot \delta \cdot l^2 \cdot f^2 \tag{8}$$

where δ is the density, *l* is the specimen length, *f* is the value of the first harmonic of resonant frequencies of longitudinal oscillations in the specimen.

The value δ was determined by hydrostatic weighing and δ is the average density including voids. At the same time density is included into formula (8) describing the propagation of sound speed in the matrix. Therefore, formula (8) for the case of porous materials expresses the effective value of Young's modulus, which is different from the value in formula (7).

$$E_i = E \cdot \frac{\delta_m}{\delta} = E \cdot (1 + S_f) \tag{9}$$

Using (7), (9) and the relationship of swelling to porosity, equation (10) can be written as follows.

$$\frac{\Delta E}{E_0} = \frac{E_m}{E_0} \cdot \frac{1}{(1+S_f)^2} - 1 \qquad (10)$$

Equation (10) transforms into equation (11) without taking into account changes in matrix Young's modulus.

$$\frac{\Delta E}{E_0} = \frac{1}{(1+S_f)^2} - 1 \qquad (11)$$

The same procedure may be used to assess void-induced changes in the shear modulus. Note that at low swelling levels this equation is approximated by a linear decrease in modulus of 2% per 1% swelling.

Figure 5 presents the dependence on swelling of experimentally derived values of relative change in Young's modulus. Predictions based on equation (11) are also shown and are in relatively good agreement with experimental data. There are some differences in prediction and measurement, however, especially at low swelling levels, where other changes such as segregation and precipitation overwhelm the void contributions to changes in modulus. It should also be noted that small changes in density usually result from precipitation.

Finally, the results presented above can be compared with those of previous studies conducted on irradiated metals. There were two previous experimental studies conducted in the U.S. fast reactor program in the early 1970s showing that the shear and Young's modulus decreased ~2% for each percent of swelling (10,11). These results are in good agreement with our results, where at low swelling levels the contribution is essentially linear with swelling content at ~2% reduction per percent swelling.

Various experimental studies conducted in the U.S. fusion materials program showed that the electrical resistivity of copper alloys increased ~1% for each percent of swelling (12-18). Once again these results are consistent with our results and theoretical prediction.

In particular it was shown by Garner and coworkers (13-18) that it was possible to separate the effects of voids and transmutant elements strongly formed in pure copper and various copper alloys during high fluence irradiation. Such separation of contributions arising from voids and other microstructural

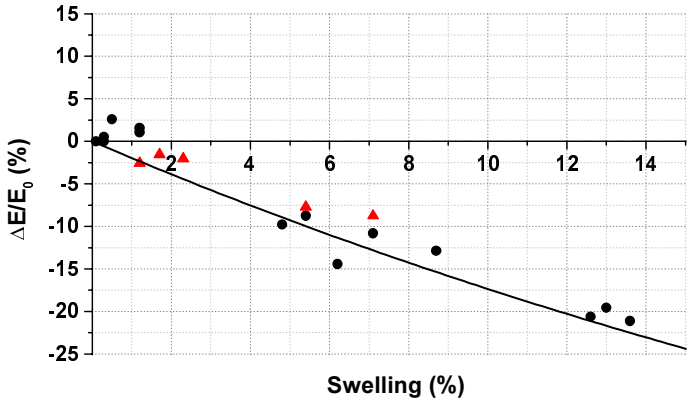

Figure 5. Dependence of relative changes in Young's modulus on swelling of 0.1C-16Cr-15Ni-2Mo-1Mn steel irradiated in the BN-600: ● - low-temperature range $T_{irr.}$<530°C, s - high-temperature range T_{irr}> 530°C, —— - dependence calculated by the equation (11).

or microchemical features lies at the heart of the technical challenge required to measure swelling in-situ during reactor downtimes. When the steel is not stabilized, however, precipitation-induced contributions will be smaller. Fortunately, the AISI 304 and 316 steels used in the U.S.A. are not stabilized, and therefore are much less prone to form precipitates, especially at the temperatures <400°C experienced in light-water cooled power reactors.

Conclusions

- High dose neutron irradiation at elevated temperatures causes swelling of austenitic steels, which is a dominating effect in changing not only the volume of the metal, but also causing significant and measurable changes in both electrical resistance and elastic moduli.
- Measured changes in electrical resistance are reasonably well described by an equation, which includes only the swelling contribution, and is relatively independent of steel composition, starting condition and irradiation conditions.
- Measured changes in elastic moduli are also well described by an equation in which swelling is the single parameter.
- The changes induced in elastic moduli by a given amount of swelling are approximately twice that induced in the electrical resistance.
- Deviations from void-based predictions are the result of other microstructural components, especially radiation-induced precipitates, and can lead to both over-predictions or under-predictions, depending on the property being measured, the steel composition, and especially the irradiation temperature.
- It appears to be feasible to use the changes induced by voids in these physical properties to nondestructively measure void swelling in-situ in a reactor.
- It also appears that the different responses of the physical properties may allow separation of the void and precipitate contributions. Additional microstructural and microchemical analysis is required on a variety of steels and irradiation conditions in order to facilitate this separation.

REFERENCES

[1] F. A. Garner, L. R. Greenwood, and D. L. Harrod, "Potential high fluence response of pressure vessel internals constructed from austenitic stainless steels", Proc. Sixth Intern. Symp. on Environmental Degradation of Materials in Nuclear Power Systems - Water Reactors, San Diego, CA. August 1-5, 1993, pp. 783-790.

[2] S. I. Porollo, A. N. Vorobjev, Yu V. Konobeev, A. M. Dvoriashin, V. M. Krigan, N. I. Budylkin, E. G. Mironova, and F. A Garner, "Swelling and void-induced embrittlement of austenitic stainless steel irradiated to 73 - 82 dpa at 335 - 365°C," *Journal of Nuclear Materials* 258-263 (1998), pp. 1613-1617.

[3] S. A. Averin, I. M. Kostousov, E. V. Serovikova, and E. N. Shcerbakov, "Methods and equipment for physical and mechanical properties researches," *VANT, series: Nuclear Technical and Technology,* Vol. 3, 1992, pp. 43-51 (in Russian).

[4] The directory, "Material since steel", M. L. Bernshtain, Eds., pub. Energyizdat, Vol. 1, book 2, Moscow, 1995 (in Russian).

[5] B. G. Liphshits, V. S. Karposhin, and Y. L. Linetskiy, "Physical properties of metals and alloys", Metallurgy, Moscow, 1980 (in Russian).

[6] W. J. S Yang, "Precipitate evolution in type 316 stainless steels irradiated in EBR-II" *Radiation-Induced Changes in Microstructure: 13th International Symposium, ASTM STP 955,* Philadelphia, 1987, pp. 628-646.

[7] A. F. Rowcliffe, and E. H. Lee, "High temperature radiation damage phenomena in complex alloys" *Journal of Nuclear Materials* 1982, Vol. 108&109, pp. 306-318.

[8] Handbook on, "Physical properties steels and alloys used in the power industry", B. E. Neymark, Eds., Energy, Moscow, 1967, (in Russian).

[9] P. G. Cheremskoi, V. V. Slezov, and V. I. Betehin, "Voids in solids", Energoatomizdat, Moscow, 1990 (in Russian).

[10] J. L. Straalsund, and C. K. Day, Nuclear Technology 20 (1973) 27.

[11] M. Marlow, and W. K. Appleby, Transactions ANS 16 (1973) 95-96.

[12] M. Ames, G. Kohse, T. S. Lee, N. J. Grant, and O. K. Harling, Journal of Nuclear Materials 141-143 (1986) 174-178.

[13] H. R. Brager, H. L. Heinisch, and F. A. Garner, "Effects of neutron irradiation at 450°C and 16 dpa on the properties of various commercial copper alloys," J. of Nucl. Mater., 133 & 134, (1985), pp. 676-679.

[14] F. A. Garner, H. R. Brager, and K. R. Anderson, "Neutron-induced changes in density and electrical conductivity of copper alloys at 16 to 98 dpa and 430°C", J. of Nucl. Mater., 179-181 (1991) 250-253.

[15] F. A. Garner, M. L. Hamilton, T. Shikama, D. J. Edwards, and J. W. Newkirk, "Response of solute and precipitation-strengthened copper alloys at high neutron fluence", J. of Nucl. Mater. 191-194 (1992), pp. 386-390.

[16] D. J. Edwards, K. R. Anderson, F. A. Garner, M. L. Hamilton, J. Stubbins, and. A. S. Kumar, "Irradiation performance of GlidCop dispersion-strengthened copper alloys to 100 dpa", J. of Nucl. Mater. 191-194 (1992), pp. 416-420.

[17] L. R. Greenwood, F. A Garner, and D. J. Edwards, "Calculation of transmutation in copper and comparison with measured electrical properties", Proc. Eighth ASTM-Euratom Symposium on Reactor Dosimetry, Vail, CO. Aug 29-Sept 3, 1993, ASTM STP 1228, pp. 500-508.

[18] D. J. Edwards, F. A. Garner, and L. R. Greenwood, "Influence of transmutation, void swelling and flux/spectra uncertainties on the electrical properties of copper and copper alloys," J. of Nucl. Mater., 212-215 (1994) 404-409.

The Primary Origin of Dose Rate Effects on Microstructural Evolution of Austenitic Alloys during Neutron Irradiation - T. Okita, T. Sato, N. Sekimura (The University of Tokyo), F. A. Garner and L. R. Greenwood (Pacific Northwest National Laboratory)*

OBJECTIVE

The objective of this effort is to determine the microstructural origins of the observed strong dependence of void swelling in austenitic alloys on dpa rate at 400°C.

SUMMARY

The effect of dose rate on neutron-induced microstructural evolution was experimentally estimated. Solution-annealed austenitic model alloys were irradiated at ~400°C with fast neutrons at seven different dose rates that vary more than two orders of magnitude. Two different doses were achieved at each dose rate. Both cavity nucleation and growth were found to be enhanced at lower dose rate. Based on a simple assumption concerning the experimental data, the net vacancy flux is calculated from the growth rate of cavities that had already nucleated during the first cycle of irradiation and grown during the second cycle. Using this approach the net vacancy flux was found to be proportional to $(dpa/sec)^{1/2}$ up to 28.8 dpa and 8.4×10^{-7} dpa/sec. This implies that mutual recombination dominates point defect annihilation in this experiment, even though point defect sinks such as cavities and dislocations were well developed. Thus, mutual recombination is thought to be the primary origin of the effect of dose rate on microstructural evolution, although the recombination distance is large and requires a new mechanism for recombination.

PROGRESS AND STATUS

Introduction

Blanket structural component materials in fusion reactors are expected to be exposed for long periods to neutron spectra generated by 14 MeV neutrons, often at dose rates lower than that characteristic of fast reactors. Accelerated irradiation testing conducted at high dose rates in fission reactors is one of the ways to achieve the same cumulative dose levels as required for fusion conditions. However, it is known that dose rates strongly affect microstructural evolution [1-5] and resultant macroscopic property changes [5-7]. It is therefore very important to evaluate the effect of dose rate on microstructural evolution and to develop models incorporating dose rate effects allowing assessments of irradiation performance of fusion materials.

The objective of this study is to experimentally clarify the primary origin of the effect of dose rate on microstructural evolution. Several solution-annealed austenitic alloys were irradiated at actively controlled temperatures with fast neutrons at seven different dose rates over a wide range of dose rate, and showed a very strong influence of dpa rate on the transient regime of swelling [5}. The results of further microstructural examination of one alloy are presented in this paper.

Experimental Procedure

Pure Fe-15Cr-16Ni (at%) with no added solute was prepared by arc melting from high purity Fe, Ni, and Cr. The ternary alloy was rolled to sheets of 0.25 mm thickness, cut into 3 mm disks and annealed for 30 minutes at 1050°C in high vacuum. Identical specimens are placed in seven different positions of the Materials Open Test Assembly (MOTA), ranging from below the core to above the core of the Fast Flux Test Facility (FFTF). The first irradiation sequence occurred in Cycle 11 of MOTA-2A for 2.58×10^{7} sec,

* Pacific Northwest Laboratory (PNNL) is operated for the U.S. Department of Energy by Battelle Memorial Institute under contract DE-AC06-76RLO-1830.

Table 1. Irradiation Conditions in Cycle 11 and Cycle 12.

Dose Rate, dpa/sec		Dose, dpa		Temperature, ˚C	
#11	#12	#11	#11 & #12	#11	#12
1.7 x 10^{-6}	1.4 x 10^{-6}	43.8	67.8	427	408
7.8 x 10^{-7} 1	9.5 x 10^{-7}	20.0 1	32.4	390	387
5.4 x 10^{-7}	8.4 x 10^{-7}	14.0	28.8	430	424
3.1 x 10^{-7} 2	3.0 x 10^{-7}	8.05 2	11.1	411	410
9.1 x 10^{-8}	2.1 x 10^{-7}	2.36	6.36	430	431
2.7 x 10^{-8}	6.6 x 10^{-8}	0.71	1.87	434	437
8.9 x 10^{-9}	2.2 x 10^{-8}	0.23	0.61	436	444

and a subset of specimens was then removed. Other identical specimens continued in Cycle 12 of MOTA-2B for 1.71 x 10^{7} sec. The dose rates ranged from 8.9 x 10^{-9} to 1.7 x 10^{-6} dpa/sec. The dose levels varied from 0.23 to 43.8 dpa in Cycle 11 and 0.38 to 24.0 dpa in Cycle 12. Table 1 summarizes the irradiation conditions. Microstructural evolution in these specimens was examined using a transmission electron microscope operated at 200kV.

Results

Figure 1 shows the cavity density as a function of cumulative dose. The cavity density increases with dose at all dose rates from 8.9 x 10^{-9} to 1.7 x 10^{-6} dpa/sec. However, both the absolute value and the rate of increase in cavity density are higher at lower dose rates, indicating that lower dose rates enhance cavity nucleation.

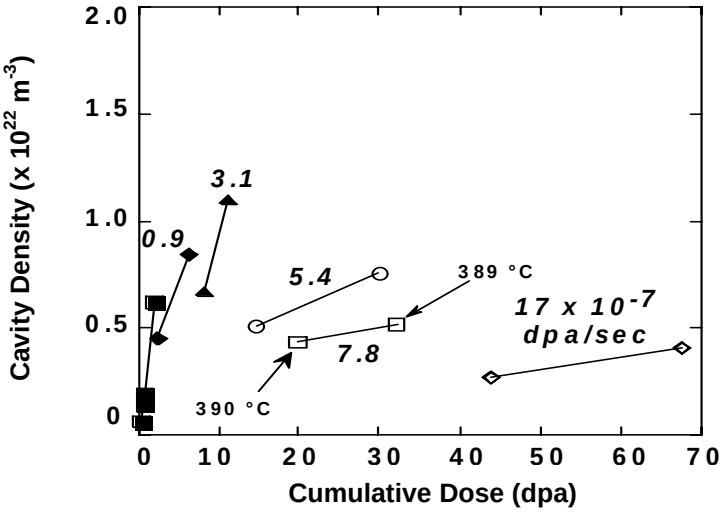

Figure 1. Cavity densities of Fe-15Cr-16Ni irradiated over a wide range of dose rates as a function of cumulative dose. The dose rates in Cycle 11 are noted in the figure. With the exception of a data set at ~390°C, all other data were generated at 411 to 444°C.

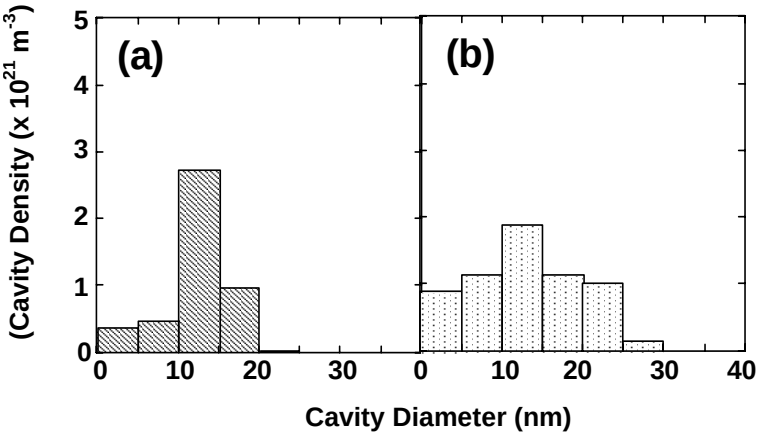

Figure 2. Comparison of cavity size distribution at similar cumulative dose levels. (a) Higher dose rate, 1 cycle of irradiation in Cycle 11, 8.05 dpa, 3.1 x10^{-7} dpa/sec at 411 °C; (b) Lower dose rate, 2 cycles of irradiation in Cycles 11 and 12, 2.36 dpa, at 9.1 x10^{-8} dpa/sec and 430°C in Cycle 11, and 4.0 dpa at 1.5 x10^{-7} dpa/sec and 431°C in Cycle 12, with a cumulative dose of 6.36 dpa.

Figure 2 shows a comparison of cavity size distributions for a lower dose rate of 1.5 x 10^{-7} dpa/sec and a higher dose rate of 3.1 x 10^{-7} dpa/sec, both at a cumulative dose level of ~7 dpa. Cavities with diameter greater than 35 nm can be observed only at the lower dose rate, indicating that cavity growth is also enhanced at low dose rate. It is also notable that a higher density of small cavities with diameter less than 10 nm can be observed at the lower dose rate, indicating continuous operation of cavity nucleation. Simultaneous enhancement of both cavity nucleation and growth therefore causes accelerated swelling at lower dose rates, as shown in Figure 3. Note that the swelling data in Figure 3a were derived from microscopy observation below 10% swelling, and from immersion density measurement above 10%, as presented earlier [5]. Microscopy at large swelling levels usually leads to significant intersection and attack of voids near specimen surfaces, and thus an underestimate of swelling compared to density changes, as shown in Figure 3b.

Note in Figure 3a that this alloy has attained or is approaching the characteristic steady state swelling rate of ~1%/dpa [8,9], and this post-transient swelling rate does not appear to be affected by the dose rate. The transient regime of swelling varied from <1 to ~60 dpa when the dose rate varied over more than two orders of magnitude. The control temperatures of the seven capsules varied from 389 to 444°C and may have influenced the swelling behavior somewhat. At a fixed dose rate, higher temperature is known to yield higher swelling based on a previous study in this experimental series by Sekimura et. al. that showed the peak swelling temperature of this alloy at 1.7 x 10^{-6} dpa/sec to lie at ~500˚C [10,11]. However, as shown in Figure 4a, for two separate cases the incubation dose of swelling at lower dose rate and lower temperature is shorter than that at higher temperature and higher dose rate. This indicates that dose rate is more important that the variation of irradiation temperature. Figure 4b shows the swelling as a function of cumulative dose at a very limited temperature range of 437 ± 7˚C. Clearly shown is the strong enhancement of swelling at lower dose rate.

Discussion

Microstructural observation shows that cavities in this ternary alloy are homogeneously distributed in the matrix at every irradiation condition, implying that the point defect flux is homogeneous throughout the matrix. In the following analysis larger cavities observed after 2 cycles are assumed to have nucleated and started to grow in the Cycle 11 stage of irradiation, while smaller cavities nucleated during Cycle 12 and growing during the remainder of Cycle 12.

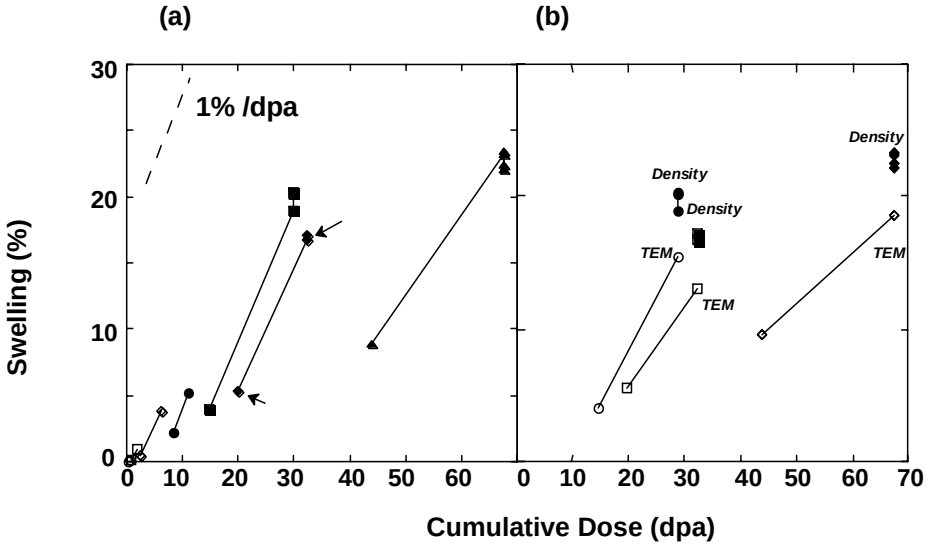

Figure 3. Swelling over a wide range of dose rates as a function of cumulative dose: (a) swelling determined by microscopy and density, as originally shown in reference 5, and (b) comparison of swelling between microscopy observation and immersion density measurement at swelling levels >10%. Note that swelling determined by density is larger than that by microscopy.

Cavities observed after the second cycle of irradiation can therefore be assumed to be divided into the following two categories; ‘earlier cavities‘, that nucleated during the first cycle of irradiation, and ‘recent cavities‘ that nucleated during the second cycle. Figure 5 shows one example of the cavity size distribution divided into earlier and recent cavities. When the diameters are plotted of ‘earlier cavities‘, which determine the largest portion of the swelling, it is clearly shown in Figure 6 that cavity growth is enhanced at low dose rates.

Employing the rate equation approach [12-14], the change of cavity diameter is written as follows;

$$\frac{dr}{dt} = \frac{1}{r} \bullet \left(Z_{vv} D_V C_V - Z_{vi} D_i C_i \right) \qquad 1.0$$

where r is the cavity radius, $D_{v,i}$ is the diffusion efficiency of vacancies (v) and interstitials (i), and $C_{v,i}$ is the point defect concentration of vacancies (v) and interstitials (i), $Z_{vv,v}$ is the bias factor of cavities for vacancies (v) and interstitials (i).

From equation (1,0) the difference between vacancy and interstitial flux, i.e. the net vacancy flux, is written as;

$$= \bar{r} \bullet \frac{dr}{dt} \qquad 2.0$$

Where, $\bar{r}$ is the average diameter of ‘earlier cavities‘ during the second cycle of irradiation. Figure 7 shows the calculated dose rate dependence of the net vacancy flux from the growth rate of ‘earlier cavities‘. The net vacancy flux is found to be proportional to $(\text{dpa/sec})^{1/2}$ up to 28.8 dpa and 8.4×10^{-7} dpa/sec. It is known that the point defect concentrations are proportional to $(\text{dpa/sec})^{1/2}$ in the recombination-dominant regime [12-17]. This indicates that mutual recombination appears to dominate point defect annihilation up to 30 dpa, even though in this experiment, the point defect sink population is well developed, with the dislocation sink strength as high as 7.11×10^{14} m^{-2} and the cavity sink strength

as high as 1.47 x 10^{15} m^{-2} [5,7], although the increase rates of these populations are strongly dependent on dose rate [5].

If mutual recombination were expected to be occur only when the distance between one interstitial and a vacancy is on the order of the 1st or 2nd nearest neighbor distance, the fraction of point defects annihilated by mutual recombination would be much smaller. Thus, there must exist some other mechanism of point defect recombination. One possibility may be that the recombination area is much larger, possibly the 5th or 6th nearest neighbor. Such a mechanism may require in-cascade gliding of small interstitial loops. However, further study is necessary to clarify such a possibility. The validation of such a mechanism of mutual recombination becomes more important at low temperature, because the fraction of point defects annihilated by mutual recombination is generally recognized as increasing with decreasing irradiation temperature.

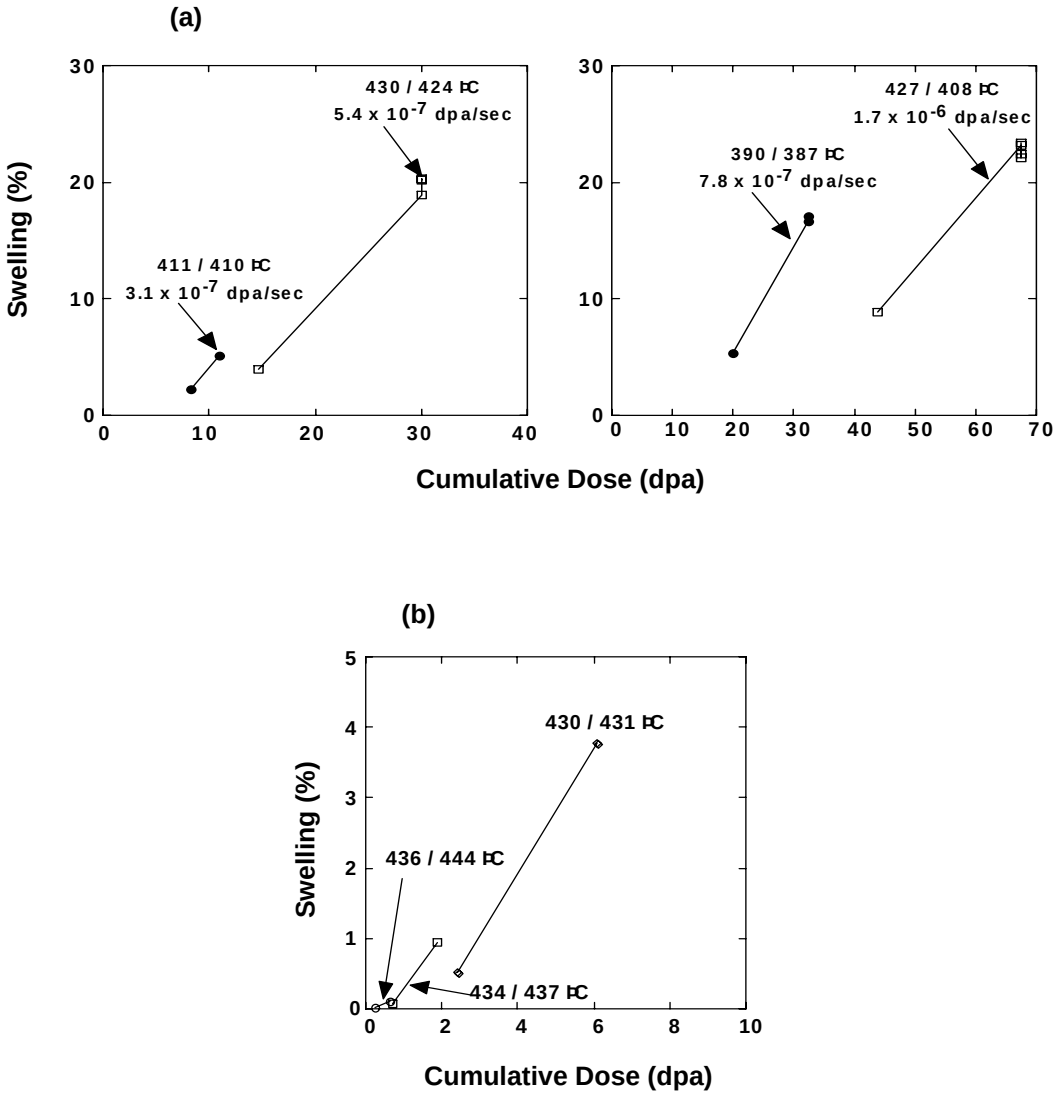

Figure 4. Comparisons of swelling as a function of cumulative dose. These figures show that dose rate differences affect swelling behavior more strongly than irradiation temperature.

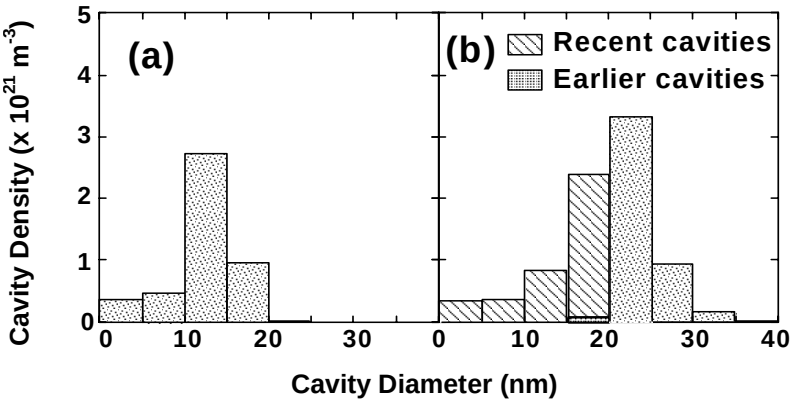

Figure 5. Dose Dependence of cavity size distribution at a fixed dose rate. Note that the density of "earlier cavities" is the same as that observed after 1 cycle irradiation, (a) 1 cycle irradiation to 2.36 dpa at 430°C, (b) 2 cycle irradiation to 6.36 dpa at 430/431°C.

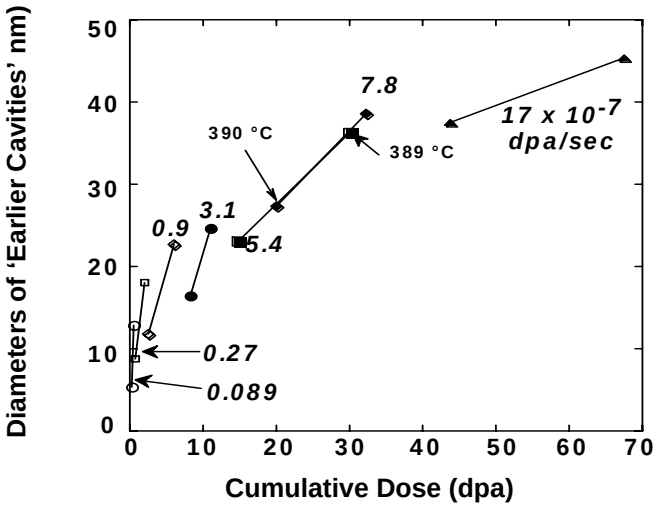

Figure 6. The diameters of "earlier cavities" as a function of cumulative dose.

At higher dose rates, point defects are generated at higher concentrations, resulting in a higher fraction of point defects annihilating by recombination. One would expect that the fraction of point defects escaping from recombination and being absorbed by sinks to be higher at lower dose rates. However, one would not expect recombination to be equally important throughout the range of dose rates studied. This apparent contradiction may arise from other significant effects of dose rate on microstructural evolution. First, enhanced loop growth with lower loop density is observed at lower dose rates [1-5,7,14], resulting in earlier loop unfaulting and an enhanced rate of network dislocation formation [5,7]. It was also shown that the incubation dose of swelling is strongly related to the dose required to form network dislocations [5,18-19].

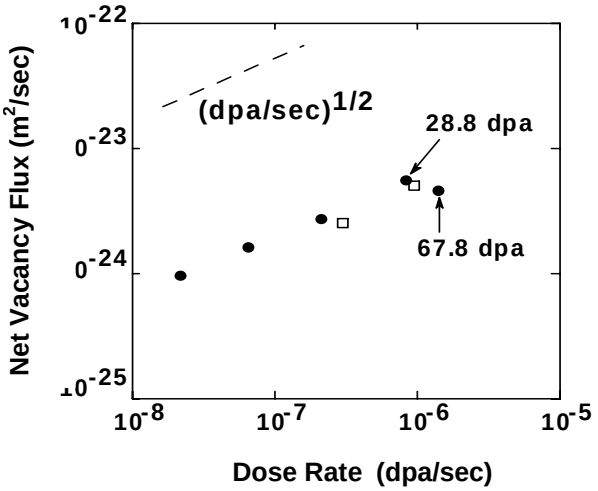

Figure 7. Dose rate dependence of the net vacancy flux. Circles show that dose rate dependence of specimens irradiated for 2 cycles is essentially the same as that of one cycle (squares). Note that below 30 dpa and 8.4 x 10^{-7} dpa/sec, the net vacancy flux is proportional to $(dpa/sec)^{1/2}$.

Summary

Several solution-annealed austenitic alloys were irradiated at ~400˚C over a wide range of dose rates, and the effect of dose rate on microstructural evolution was estimated for one alloy. Using an assumption about the cycle in which individual cavities nucleated, net vacancy flux calculated from the cavity growth rate was found to be proportional to $(dpa/sec)^{1/2}$ up to 30 dpa. This indicates that the fraction of point defects annihilated by mutual recombination is rather large. Thus, the primary origin of the dose rate effect on microstructural evolution at ~400˚C lies in the domination of point defect annihilation by recombination and the consequent influence on dislocation and cavity nucleation. In the development of models describing the results of long-term irradiation, it is essential to incorporate the mutual recombination mechanism into the model.

ACKNOWLEDGEMENTS

This work was supported by Monbusho, the Japanese Ministry of Education, Science and Culture under the FFTF-MOTA collaboration and the JUPITER program (Japan-USA Program for Irradiation Testing for Fusion Research), and the U.S. Department of Energy, Office of Fusion Energy, under Contract DE-AC06-76RLO 1830 at Pacific Northwest National Laboratory, and by the Lawrence Livermore National Laboratory under contract No W-7405-ENG-48 with the DOE. Additional financial support for T. Okita was provided by Nuclear Fuel Industries, Ltd. The authors are pleased to acknowledge the contributions of PNNL employees Ruby Ermi and Elaine Dieffenbacher for specimen retrieval and preparation.

REFERENCES

[1] T. Okita, T. Kamada and N. Sekimura, J. Nucl. Mater., 283-287 (2000) 220.

[2] T. Okita, N. Sekimura, T. Iwai and F. A. Garner, Proc. 10th International Symposium on Environmental Degradation of Materials in Nuclear Power Systems- Water Reactors, 2001, on CD with no page numbers.

[3] M. Kiritani: J. Nucl. Mater., 169 (1989) 89.

[4] T. Muroga, H. Watanabe and N. Yoshida, J. Nucl. Mater., 174 (1990) 282.

[5] T. Okita, N. Sekimura, F. A. Garner, L. R. Greenwood, W. G. Wolfer and Y. Isobe, Proc. 10th International Symposium on Environmental Degradation of Materials in Nuclear Power Systems-Water Reactors, 2001, on CD with no page numbers. Also published in Fusion Materials Semiannual Report for Period Ending June 30, 2001, pp. 148-164.

[6] A. Garner, M. L. Hamilton, D. L. Porter, T. R. Allen, T. Tsutsui, M. Nakajima, T. Kido, T. Ishii, G. M. Bond and B. H. Sencer, manuscript in preparation.

[7] T. Okita, T. Sato, N. Sekimura and F. A. Garner, Proc. PRICM-4 2001, in press.

[8] F. A. Garner, Material Science and Technology Vol.10A Nuclear Materials. 419.

[9] F. A. Garner, J. Nucl. Mater. 117 (1983) 177.

[10] N. Sekimura, K. Hamada and S. Ishino, J. Nucl. Mater., 179-181 (1991) 542.

[11] N. Sekimura and S. Ishino, ASTM-STP 1175, (1994) 992.

[12] L. K. Mansur, Nucl. Technol., 40 (1978) 5.

[13] Y. Katoh, A. Kohyama and R. E. Stoller, J. Nucl. Mater., 212-215 (1994) 179.

[14] R. E. Stoller and G. R. Odette, J. Nucl. Mater., 131 (1985) 118.

[15] L. K. Mansur and W. A. Coghlan, J. Nucl. Mater., 119 (1983) 1.

[16] H. Watanabe, A. Aoki, H. Murakami, T. Muroga and N. Yoshida , J. Nucl. Mater., 155-157 (1988) 815.

[17] M. Kiritani, N. Yoshida, H. Tanaka and Y. Maehara, J. Phys. Soc. Japan 39 (1975) 170.

[18] T. Muroga, F. A. Garner and S. Ohnuki, J. Nucl. Mater., 179-181 (1991) 546.

[19] T. Muroga, F. A. Garner, J. M. Mcarthy and N. Yoshida, ASTM-STP 1125, (1992) 1015.

STRESS AND TEMPERATURE DEPENDENCE OF IRRADIATION CREEP OF SELECTED FCC AND BCC STEELS AT LOW SWELLING – M. B. Toloczko and F. A. Garner (Pacific Northwest National Laboratory)

OBJECTIVE

The objective of this work was to show that a transition stress exists in FCC and BCC steels during irradiation creep and to map out this transition stress as a function of temperature and to propose possible creep deformation mechanisms taking place beyond the transition stress.

SUMMARY

A large amount of data on irradiation creep of face centered cubic (FCC) and body centered cubic (BCC) steels have been analyzed and published by the present authors, but a recent reanalysis of these data have provided further insight into irradiation creep behavior. The present paper looks at the stress and temperature dependence of creep at low swelling for selected 316 stainless steels and HT9 steels irradiated at temperatures from 400°C to 670°C. Analysis of the creep data has revealed that a transition from a lower creep rate with a stress exponent of one to a higher creep rate with an unknown stress exponent occurs in FCC and BCC steels at moderate stresses, and the transition stress is approximately the same for both classes of steels. Due to limited data at higher stresses, the nature of the creep behavior at stresses greater than the transition stress cannot be unambiguously defined. One possibility is that the stress exponent is transitioning from a value of one to a value greater than one. Another possibility is that the creep compliance value is transitioning to a higher value while the stress exponent remains at a value of one. The creep compliance coefficients of the FCC and BCC steels have also been carefully reanalyzed in the regime where the stresses are lower than the transition stress, and in this regime there is a clear delineation in the creep compliance values between 316 stainless steels, titanium-modified 316 steels, and HT9 steels as a function of temperature.

Introduction

In the present study, experimental data are reported which provide information on the irradiation creep phenomenon. It is understood that creep in an irradiation environment can be driven by a variety of mechanisms, and that like thermal creep, transitions in creep behavior may be observed in creep data as a function of applied stress. The present study uses a large body of creep data from a multi-year irradiation creep experiment that was performed in the Fast Flux Test Facility (FFTF) to define a temperature dependent transition stress. For stresses below this transition stress, there were sufficient data to determine the creep stress exponent and the creep compliance value, B_0, but there was insufficient data to define either the creep stress exponent or the creep compliance for stresses greater than the transition stress. It was observed that the transition stress was approximately the same for 316 SS, titanium-modified 316 SS, and HT9 steel. From the examination of the creep compliance values at stresses below the transition stress, it will be concluded that the creep compliance is sensitive to composition and perhaps crystal system. Much of the creep data analyzed in the present study have been previously reported in the open literature [1-3], but the data have not been compiled and analyzed to show the stress and temperature dependencies to be reported.

Experimental

Materials and Specimens

The materials for this study were 316 stainless steel (SS), titanium-modified 316 SS, and HT-9 which is a ferritic-martensitic stainless steel. The composition and the pre-irradiation thermomechanical treatment of the FCC steels are shown in Tables 1 and 2, respectively, while the composition and pre-irradiation

* Pacific Northwest National Laboratory (PNNL) is operated for the U.S. Department of Energy by Battelle Memorial Institute under contract DE-AC06-76RLO-1830.

thermomechanical treatment for the BCC steels are shown in Tables 3 and 4, respectively. Fabrication of the pressurized tubes from tube-stock is described in [4].

For each target irradiation temperature, a set of capped thin-walled tubes were fabricated with each tube having a different pressure. For the present work, a set of pressurized tubes shall be called a tube-set. The range of pressures, and thus stresses, was chosen based on the target irradiation temperature. In general, a tube-set consisted of between four and eight pressurized tubes with one tube have zero pressure at the irradiation temperature. The zero stress tube was used to estimate swelling.

The uncertainty in the magnitude of the stress in the tube-wall arises mainly from deviations in the actual test temperature (T_{test}) from the target test temperature (T_{target}). First order error analysis shows that the uncertainty in the stress is given approximately by

$$\frac{\Delta\sigma}{\sigma} \sim \frac{\left|T_{\text{test}} - T_{\text{target}}\right|}{T_{\text{target}}} \tag{1}$$

where the temperature is in Kelvin.

Stress and Strain Calculations

The stress state in the wall of a capped thin-wall pressurized tube is well known [4,5], and shall not be repeated here. The stress state is biaxial, and for purposes of comparison to other specimen geometries and stress states, the creep data are examined as a function of the von Mises effective stress ($\bar{\sigma}$. which for pressurized tubes is given by

$$\bar{\sigma} = \frac{\sqrt{3}}{2}\sigma_{\text{H}} \tag{2}$$

where σ_H is the hoop (tangential) stress.

Due to the 2:1 ratio of the hoop stress to the axial stress, and due to the fact that creep involves only deviatoric deformation, a plane strain deformation condition exists when a pressurized tube undergoes creep. The deviatoric deformation lies in the rθ plane, and there is no deviatoric deformation along the z-axis. Creep strains are obtained from the change in the outer-wall diameter of a tube. This measured outer-wall strain is converted into a mid-wall strain which is an average of the strain across the tube-wall thickness. For the tube geometries utilized in this experiment, the conversion factor is of the order of 1.1 and is essentially constant for outer-wall strains up to 10%. The mid-wall strain (ε_M) is then converted to an effective plastic strain [6]. Assuming plane strain deformation in the rθ plane, the effective plastic

Table 1. Composition of the FCC steels for the present study.

Alloy	Fe	Cr	Ni	Mo	Mn	V	Al	Cu	Co
Ti-Mod 316SS†	Bal	13.7	15.8	1.65	2.03	0.01	<0.01	<0.01	<0.01
316SS 1st Core	Bal	17.4	13.7	2.34	1.77	0.02	0.005	0.01	0.005
316SS 4th Core	Bal	17.7	13.7	2.82	1.53	0.01	0.01	0.02	0.01
Alloy	Si	C	Ti	Ta	S	P	B	N	O
Ti-Mod 316SS	0.80	0.039	0.34	<0.01	0.003	0.005	0.0005	0.004	---
316SS 1st Core	0.57	0.047	---	0.015	0.006	0.004	0.0005	0.004	0.002
316SS 4th Core	0.54	0.056	---	0.01	0.005	0.002	0.0005	0.002	0.002

† Ti-Mod 316 SS: D9 Heat 83508, 1st Core 316 SS: Heat 81600, 4th Core 316 SS: Heat 93591

Table 2. Pre-irradiation thermomechanical treatment of the FCC steels.

Alloy and Heat	Thermomechanical Treatment	Tube Dimensions (cm)
D9 Reference (Ti-Mod 316 SS)	20% cold-worked	0.584 outside diameter 0.038 wall thickness 2.82 length
D9-FV1 (Ti-Mod 316 SS)	10% cold-worked	0.457 outside diameter 0.020 wall thickness 2.24 length
D9-FV2 (Ti-Mod 316 SS)	20% cold-worked	0.457 outside diameter 0.020 wall thickness 2.24 length
316 SS 1st Core and 316 SS 4th Core	20% cold-worked	0.457 outside diameter 0.020 wall thickness 2.24 length

strain is given by

$$\bar{\varepsilon} = \frac{2}{\sqrt{3}} \varepsilon_{\mathrm{M}} \tag{3}$$

Because of the plane strain deformation and the conservation of volume which occurs during creep of a pressurized tube capsule, the pressure and wall thickness both decrease in such a way that the stresses in the tube wall remain nearly constant for strains as large as 10%.

Swelling was monitored by measuring the diametral strain of the stress-free tube that was included in each tube-set. As it is known that swelling is enhanced in materials under an applied stress [2, 7-11], the swelling estimates from the stress-free tubes were a lower bound estimate of the swelling that occurred in the pressurized tubes. For selected 316 SS pressurized tubes where stress-enhanced swelling was suspected to be large, these tubes were sacrificed at the conclusion of the irradiation experiment, and density measurements were performed to obtain swelling in the pressurized tubes [2]. The stress-enhanced swelling data were used in conjunction with the stress-free swelling values to obtain estimates of the true swelling rate in the pressurized tubes where stress-enhanced swelling was thought to be large.

Irradiation Conditions

Irradiations were performed at the Fast Flux Test Facility located in Richland, Washington using the Materials Open Test Assembly [12,13]. Target irradiation temperatures ranged from 400°C to 670°C. Specimen irradiation temperatures were achieved using an actively controlled gas-gap method which permitted temperature control to within ±5°C [13]. In most every instance, pressurized tubes in a tube-set

Table 3. Composition of the BCC steels.

Alloy	Fe	Cr	Ni	Mo	Mn	V	W
HT9-1†	Bal	11.8	0.51	1.03	0.50	0.33	0.52
HT9-2,3	Bal	11.8	0.57	0.94	0.54	0.24	0.52
HT9-5	Bal	11.8	0.60	1.06	0.62	0.33	0.52
Alloy	Si	C	Ti	Al	S	P	N
HT9-1	0.21	0.21	< 0.01	0.03	0.003	0.008	0.006
HT9-2,3	0.28	0.17	< 0.01	0.05	0.003	0.007	0.006
HT9-5	0.29	0.21	---	0.01	0.002	0.011	---

† HT9-1: Heat 84425; HT9-2,3: Heat 91353; HT9-5: Heat 92235

Table 4. Pre-irradiation thermomechanical treatment of the BCC steels.

Alloy	Thermomechanical Treatment	Tube Dimensions (cm)
HT9-1 and HT9-2	1038°C/5 min/air cool, 760°C/30 min/air cool	0.457 outside diameter 0.020 wall thickness 2.24 length
HT9-3	1100°C/2 min/air cool, 650°C/2 hr/air cool	0.457 outside diameter 0.020 wall thickness 2.24 length
HT9-5	1100°C/2 min/air cool, 650°C/2 hr/air cool	0.686 outside diameter 0.055 wall thickness 2.82 length

were placed side-by-side in the reactor to provide nearly identical irradiation conditions within a tube-set. However, a tube-set was not necessarily kept in the same position from one irradiation cycle to the next, which occasionally resulted in small temperature differences from one irradiation cycle to the next. Depending on the location in reactor and the particular MOTA cycle, the dose rate for this experiment ranged from ~0.8×10^{-6} dpa/sec to ~1.7×10^{-6} dpa/sec. Tubes were removed from reactor after each irradiation cycle, and diameter measurements were performed using a scanning laser profilometer [13]. Total accumulated dose ranged from about 50 dpa up to 165 dpa.

Creep Compliance Calculations

The creep compliance, B_0, is defined by the equation

$$\frac{\dot{\bar{\varepsilon}}}{\bar{\sigma}} = B_0 + D\dot{S} \tag{4}$$

where $\dot{\bar{\varepsilon}}$ is the effective strain rate per dpa, D is the creep-swelling coupling coefficient, and $\dot{S}$ is the volumetric swelling rate per dpa. B_0 represents the contribution to irradiation creep that is independent of swelling. For the present study, B_0 was calculated from the strains accumulated after the first irradiation cycle. For the HT9 and the Ti-modified 316 SS, no swelling was observed in the first irradiation cycle, and B_0 was easily calculated from Equation 4. However, for the 316 SS at several of the irradiation temperatures, swelling was observed during the first irradiation cycle. When swelling was present, it was necessary to solve for both B_0 and D which was done by applying Equation 4 to two irradiation intervals which provided the two equations needed to solve for the two unknowns, B_0 and D.

Results

Stress-Enhanced Swelling Measurements

316 SS is known to swell significantly at irradiation temperatures ranging from 550°C to 600°C, and thus it was necessary to measure both the stress-free swelling and the stress-enhancement of swelling so that the creep compliance could be accurately measured. Stress-enhanced swelling was measured on the 1st Core of 316 SS pressurized tubes irradiated at 550°C to about 80 dpa as previously reported [2]. The swelling in the pressurized tubes after 80 dpa along with the interpolated effect of stress on the swelling at lower doses is shown in Figure 1. The interpolated values for the swelling are represented by the equation

$$S = S_0(1 + F\bar{\sigma}) \tag{5}$$

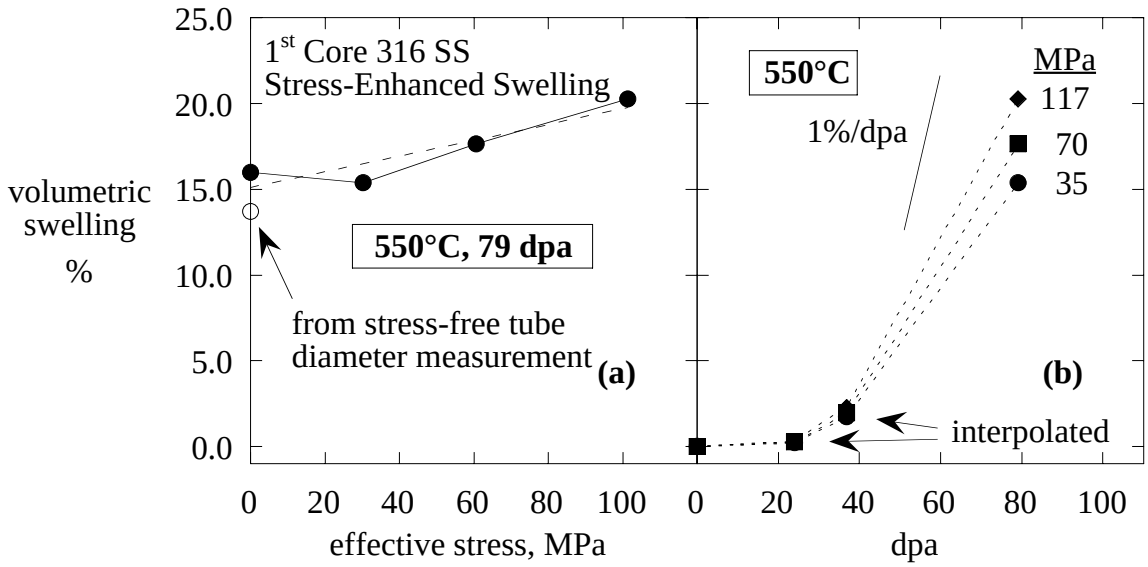

Figure 1. a) Stress-enhanced swelling of the 1st Core heat of 316 SS irradiated at 550°C, and b) the estimated interpolated behavior of the stress-enhanced swelling of the pressurized tubes at the lower doses.

where S_0 is the stress-free swelling, and F is a linear correlation factor. For the 316 SS, F was found to be 0.3×10^{-2} MPa^{-1} by fitting Equation 5 to the data in Figure 1a. As F will be used at temperatures other than at 550°C and only data on stress-enhanced swelling had been gathered at 550°C, the creep data in the open literature were surveyed to determine values for F at other temperatures. Creep data where F could be calculated were found for 316 SS and stabilized 316 SS irradiated at temperatures ranging from 455°C to 480°C, and the resulting F values are shown in Table 5. For swelling values greater than 1% where F could be clearly measured, F ranged from $0.3\text{-}0.9 \times 10^{-2}$ MPa^{-1}. It was decided to use a value for F of 0.5×10^{-2} MPa^{-1} which represents an average value over a greater range of temperatures.

Creep Data and Transition Stress

A vast amount of creep data were analyzed for the present study making it impractical to present all the creep data here, but a few representative plots showing creep strain as a function of applied stress are shown in Figures 2 and 3. The entire creep data set is published in Reference 14, and parts are published in References 1-3. The transition stress was taken at the data point on the creep versus stress curves where a large increase in slope occurred. Because there were only a limited number of data points on each curve, the chosen transition stress is a lower-bound estimate of the actual transition stress, and the actual transition stress may lie at some stress bounded by the chosen transition stress and the next higher stress level. Figure 3 shows an example where a transition in creep rate as a function of stress is clearly apparent. It was observed that the transition stress was temperature dependent, and the transition stress is plotted as a function of temperature in Figure 4. The data points connected by the dotted lines represent are the maximum applied stress at that temperature, while the data points connected by the solid lines represent the transition stress. There were two instances where the maximum applied stress may not have been high enough to reach the transition stress. The first is at 400°C where it can be seen that the maximum applied stress is 173 MPa, and all three of the alloy types showed no transition behavior up to this stress level. The other instance is at 600°C where the maximum applied stress of the HT9 alloy was only 15 MPa. Again, no transition in creep behavior was observed up to this stress, and the actual transition stress may have been greater than 15 MPa.

Table 5. Values for the stress-enhanced swelling coefficient calculated from data published in the open literature.

$S = S_o(1 + F\bar{\sigma})$			
reference	irradiation conditions	S_o, %	F, $x10^{-2}$ MPa^{-1}
7	annealed 316SS PT, 500°C	0.035	2.6
8	20% CW 316SS PT, 477°C	1.6	0.38
9	CW 316SS + Nb PT, 480°C	3.3	0.63
10	CW 316SS + Ti PT, 455°C	4.0	0.89
11	SA 316 type + Nb Pt, 480°C	20	0.30

Stress and Temperature Dependence of the Creep Stress Exponent

From plots of creep strain as a function of stress it was possible to determine the stress exponent for irradiation creep for stresses below the transition stress. For stresses above the transition stress, there were insufficient data to determine the creep stress exponent (or the creep compliance). For this study, creep strain as a function of stress was examined for the three alloy types at temperatures ranging from 400°C to 670°C which permits determining the stress exponent as a function of both stress and temperature. For stresses up to the transition stress, it was observed that the creep stress exponent had a value of one for each of the different alloy types.

Temperature Dependence of the Creep Compliance

The creep compliance coefficient of the alloys within the regime of stresses and temperatures where the stress exponent is equal to one is shown as a function of irradiation temperature in Figure 5a. As can be seen, there are clear differences in the creep compliance values for the three alloys with HT9 having the lowest creep compliance coefficient for temperatures between 400°C and 600°C. Shown in Figure 5b are creep compliance coefficient values obtained from creep data in the literature on similar materials [9, 15-26]. The values for the creep coefficients for the alloys in the literature are not so well stratified, but one similar trend is that with the exception of Malliard's data [22] which are unreasonably low for those

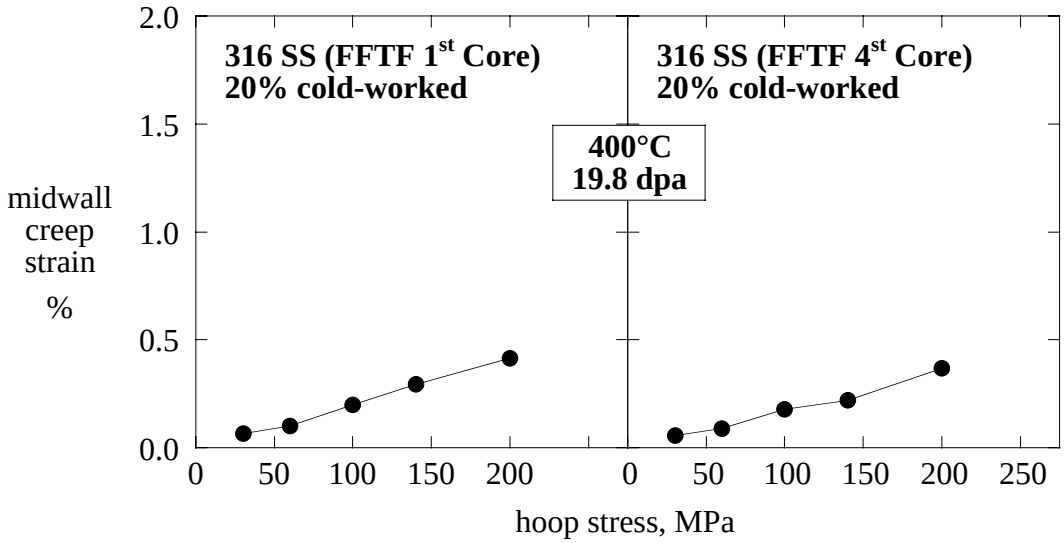

Figure 2. Midwall creep strain as a function of stress for two heats of 316 SS irradiated at 400°C.

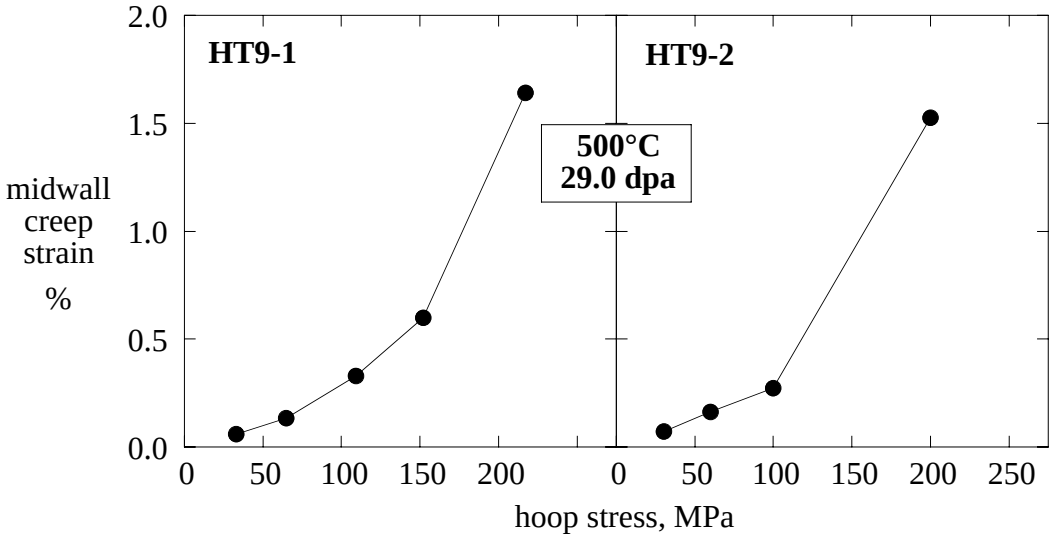

Figure 3. Midwall creep strain as a function of stress for two heats of HT9 irradiated at 500°C.

temperatures, the Ti-mod 316 SS alloys consistently have the highest creep compliance coefficient at the lower temperatures as does the Ti-mod 316 SS variants in the present study. The creep compliance values for the HT9 and 316 SS in the literature appear to be approximately the same.

Discussion

Transition Stress and Creep Mechanisms

A transition stress is typically representative of a change in creep mechanism. For the present study, a stress exponent of one at stresses below the transition stress indicates that a mechanism based on point defect diffusion is dominating irradiation creep. In the regime of temperatures where irradiation creep is known to be dominant (below 550°C in steels), current theories suggest that dislocation climb driven by point defect diffusion is the primary creep mechanism [27-30]. Because of the limited amount of data at stresses above the transition stress, it was not possible to determine whether the increase in creep as a function of stress was indicative of an increase in stress exponent or simply an increase in the creep compliance.

As a way to attempt to rationalize the creep mechanisms above and below the transition stress, the transition stress line for the irradiated 316 SS was overlayed on a thermal creep deformation map of 316 SS taken from the literature [31]. Ideally, the thermal creep deformation map would have been for a 316 SS with the same microstructural features that are typically present in 316 SS after irradation, but such materials and deformation maps are not available. Instead, the thermal creep deformation map was for annealed 316 SS. The thermal creep deformation map with the transition stress for the irradiated 316 SS is shown in Figure 6. This is not an ideal comparison because there are many differences in the microstructures of the two materials being compared. The annealed material will have a low dislocation density of about 10^8 cm^{-2}, it is free of precipitates, and it has a grain size of about 50 μm, whereas the irradiated material is likely to have a temperature dependent dislocation density ranging from 10^{11} cm^{-2} at 400°C to about 10^8 cm^{-2} at 670°C, it will have a large number of precipitates (also temperature dependent), and it will have a grain size closer to 15 μm. Because of the differences in microstructure, if the irradiated material was placed under stress in a thermal environment and a creep deformation map were constructed, the boundary between elastic behavior and power-law creep for this material would likely be shifted to higher stresses relative to the annealed material, and the diffusional flow regime (as

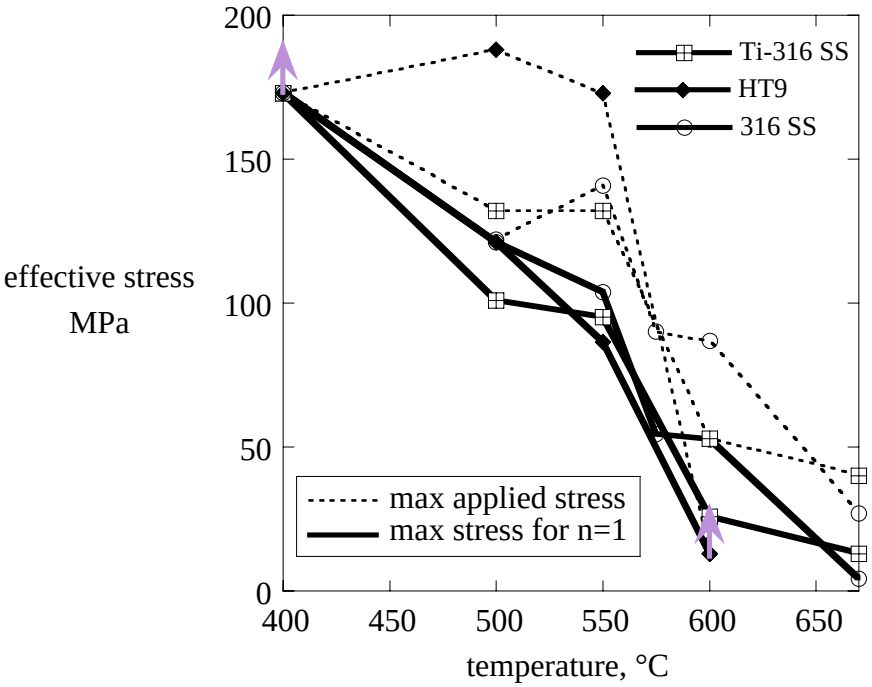

Figure 4. Transition stress as a function of temperature for the three alloy types. The data points associated with the solid lines represent the highest stress at which the creep rate was linearly proportional to the applied stress at the given temperature. The data points associated with the dotted lines represent the highest applied stress at the given temperature. The arrows indicate the transition stress was probably higher than the value shown because the maximum applied stress was not great enough to reach the transition stress.

defined in Figure 6) would be likely to have contributions by climb of dislocations at the lower temperatures. With this in mind, it is useful to compare the transition stress to the thermal creep behavior of the annealed material. Between 400°C and 550°C, the transition stress straddles the boundary between elastic behavior and power-law creep suggesting that at these temperatures, an irradiation-assisted climb-glide creep mechanism [31-35] may be beginning to play a dominant role in the total creep strains at stresses beyond the transition stress. This would lead to an increase in the creep stress exponent at stresses beyond the transition stress. At temperatures between 550°C and 670°C, it appears that diffusionally-controlled thermal creep mechanisms may be beginning to play a role in the total creep strains. In this scenario, thermal creep is likely to be driven by Coble creep mechanisms, and the creep stress exponent above the transition stress would remain at a value of one. While this discussion was based on trends in 316 SS, it is likely that similar phenomenon are occurring in the Ti-modified 316 SS and the HT9 variants.

Temperature Dependence of the Creep Compliance

The creep compliance values in Figure 5a show some unexpected trends. Because BCC steels are generally believed to have lower thermal creep resistance than FCC steels at high temperatures, it has been assumed that BCC steels would have lower creep resistance than FCC steels when irradiated at temperatures of 600°C and beyond. The data in Figure 5a, however, suggest that BCC steels may actually perform better in an elevated temperature irradiation environment than FCC steels. As discussed, it is likely that at temperatures of 550°C and beyond, thermal creep is likely to be playing a more and more dominant role. So it seems possible that the large increase in the creep compliance values for the 316 SS variants is due to thermal creep mechanisms, and it may be that for the relatively

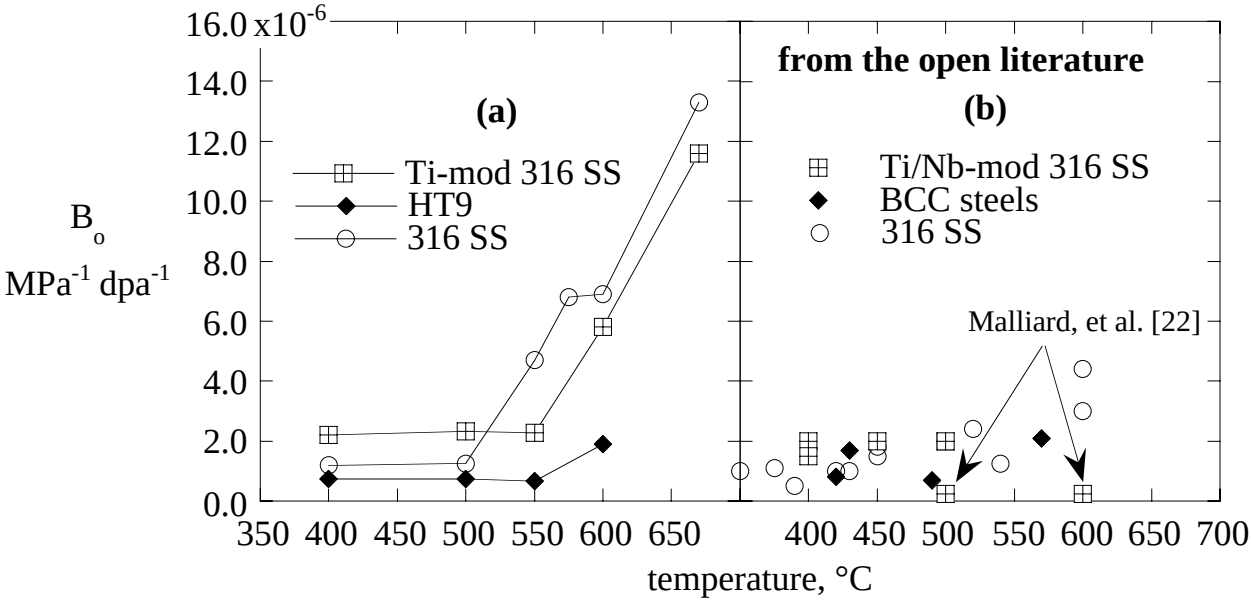

Figure 5. a) Average creep compliance of several different types of steel for stresses where the stress exponent is equal to one, and b) creep compliance values obtained from various studies published in the open literature [9,16-27].

low stresses where the creep compliance coefficient was measured, the HT9 steels may have better creep resistance than the 316 SS variants. Thermal creep at low stresses is thought to be due to vacancy diffusion between dislocations or along grain boundaries resulting in either climb of dislocations or movement of grain boundaries, respectively [36, 37], and in either case, the stress exponent would remain at a value of one which is consistent with the data. The reason for the improved creep resistance of HT9 over the 316 SS variants during irradiation is not obvious from the available data, however, it may be linked to the fact that HT9 is much more resistant than 316 SS to irradiation-induced changes in microstructure.

Summary and Conclusions

Irradiation creep of several different tube-sets of 316 SS, Ti-mod 316 SS, and HT9 were measured. From these measurements, it was possible to determine a transition stress that signals an increase in the creep rate as a function of stress for irradiation temperatures ranging from 400°C to 670°C. It was observed that all three of the alloy types had roughly the same transition stress as a function of temperature, and for stresses below the transition stress, the creep stress exponent has a value of one. From the available data, it appears that the transition stress at lower temperatures straddles the boundary between climb-controlled irradiation creep and irradiation-controlled climb-glide creep mechanisms, while at the higher temperatures, it straddles the boundary between dislocation climb-controlled irradiation creep and thermally-controlled diffusional creep mechanisms. When the creep compliance values for stresses below the transition stress (n = 1) were plotted as a function of temperature, it was found that between 400°C and 500°C, HT9 has the lowest creep compliance value while the Ti-mod 316 SS had the highest creep compliance value. Between 500°C and 550°C, the creep compliance values for the FCC steels began to increase strongly and continued increasing up to the highest temperature covered in the study The available data suggest this is due to the onset of thermally-controlled diffusional creep mechanisms The creep compliance values of the HT9 variants began to increase at 550°C, but the rate of increase was only a small fraction of the rate of increase of the FCC steels. This may be due to the fact that the

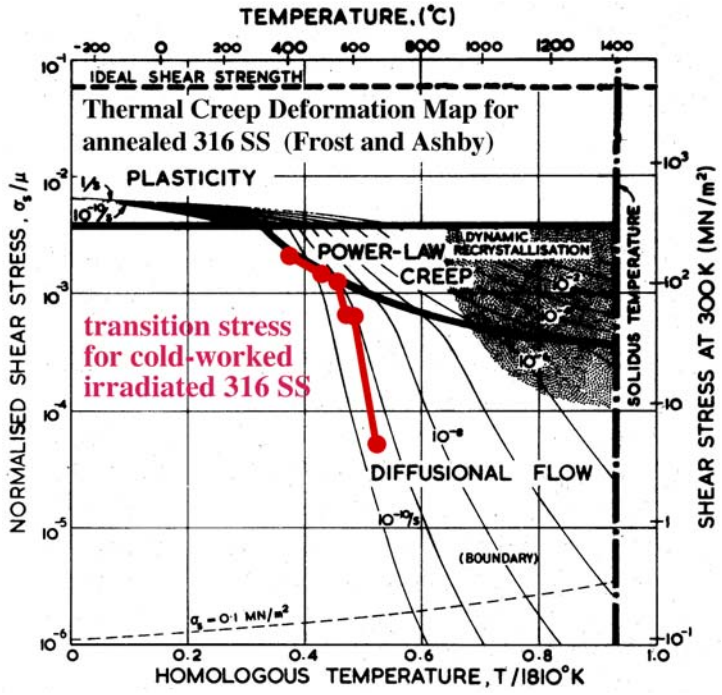

Figure 6. Creep deformation map of annealed 316 SS overlayed with the transition stress for 20% cold-worked irradiated 316 SS.

microstructure of BCC steels is more resistant to irradiation-induced microstructure changes than FCC steels.

REFERENCES

[1] F. A. Garner, M. L. Hamilton, C. R. Eiholzer, M. B. Toloczko, and A. S. Kumar, "Irradiation and thermal creep of a titanium-modified austenitic stainless steel and its dependence on cold work level", Journal of Nuclear Materials, Vols. 191-194, 1992, pp. 813-817.

[2] F. A. Garner, M. B. Toloczko, and R. J. Puigh, "The Relationship Between Swelling and Irradiation Creep in 20% Cold-Worked 316 Stainless Steel", Effects of Radiation on Materials, 19th International Symposium, ASTM STP 1366, M. L. Hamilton, A. S. Kumar, S. T. Rosinski, and M. L. Grossbeck, Eds., American Society for Testing and Materials, West Conshohocken, PA, 1999, pp. 667-678.

[3] M. B. Toloczko, and F. A. Garner, "Variability of Irradiation Creep and Swelling of HT9 Irradiated to High Neutron Fluences at 400-600°C", Effects of Irradiation on Materials: 18th International Symposium, ASTM STP 1325, R. K. Nanstad, M. L. Hamilton, F. A. Garner, and A. S. Kumar, Eds., American Society for Testing and Materials, West Conshohocken, PA, 1999, pp. 765-779.

[4] M. B. Toloczko, B. R. Grambau, F. A. Garner, and K. Abe, "Comparison of Thermal Creep and Irradiation Creep of HT9 Pressurized Tubes at Test Temperatures From ~490°C to 605°C", Effects of Radiation on Materials: 20th International Symposium, ASTM STP 1405, S. T. Rosinski, M L. Grossbeck, T. R. Allen, and A. S. Kumar, Eds., American Society for Testing and Materials, West Conshohocken, PA, 2001, pp. 557-569.

[5] S. P. Timoshenko, J. N. and Goodier, *Theory of Elasticity, Third Edition*, McGraw-Hill Book Company, 1970.

[6] L. E. Malvern, *Introduction to Mechanics of a Continuous Medium*, Prentice-Hall, Inc., New Jersey, 1969.

[7] J. F. Bates and E. R. Gilbert, "Experimental Evidence for Stress Enhanced Swelling", Journal of Nuclear Materials, Vol. 59, 1976, p. 95.

[8] J. F. Bates and E. R. Gilbert, "Effects of Stress on Swelling in 316 Stainless Steel", Journal of Nuclear Materials, Vol. 71, 1978, p. 286.

[9] W. Schneider, K. Herschbach, and K. Ehrlich, "Interdependence of In-Pile Creep and Void Swelling in Ti- and Nb-Stabilized Stainless Steels", ASTM STP 782, 1982, p. 30.

[10] J. L. Seran, H. Touron, A. Maillard, P. Dubuisson, J.P. Hugot, E. Le Boulbin, P. Blanchard, and M. Pelletier, "The Swelling Behavior of Titanium-Stabilized Austenitic Steels Used as Structural Materials of Fissile Subassemblies in Phénix", ASTM STP 1046, 1990, p. 739.

[11] A. N. Vorobjev, N. I. Budylkin, E. G. Mironova, S. I. Porollo, Yu. V. Konobeev, and F. A. Garner, "Irradiation Creep and Stress-Enhanced Swelling of Fe-16Cr-15Ni-Nb Austenitic Stainless Steel in BN-350", Journal of Nuclear Materials, Vols. 258-263, 1998, p. 1618.

[12] Irradiation Parameters for the FFTF Materials Open Test Assemblies from 1983 to 1992, WHC-SD-FF-TD-010 Revision 0, August, 1994.

[13] E. R. Gilbert, and B. A. Chin, “Irradiated Materials Measurement Technology,” *Effects of Radiation on Materials: Tenth Conference, ASTM STP 725*, David Kramer, H. R. Brager, J. S. Perrin, Eds., American Society for Testing and Materials, Philadelphia, 1981, pp. 665-679.

[14] M. B. Toloczko, “Irradiation Creep of Stainless Steels”, Ph.D. Thesis, Washington State University, Pullman, WA, December, 1999.

[15] E. R. Gilbert and J. F. Bates, "Dependence of Irradiation Creep on Temperature and Atom Displacements in 20% Cold-Worked Type 316 Stainless Steel", Journal of Nuclear Materials, Vol. 65, 1977, p. 204.

[16] J. L. Boutard, Y. Carteret, R. Cauvin, Y. Guerin, and A. Maillard, "Irradiation Creep of Solution Annealed and Cold-Worked 316 Stainless Steel", Proceedings of the Conference on Dimensional Stability and Mechanical Behaviour of Irradiated Metals and Alloys, Vol. 1, British Nuclear Energy Society, 1983.

[17] G. W. Lewthwaite and D. Mosedale, "The Creep of Solution Annealed, Austenitic Stainless Steels at about 500 K in the Dounreay Fast Reactor, (DFR)", Proceedings of the Conference on Dimensional Stability and Mechanical Behaviour of Irradiated Metals and Alloys, Vol. 1, British Nuclear Energy Society, 1983.

[18] K. Herschbach, W. Schneider, and H. J. Bergmann, "Swelling and In-Pile Creep Behavior of Some 15Cr15TiNi Stainless Steels in the Temperature Range 400 to 600°C", ASTM STP 1046, 1990, p. 570.

[19] D. L. Porter, G. D. Hudman, F. A. Garner, "Irradiation Creep and Swelling of Annealed Type 304L Stainless Steel at ~390°C and High Neutron Fluence", Journal of Nuclear Materials, Vols. 179-181, 1991, p. 581.

[20] J. L. Séran, V. Lévy, P. Dubuisson, D. Gilbon, A. Maillard, A. Fissolo, H. Touron, R. Cauvin, A. Chalony, and E. Le Boulbin, "Behavior under Neutron Irradiation of the 15-15Ti and EM10 Steels Used as Standard Materials of the Phénix Fuel Subassembly", ASTM STP 1125, 1992, pg. 1209.

[21] V. S. Neustroev and V. K. Shamardin, "Radiation Creep and Swelling of Austenitic 16Cr-15Ni-3Mo-Nb Steels Irradiated in the Reactor BOR-60 at 350 and 420 C", ASTM STP 1175, 1993, p. 816.

[22] A. Maillard, H. Touron, J. L. Séran, and A. Chalony, "Swelling and Irradiation Creep of Neutron-Irradiated 316Ti and 15-15Ti Steels", ASTM STP 1175, 1994, p. 824.

[23] M. L. Grossbeck, L. T. Gibson, and S. Jitsukawa, "Irradiation Creep in Austenitic and Ferritic Steels Irradiated in a Tailored Neutron Spectrum to Induce Fusion Reactor Levels of Helium", Journal of Nuclear Materials, Vols. 233-237, 1996, p. 148.

[24] I. Shibahara, S. Ukai, S. Onose, and S. Shikakura, "Irradiation Performance of Modified 316 Stainless Steel for Monju Fuel", Journal of Nuclear Materials, Vol. 204, 1993, p. 131.

[25] B. A. Chin, "An Analysis of the Creep Properties of a 12Cr-1Mo-W-V Steel", Proceedings of: Topical Conference on Ferritic Alloys for the use in Nuclear Energy Technologies, Snowbird, UT, 1983, p. 593.

[26] R. J. Puigh, "In-Reactor Creep of Selected Ferritic Alloys", ASTM STP 870, 1985, p. 7.

[27] P. T. Heald and M. V. Speight, "Steady-State Irradiation Creep", Philosophical Magazine, Vol. 29, 1974, p. 1075.

[28] W. G. Wolfer and M. Ashkin, "Diffusion of Vacancies and Interstitials to Edge Dislocations", Journal of Applied Physics, Vol. 47, No. 3, 1976, p. 791.

[29] F. R .N. Nabarro, R. Bullough, and J. R. Matthews, "The Enhancement of Creep by Irradiation", Acta Metallurgica, Vol. 30, 1982, p. 1761.

[30] C. H. Woo, "Shape Effect in the Drift Diffusion of Point Defects into Straight Dislocations", Physical Review B, Vol. 30, No. 6, 1984, p. 3084.

[31] H. J. Frost and M. F. Ashby, “Deformation-Mechanism Maps, The Plasticity and Creep of Metals and Ceramics” 1st Edition, Pergamon Press Inc, 1982.

[32] J. Weertman, "Dislocation Climb Theory of Steady State Creep", Transactions of the American Society for Metals, Vol. 61, 1968, p. 681.

[33] S. D. Harkness, J. A. Tesk, and C.-Y. Li, "An Analysis of Fast Neutron Effects on Void Formation and Creep in Metals", Nuclear Applications and Technology, Vol. 9, 1970, p. 24.

[34] L. K. Mansur, "Irradiation Creep by Climb-Enabled Glide of Dislocations Resulting from Preferred Absorption of Point Defects", Philosophical Magazine A, Vol. 39, No. 4, 1979, p. 497.

[35] J. H. Gittus, R. G. Anderson, and M. J. Makin, "On the Possibility that Cottrell Creep occurs when Non-Fissile Materials such as Stainless Steel Irradiated in a Fast Reactor", Proceedings of the conference on Irradiation Embrittlement and Creep in Fuel Cladding and Core Components, British Nuclear Energy Society, 1972, pg. 291.

[36] W. J. Duffin and F. A. Nichols, "The Effect of irradiation on Diffusion-Controlled Creep Processes", Journal of Nuclear Materials, Vol. 45, 1972/73, p. 302.

[37] F. Garofalo, "Fundamentals of Creep and Creep-Rupture in Metals", The MacMillian Company, New York, 1965.

[38] J. P. Hirth and J. Lothe, "Theory of Dislocations", 2nd Edition, Wiley and Sons, Inc., 1982.

7.0 MHD INSULATORS, INSULATING CERAMICS AND OPTICAL MATERIALS

PROPOSED SPECIFICATIONS FOR CANDIDATE INSULATOR MATERIALS FOR MHD COATINGS -- B. A. Pint and J. R. DiStefano (Oak Ridge National Laboratory)

OBJECTIVE

The objective of these specifications is to identify experimental criteria necessary to (1) select new candidate materials for electrically-insulating, magneto-hydrodynamic (MHD) coating development and (2) evaluate coatings based on processing technique, electrical resistivity, liquid metal compatibility, thermal cycling resistance and self-healing capability. The first section details the recommended performance criteria for evaluation of bulk specimens and the second section details coating performance requirements that need to be met in order to proceed to dynamic loop testing of a coating.

SUMMARY

These specifications provide metrics for evaluating compatibility results in static Li exposures to determine when bulk ceramic candidate materials are ready for coating development and when coatings are ready for dynamic (i.e. loop) testing.

INTRODUCTION

The blanket system in proposed deuterium/tritium-fueled fusion reactors converts the fusion energy into heat and breeds tritium for the fuel cycle. One promising blanket concept is the use of liquid lithium as the breeding medium, where the lithium also self-cools the blanket. However, in magnetic fusion energy systems where a strong magnetic field is used to contain the fusion plasma, a MHD pressure drop is developed when the electrically conductive lithium flows across the magnetic field lines. Accordingly, an insulating barrier is needed to decouple the lithium from the magnetic field in order to have adequate liquid metal flow at acceptable pumping power levels. The best way to achieve such isolation is by creation of an electrically insulating surface layer on the structural alloy containing the lithium. From heat-transfer considerations, this barrier must be relatively thin (<10μm) and integrally bonded to the first-wall containment material, which would likely be a vanadium alloy. The barrier or coating also must be resistant to radiation damage and, based on efficiency considerations, it must be compatible with the lithium and first wall at temperatures up to 700°-750°C.[1]

The materials development goal is to find an insulator material that can be made into a coating with the necessary integrity, compatibility and resistivity to satisfy the system requirements. In order to circumvent the need to select and/or develop a coating process for each new candidate material, one strategy has been to test bulk ceramics to identify the best potential candidates before proceeding with coating development. This allows a wider range of materials to be considered without the cost and time required for an optimized coating fabrication procedure to be completed. The first set of specifications is to clarify when a new candidate material should proceed to coating development and testing, and the second set is to determine when a coating is ready for liquid metal loop experiments. Ultimately, dynamic loop testing will be necessary to determine if a coating is likely to successfully perform in a fusion reactor.

Note: the optimum coating thickness and maximum system operating temperature are not included but MUST be specified before the selection criteria can be satisfied. At this time, those values would be estimated as 10μm and 700°C but could change based on design consideration.

MATERIALS SELECTION SPECIFICATIONS

For any new materials under consideration, the following basic material requirements should be met before coating development of the material occurs:

1-1. Appropriate resistivity measured at 400°-800°C
$\geq 10^5$ Ω-cm

1-2. Appropriate compatibility with liquid lithium:

A. expose a bulk specimen or coating of the pure material to liquid lithium (>90at%Li) at a temperature 50K above the specified maximum temperature.

Note: To eliminate microstructural variables, particularly second phases on grain boundaries that may not be present in a coating, it may be preferable to expose a single crystal of the material.

B. after exposure to lithium as described in (A), based on mass change and/or microstructural analysis, the specimen should show:

- less than an equivalent 3μm loss in specimen thickness after 100h
- less than an equivalent 5μm loss in specimen thickness after 1000h
- less than a 5μm deep reaction zone after 1000h
- the combined thickness loss and reaction zone should not exceed 5μm after 1000h

Note: a reaction zone would include new compound formation, intergranular penetration or intercalation of the material with lithium.

For example, for a specified maximum temperature of 650°C and a bulk specimen of AlN, the testing would be conducted at 700°C. A mass loss of ≈1.6 mg/cm^2 would correspond to an equivalent 5μm material loss using a density of 3.25g/cm^3. Figure 1 shows data obtained for AlN

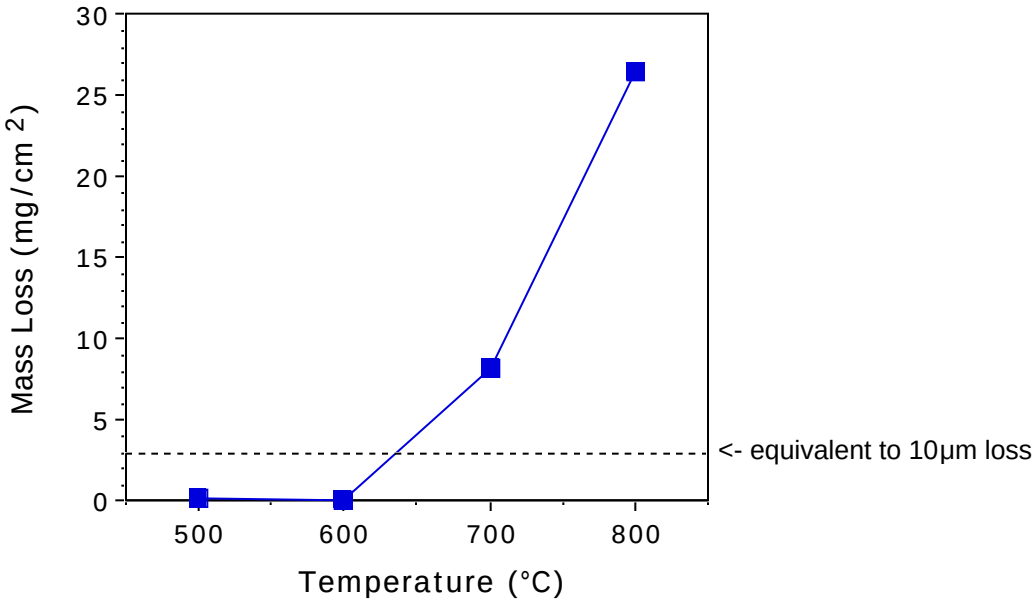

Figure 1. Mass losses for AlN (Shapal SH-50 from Tokuyama Corp, 0.04wt%Y, 0.9%O) after 1000h exposures in undoped Li at each temperature in a V alloy capsule. The dissolution of AlN becomes rapid above 600°C. [2]

exposed to undoped Li in a V alloy capsule for 1000h at several test temperatures. According to the above criteria, these data would indicate a maximum use temperature for AlN in undoped Li of <650°C. (These results are provided as an example, mass losses were lower at 700°C when a Mo capsule was used for the test.)

COATING PERFORMANCE CRITERION

For an actual coating, these criteria would need to be satisfied before proceeding with a dynamic lithium loop testing.

2-1. Demonstrate a reasonable and reproducible coating technique for this application:

A. uniform microstructure and coating thickness (deviations less than 25% of total thickness) confirmed by multiple characterization techniques including transmission electron microscopy as appropriate.

B. ability to coat complex geometries

2-2. Demonstrate sufficient electrical resistivity from 25°C to specified maximum temperature:

A. measure values of ≥1000 Ω-cm^2 on a coating with appropriate thickness (50%-150% of specified thickness) and fabricated using a process which satisfies requirements in section 2-1.

Note: the resistance should be measured through the coating thickness, NOT by a 4-pt probe method which measures properties in the plane of the coating.

2-3. Demonstrate compatibility with liquid lithium:

A. expose coating with appropriate thickness (50%-150% of specified thickness) and fabricated using a process which satisfies requirements in section 2-1 to liquid lithium (>90at%Li) at a temperature 50K above the specified maximum temperature.

B. after exposure to lithium as described in (A), based on mass change and/or microstructural analysis, the coating specimen should show:

- less than 5% loss in coating thickness after 100h
- less than 10vol% of coating reacted after 100h
- less than 10% loss in coating thickness after 1000h
- less than 20vol% of coating reacted after 1000h
- resistivity measured from 400° to test temperature maintained above 500 Ω-cm^2

For example, using specifications of 700°C and 10μm, a 5-15μm thick coating would be exposed at 750°C and thickness losses of <0.5μm after 100h or <1μm after 1000h would be required.

Note: percentage thickness losses were selected based on a minimum reactor operating time of 25,000h; significant mass losses measured in short-term static tests are unlikely to significantly decrease in longer-term dynamic exposures.

Note: compound conversion limitations are specified because the coating may not dissolve but rather convert to a different compound such as has been reported for AlN forming $LiAlO_2$ [3] or Y_2O_3 forming $LiYO_2$ [4]

2-4. Demonstrate thermal cycling capability

A. use a coating with appropriate thickness (50%-150% of specified thickness) and fabricated using a process which satisfies requirements in section 2-1

B. expose the coating to a minimum of 3 thermal cycles from room temperature to a temperature 50K above the specified maximum temperature in liquid lithium (>90at%Li). Each cycle should consist of 10-100h at the high temperature and >0.5h at room temperature.

C. after exposure described in (B), examine to determine that the coating meets the requirements in section 2-3-B.

2-5. Demonstrate possibility of self healing

A. experimentally confirm the viability and reproducibility of the self healing process and specify the conditions under which the self-healing will be performed.

Note: for a coating system which demonstrates exceptional Li compatibility, adhesion and resistance to thermal cycling, this requirement may be waived.

REFERENCES

1. D. L. Smith, M. C. Billone, S. Majumdar, R. F. Mattas and D.-K. Sze, J. Nucl. Mater. 258-63 (1998) 65-73.
2. B. A. Pint, L.D. Chitwood, J. H. DeVan and J. R. DiStefano, DOE/ER-0313/29 (2001) 3.
3. B. A. Pint, L.D. Chitwood, J. H. DeVan and J. R. DiStefano, DOE/ER-0313/28 (2000) 26.
4. T. Mitsuyama, T. Terai, T. Yoneoka and S. Tanaka, Fusion Eng. and Design, 39-40 (1998) 811-817.

Preliminary Investigation on the Deposition of Y-O and Si-O Films on V-4%Cr-4%Ti for the In-situ Forming of CaO Coatings * J.-H. Park, A. Sawada, B. J. Kestel, D. L. Rink, K. Natesan, and R. F. Mattas[1], Energy Technology Division and [1]Technology Development Division, Argonne National Laboratory, Argonne, IL 60439 USA

OBJECTIVE

According to our previous study we have demonstrated the in-situ CaO insulator coating forming, generating defects under the thermal cycling condition, and self-healing of defects on V-Cr-Ti alloys in liquid lithium system, [1] and sintered Y_2O_3 is compatible with liquid Li.[2] This encouraging results caused us to investigate O-charged V-4Cr-4Ti with a Y film deposited by means of PVD. We are now investigating the in-situ forming of a CaO layer on a surface V-4Cr-4Ti enriched with Y-O or Si-O. In the study of insulator coatings on the V/Li blanket, the electrical insulation behavior should be maximized to have a thinner film that high toughness and thermal conduction. What need to be eliminated or minimized is V incorporation into the insulator film and in-situ self-healing. The addition of Si was objected to minimize the V incorporation in the in-situ forming film.

SUMMARY

We have investigated two ways to modify the V-4Cr-4Ti surfaces (Y deposition and Cr-Si-O addition) in preparation for forming CaO coatings on V alloys in liquid Ca-Li. Our earlier experimental studies indicated that sintered Y_2O_3 is compatible with liquid Li. In continuing studies, we have deposited thin (0.2, 0.8, and 1.5 μm) yttrium films on V-4Cr-4Ti substrates by physical vapor deposition (PVD). Annealing the thin Y-metallic PVD film on O-charged V-4Cr-4Ti at 750°C for 17 h formed an oxide film by the solid-state reaction between O and Y. Both energy dispersive spectroscopy (EDS) and X-ray diffraction indicated that the 0.2 and 0.8 μm Y-metallic films converted to either YVO_3 or $Y_8V_2O_{17}$ after annealing, but the thicker (1.5 μm) Y-metallic film developed two phases as $Y_8V_2O_{17}$ and Y_2O_3. When these samples were exposed in 2.8 at.% Ca-Li at temperatures of 700°C for 99 h, a uniform-microstructure CaO layer was formed on the top of the Y-V oxides, but localized Y was not detected by cross-sectional EDS analysis. However, the thicker films were shown to have a localized spallation problem between V-4Cr-4Ti and the oxide after annealing, so we ceased the exposure tests. The Si-O addition was performed by $Cr+Cr_2O_3$ equilibrium inside a vacuum-sealed quartz (SiO_2) chamber at 950°C for 17 h followed by exposure to 2.8 at.% Ca-Li at temperatures of 700°C for 99 h. This yielded an adhesive, water insoluble, and highly resistive Ca-Si-O film.

INTRODUCTION

Also investigated was Cr-Si-O addition based on a thermodynamic evaluation. The addition of Si was objected to minimize the V incorporation in the in-situ forming film. Our previous investigations showed that the incorporation of V into the in-situ-formed CaO was normally 15 to 35 at.%. If V is highly incorporated, the film could be conductive due to the V having a wide range of ionic. Based on the thermodynamic evaluation, additions of Si could form as Ca-Si-O in the Ca-Li environment. Therefore, we performed surface modification by $Cr+Cr_2O_3$ equilibrium inside a vacuum-sealed quartz (SiO_2) chamber. When the oxygen partial pressure (pO_2) is low, such as the level corresponding to $Cr+Cr_2O_3$ equilibrium at high temperatures, the quartz becomes the source of Si, Si-O, and Cr that are incorporated into the V-4Cr-4Ti along with O in the chemical vapor.

Based on these concerns, we initiated study of the Y and Si additions to the in-situ CaO films, and we are reporting the results of short exposures and expect continuation of testing.

* Work supported by the U.S. Department of Energy, Office of Fusion Energy Research, under Contract W–31–109–Eng–38.

EXPERIMENTAL PROCEDURE

PVD Y-film deposit: We O-charged a conventional argon-oxygen gas, and yttrium metal was evaporated by use of a tungsten-heating element within an ultra-high-vacuum chamber to deposit films with thicknesses of between 0.2 to 1.5 µm. Samples were annealed at 750°C for 13 h in the vacuum. The Y film reacted with the pre-charged O in the V-4Cr-4Ti to convert to Y-O. The films were analyzed by scanning electron microscopy, EDS, and investigated the microstructures by SEM and chemical analysis by EDS, and X-ray diffraction.

V-4Cr-4Ti annealing in the Cr+Cr_2O_3: We have performed the simultaneous additions of Si and O by means of Cr+Cr_2O_3 equilibrium inside the vacuum-sealed quartz (SiO_2) chamber at 950°C for 17 h. The above samples were exposed to 2.8 at.% Ca-Li at 600-700°C for between 99 and 747.5 h. Experimental details can be found in our previous reports.[3]

Y_2O_3 ceramic: For comparison, we exposed a rectangular sample of sintered Y_2O_3 ceramic in 2.8 at.% Ca-Li at 600°C for 623 h.

RESULTS AND DISCUSSIONS

Sintered Y_2O_3 ceramic: The sintered Y_2O_3 samples exposed to 2.8 at.% Ca-Li at 600°C for 623 h were intact except for surface darkening. The measured geometry remained the same before and after the exposure. This result was similar to our previous test in pure liquid Li at 425°C for 240 h.

Investigation on Y-coated V-4Cr-4Ti: Figure 1shows the stepwise X-ray diffraction studies for each process: Spectra are given for the Y-deposit, sample annealed at 750°C, and sample after exposure at 700°C in 2.8 at.% Ca-Li for 99 h. The x-ray spectrum for the exposure in the 2.8 at.% Ca-Li was identical with that for the samples exposed without Y deposit. Since the CaO film was formed and grew in-situ it was expected that those film structures might be identical. The CaO film in Y-O coated samples was thicker than without the coating. Table 1 presents film thickness for the in-situ coatings deposited on V-4Cr-4Ti in 2.8 at. % Ca-Li exposure for 99 h at 700°C for the Y-coated (t = 0.5 µm) samples. The film chemical analysis done by EDS is shown in Fig. 2.

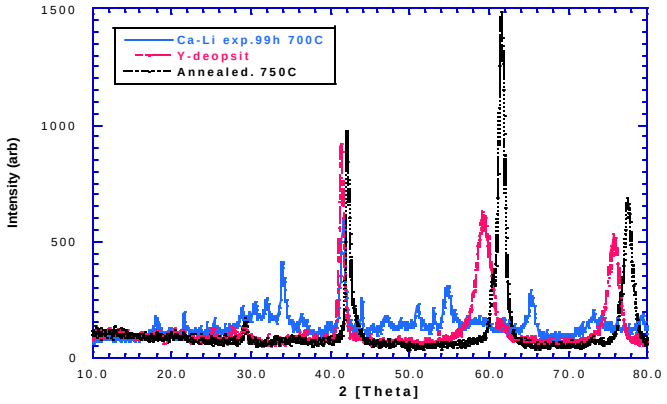

Fig. 1.

X-ray diffraction for sample #33 (Table 1). Pattern for Y-deposit, after annealing at 750°C, and after exposure at 700°C in 2.8 at. % Ca-Li for 99 h.

Table 1. Thickness of the in-situ coating deposited on V-4Cr-4Ti in 2.8 at. % Ca-Li exposure for 99 h at 700°C for the Y-coated (t = 0.5 µm) samples.

Sample No.	O (wppm)	Y deposit (µm)	XRD, annealed @750°C 13 h	Film t (µm) SEM	Note
33	400	0.2	$Y_8V_2O_{17}$	11.8	Film thicker in Y-O coated samples.
47	7000	0.35	YVO_3	9.5	
48	6600	0.35	-	10.0	
79	400	none	-	4.3	

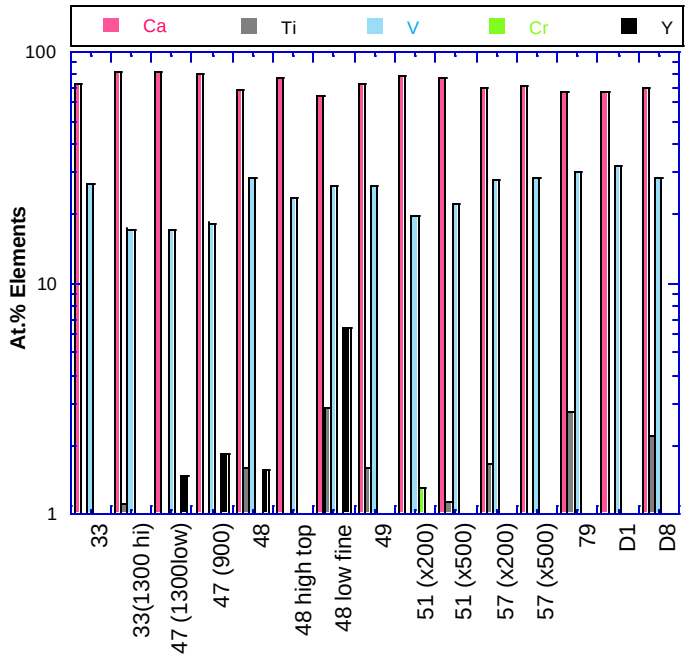

Fig. 2.

Elemental composition of the in-situ film formed on V-4Cr-4Ti in 2.8 at. % Ca-Li exposure for 99 h at 700°C for the Y-coated samples. Parentheses indicate that the SEM magnification for the EDS analysis and hi = thicker area and low = thinner coating area (for the #79, D1, and D8 samples, not Y-coated samples)

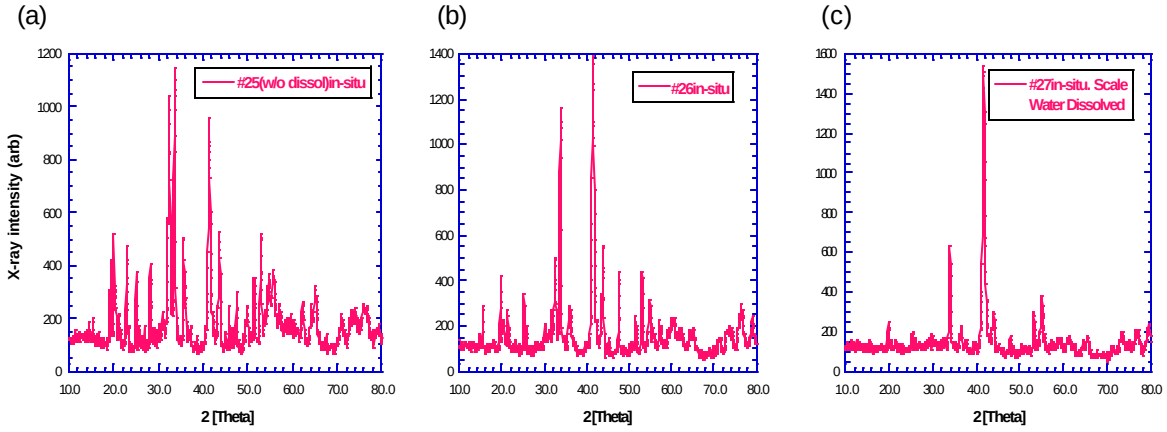

Fig. 3. X-ray diffraction for the in-situ formed scales on the V-4Cr-4Ti in the 2.8 at. % Ca-Li at 600°C for 747.5 h. O-charging done by $Cr+Cr_2O_3$ pack inside the vacuum-sealed quartz cell. (a) Without dissolution of the excessive Ca-Li residue on the sample surface (#25). The Ca-Li residue was minimized during removal of sample from the molten Ca-Li. (b) With dissolution in the ethanol (#26). (c) With dissolution in water, i.e. water insoluble layer (#27). (See Table 2.)

Si-Cr-O annealed V-4Cr-4Ti*:* Figure 3 shows the X-ray diffraction patterns for the in-situ formed films on the V-4Cr-4Ti in the 2.8 at. % Ca-Li at 600°C for 747.5 h. Shown are the patterns for the three distinct layers between the V-4Cr-4Ti and film: water insoluble layer, ethanol insoluble layer, and soluble layer. For the x-ray investigations the major spectrums are identical, but detailed analysis of the X-ray peaks still remains.

Table 2. Results of the EDS analysis for the sample surface from the in-situ coating performed on V-4Cr-4Ti in 2.8at.% Ca-Li exposure at 600C for 747.5 h for the samples annealed with Cr+Cr_2O_3 in a quartz cell. Beam energy (BE) = 10 keV otherwise noted otherwise.

No.	[a]O (Wppm)	Cal'd t (μm)	Meas'd t (μm)	Fraction of the element by EDS (at. fraction)					Note
				Ca	V	Ti	Cr	Si	
25	[4895]	-	-	0.513	0.462	0.0198	0.000	0.005	BE= 30 keV
26	[1838]	12.077	-	0.710	0.241	0.0018	0.000	0.047	
27	[12374]	11.154	-	0.476	0.163	0.0129	0.000	**0.348**	[b]**Water insoluble film**
28	[14691]	-	26.30	0.699	0.277	0.0000	0.000	0.024	
29				0.677	0.298	0.0000	0.000	0.025	
35	[1431]	5.5385	-	0.681	0.283	0.0155	0.000	0.020	
45				0.701	0.267	0.0017	0.000	0.031	
46				0.689	0.289	0.0067	0.000	0.015	BE = 40 keV

[a] Brackets indicate total wt. changed during the quartz sealing cell in test with the Cr/Cr_2O_3 atmosphere. Some Si and Cr may be affected. Real O-wppm should be lower than those in Brackets. This in-situ formed film was highly adhesive and high insulation based on our experience with in-situ formed films in Ca-Li environments. Currently, we do not have the electrical resistivity data required for the blanket design. Therefore, we plan to continue the study on the in-situ formed Ca-Si-O film on V-4Cr-4Ti.

Since we have found the adhesive with the V-4Cr-4Ti to be water insoluble and highly resistive (only checked at ambient temperature) for sample #27 (Table 2), we have calculated the free energy of formation for the Ca-Si-O shown in Fig. 4. As we see in Fig. 4, the Si incorporation in the in-situ formed Ca-Si-O film of #26 sample might effective as a buffer layer between CaO and V-4Cr-4Ti. In this film, V is 16 at.% (lowest) and Ca + Si = 83 at. % (highest) those are our targeted goal for the in-situ insulator coatings in Ca-Li environments.

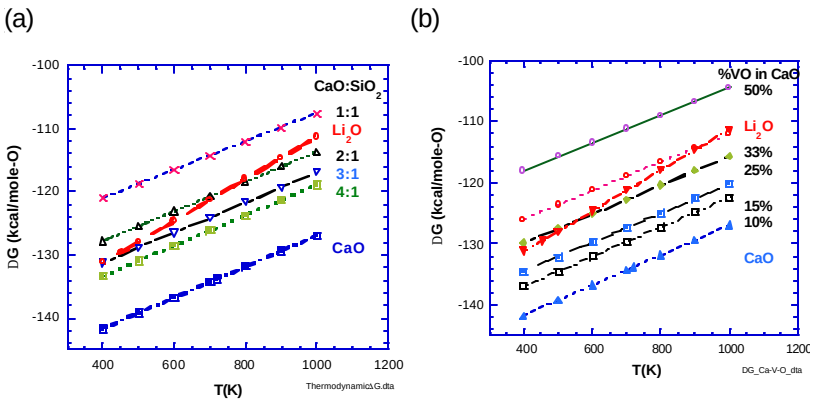

Fig. 4.

Gibbs free energy, ?G for the formation of ternary oxides per mole of O.
(a) Ca-Si-O with various ratios of CaO and SiO_2 and, (b) Ca-V-O. See water insoluble in-situ formed Ca-Si(V)-O (#27). (See Fig. 3 and Table 2.)

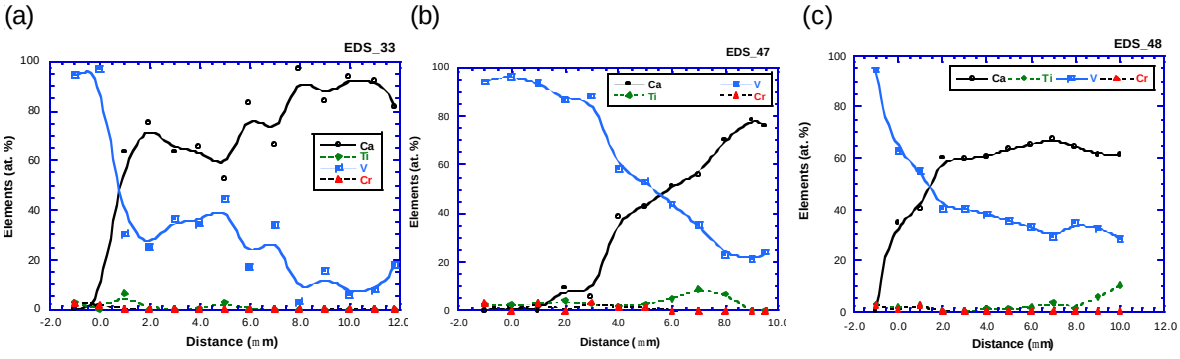

Fig. 5. Cross-section EDS analysis near the interface of V-4Cr-4Ti and film. Samples were exposed in 2.8 at.% Ca-Li at 700ºC for 99 h, and the excessive Ca-Li was dissolved in methanol for 20 h. Sample numbers are noted in the right top corner of the each figure. Sample description is given Table 1.

FUTURE SUGGESTED WORK

Our previous studies were limited to short (t = 100 h) exposures of Ca-Li at T = 700°C. Currently, the 700°C exposure for a longer time (t =1000 h) is the challenge. Y was intact based on our previous liquid metal-compatibility test, but Y collects hydrogen that penetrates through the metal wall from environmental moisture into the liquid metal to form the thermodynamically stable cubic yttrium hydride (YH_2) from the hexagonal cross-packed-Y. Therefore, for the deposition of Y-metallic film on the O-charged V-4Cr-4Ti, followed by exposure of the in-situ formed Y-Ca-O layer in the Ca-Li environment at 700°C, it is expected that the Y_2O_3 layer is intact. When a micro-crack is generated, however, the Ca and O will behave as self-healing defects. In this case, O in the micro-cracked zone reacts with Ca for the formation and dissolution; these processes will continue until the amount of O in the V-4Cr-4Ti is completely consumed. At 700°C rates for the forming and dissolution of film are high, so it is necessary to slow down or block the outward diffusion of (V and) O through the film layer after the film forms. This approach is similar to the reactive element effect in the high-temperature oxidation of metals obtained by the addition(s) of proper cations into the in-situ forming films beyond the yttrium oxide films. We expect that Si could be the best choice due to its stable thermodynamic nature in liquid-Li when it forms Ca-Si-O, as shown in Fig. 4.

ACKNOWLEDGMENTS

P. Johnson and B. Tani of Argonne Analytical Chemistry Laboratory provided the X-ray diffraction studies. Work supported by the U.S. Department of Energy, Office of Fusion Science, under Contract W–31–109–Eng–38.

REFERENCES

1 J. -H. Park and T. F. Kassner, CaO Insulator Coatings and Self-healing of Defects on V-Cr-Ti Alloys in Liquid Lithium System, J. Nucl. Mater. 233-237, 476-481 (1996).

2 J. -H. Park, M. R. Fox, and G. Dragel, DOE/ER-0313/13, 260-275, and 290-294 (1992).

3 J. -H. Park, A. Sawada, K. Natesan, D. Rink, and R. F. Mattas, Progress of In-situ Coatings on the V-4Cr-4Ti in 2.8 at. % Ca-Li at 600 & 700ºC, Fusion Materials Semiannual Report Vol. #32 (2002).

Progress on Development of In-situ Coatings for V-4Cr-4Ti[*] J.-H. Park, A. Sawada, D. L. Rink, K. Natesan, and R. F. Mattas[1], Energy Technology Division and [1]Technology Development Division, Argonne National Laboratory, Argonne, IL 60439 USA

OBJECTIVE

Corrosion resistance of structural materials and magnetohydrodynamic (MHD) forces and their influence on thermal hydraulics and corrosion are major concerns in the design of liquid-metal blankets for magnetic fusion reactors (MFR).[1] The objective of this study is to develop in situ coatings at the liquid-metal/structural-material interface,[2] with emphasis on coatings that can be converted to an electrically insulating film to prevent adverse currents that are generated by MHD forces from passing through the structural walls.

SUMMARY

We are investigating the in-situ formation of CaO coatings on V-4Cr-4Ti structural material in liquid lithium under various conditions. Initially, the near surface of the V-4Cr-4Ti was oxygen-charged at 710°C and homogenized at 750°C for 17 h, then samples were exposed in 2.8 at.% Ca-Li at temperatures of 600 and 700°C for times between 50 and 747.5 h. The thickness of the in-situ-formed CaO was 4 to 26 μm under the experimental conditions. In the 50 h exposure, thicker CaO films were formed at higher oxygen contents and 700°C, while thinner CaO films were formed at lower oxygen contents and 600°C. For longer exposures at 600°C (623 and 747.5 h), the film thickness stayed the same, but for 700°C exposures (100-425 h) the CaO film chemistry changed, with the film becoming thinner as a result of the net effect from compensating for the film formation and dissolution. We measured the electrical resistivity in an inert-gas environment at between room temperature and 760°C for in-situ formed films at 600°C in 2.8 at.% Ca-Li for 623 and 747.5 h. The measured values for the electrical resistivity were shown to satisfy the design requirement for insulating coatings in the Li/V advanced blanket for the magnetic fusion reactor (MFR). We also performed a Ca-Li compatibility test for single-crystal CaO samples at 600°C for 623 h. The surface of the single-crystal CaO was dissolved 50 μm. These results indicate that the in-situ formed film could be a different phase from the pure CaO. As a result of our recent investigations, we may have met the important development issues for obtaining 700°C stable coatings in Li/V advanced MFR blankets.

INTRODUCTION

Current research on magnetic fusion reactors includes development of electrically insulating coatings for the V alloy in first wall/blanket applications. In this present study, we have focused on in-situ CaO film fabrication at 600 and 700°C in 2.8 at.% Ca-Li on the V-4Cr-4Ti of either US heat or National Institute of Fusion Science (NIFS) heats. Single-crystal CaO samples were also subjected to the compatibility test in the 2.8 at. % Ca-Li to compare with the in-situ formed CaO films.

EXPERIMENTAL DETAILS

Samples preparation is documented in our several previous reports.[2,3] Samples of V-4Cr-4Ti were O-charged at 700°C and O-homogenized in a vacuum-sealed (quartz) cell for 17 h at 750°C. Several samples were then arrayed together, and dipped into a Ca-Li pot at 600 and 700°C for 50-747.5 h. Each desired exposure times, the sample tree was raised above the liquid-Ca-Li level and then shaken to minimize residual Ca-Li around the samples. The excessive Ca-Li around the samples was dissolved in methanol to investigate the surface and cross section by scanning electron microscopy (SEM) and X-ray diffraction (XRD). Ex-situ electrical conductivity measurements were performed for the samples exposed

[*] Work supported by the U.S. Department of Energy, Office of Fusion Energy Research, under Contract W–31–109–Eng–38.

in 2.8 at.% Ca-Li after the residual Ca-Li had been removed in ethanol. Details are found in our previous report.[2,3] Two platinum discs were used as electrodes in the top and bottom positions. The electrical conductivity measurements were performed in 99.996% Ar at 25 = T = 760°C using a high-input impedance Keithley Model 2001 multi-meter. To determine the CaO compatibility in 2.8 at.% Ca-Li, rectangular shapes of single-crystal CaO samples were also exposed at 600°C for 623 h.

RESULTS

In-situ formed films: Overall results for the coating performance at 600 and 700°C with different times of the in-situ coatings are summarized in Table 1.

Thickness of the film: The coating thicknesses on V-4Cr-4Ti in 2.8 at. % Ca-Li exposures at 600°C for 623 and 747.5 h are listed in Tables 2 and 3. Table 4 gives thicknesses for the 700°C exposure for 99 h. Thicknesses of the films were measured by the cross-section SEM view or calculated by the weight change, assuming that the film was CaO (density of 3.25 g/cm^3). Figure 1 shows the calculated thickness vs. O contents for the in-situ formed CaO film using the various weight. changes after exposure in the 2.8 at.% Ca-Li at 600°C for 623 h listed in Table 3. The CaO thickness was calculated from the amount of oxygen in the V-4Cr-4Ti being reacted with Ca in the 2.8 at.% Ca-Li, and was also determined from the weight change after the exposure at 600°C for 623 h. These values indicated that thinner films were formed than expected. This means that O is escaping from the process, or the in-situ formed CaO films are dissolved during the exposed period. From this trend, we can predict the dissolution rate, as given in Table 3.

Adhesion of the film: No physical data for the adhesion were obtained, but according to our experiences, longer exposures (compare with our previous exposures t = 120 h) should increase the film integrity.

Vickers hardness (VH) profiles: Figures 2 and 3 show the cross-sectional VH profiles for the V-4Cr-4Ti samples exposed to 2.8 at.% Ca-Li at 700ºC for 99 h and 600ºC for 747 h, respectively. These trends indicate that lower O in the V-4Cr-4Ti results in greater VH near the surface. This effect may be the result of the Ca incorporation into the alloy substrate at 700ºC.

X-ray diffraction: For the stepwise dissolution in methanol and in water, three distinctive layers exist between the V-4Cr-4Ti and film: water insoluble layer, ethanol insoluble layer, and soluble layer. For the x-ray investigations, most major spectra are identical for the films formed in 2.8 at.% Ca-Li at 600°C, but detailed analysis on the X-ray spectra remains to be done.

Electrical resistance: Figures 4 and 5 show the measured electrical resistance times area of the in-situ formed CaO films in an inert gas atmosphere. Some measurements were also performed in air at temperatures between room temperature and 750ºC. These measurements were made at a high input impedance of 10^{12} ohm with the Keithly 2001 multi-meter. In general, resistance times area (R*A) values satisfied the MFR design requirement. but when it exposed in air, much lower R*A values were measured (#45 sample) however, in the MFR design purposes, the air exposure may not be a consideration.

Chemical compositions for the CaO films: Surface and cross-sectional films were investigated by EDS analysis. The cross sectional EDS results are presented in Fig. 6.

Single-crystal CaO exposure: A CaO single crystal was dissolved 53 µm *in 2.8 at. % Ca-Li for 623h at 600°C, and the dissolution rate was* determined by the difference geometry before and after exposure. If we assume the dissolution to occur at a linear rate, it can be expressed as R_d (CaO single crystal) = 8.51 x10^{-2} µm/h. This value is 10 to 15 times higher than that of in-situ formed films. However, the film dissolution rate increases with increasing O contents in the V-4Cr-4Ti (Table 3). For exposure times of 623 and 725 h at 600°C, the in-situ formed CaO layers and the CaO crystal are different from each other.

Table 1. Performance of the in-situ formed CaO coating on V-4Cr-4Ti in 0.0, 0.5, and 2.8 at.% Ca-Li at 600 and 700°C.

T (°C)	Time (h)	Films[a]	Remark	Note .
600	120[b]	Good insulator	Film thickness almost same for t =120 h. Film stop growing when O consumed in the V-4Cr-4Ti substrate.	**2.8 at.% Ca-Li:**
	623			
	747.5			
700	50	Good insulator	Rough surface microstructure.	
	99	Good insulator	Smoother surface than 50 h exposure.	Acceptable for 600°C, but not acceptable for 700°C time exposure 425 h.
	425	Conductive	Film showed lower Ca & higher Ti compare with the film formed at lower T and shorter time.	
	(1000)	(Conductive)	Did not pursue because the 425 h exposure became conductive with low surface Ca fraction.	
	100 (100 + 100)	Conductive	Film dissolved: 100 h exposed in 2.8at.%Ca-Li at 600°C for in-situ coating procedure, and then transferred to the pure Li pot for the 100 h exposure.	**Pure Li:** Not acceptable
	500 (100 + 500)	Conductive	Film dissolved: 100 h exposed in 2.8 at. % Ca-Li at 600°C for in-situ coating with the condition of all consumed O in the alloy substrate, then transferred to the 0.5 at. % Ca-Li pot for the 500 h exposure.	**0.5 at.% Ca-Li:**
	(1000)	(Conductive)	500 h exposure showed conductive with dissolved film so it is not desired to pursuit, but to learn the surface microstructure and chemistry, it is under running.	Not acceptable

[a] "Good insulator" indicates satisfaction of the requirement resistance times area value in the MFR application.
[b] For V-5Cr-5Ti.

Table 2. Thickness for the in-situ coating depositeded on V-4Cr-4Ti in 2.8 at. % Ca-Li for 747.5 h at 600°C.

No.	O-charging method	[a]O (Wppm)	Calcul'd film thickness (μm)	Meas'd film thickness (μm)
25	Cr/Cr_2O_3	[4895]	-	-
26	Cr/Cr_2O_3	[1838]	12.1	-
27	Cr/Cr_2O_3	[12374]	11.1	-
28	Cr/Cr_2O_3	[14691]	-	26.3
29	-	[400]	-	11.4
35	Cr/Cr_2O_3	[1431]	5.5	-
45	Ar(O)	4858	4.9	-
46	Ar(O)	6400	-	25.0

Note: [a] Brackets indicate that O-Wppm, including total wt. changed during the quartz sealing cell in the Cr/Cr_2O_3 equilibrium. Some portion of the weights to be affected by the addition of Si and Cr; therefore, real O-wppm should be lower than those in brackets.

Table 3. Raw data for sample treatment for the exposure in 2.8 at.% Ca-Li at 600ºC for 623 h (NIFS-II heat).

	Units	NIFS-II Heat Samples			
		2-D3	3-D3	7-D3	6-D5
As-received (AR) sample weigtht = W_i	(g)	1.1655	1.2482	1.122	1.1465
Surface area of sample	(cm^2)	4.745	5.039	4.590	4.677
Sample wt. after O-charged	(g)	1.1690	1.2522	1.1280	1.1533
Sample wt. O-homogenized, Wo	(g)	1.1691	1.2524	1.1278	1.1534
W(O) = [150 Wppm (AR) + Wo]	(Wppm)	3750	4350	5950	7050
	(mg/cm^2)	0.9211	1.0775	1.4544	1.7280
Thickness, film calculated by W(O) , t(O)	(μm)	9.92	11.60	15.66	18.61
Post exposure in 2.8 at.% Ca-Li = W_f	(g)	1.1785	1.2615	1.1392	1.1663
W(I) = $W_f - W_i$ = Wt. of CaO	(mg/cm^2)	2.7397	2.6393	3.7470	4.2331
Thickness calculated from W(I), t(CaO)	(μm)	8.43	8.12	11.53	13.03
W(II) = $W_f - W_O$ = Wt. of Ca	(g)	1.9810	1.8059	2.4835	2.7580
Thickness calculated from W(II), t(Ca)	(μm)	8.53	7.78	10.70	11.88
Film dissolution rate, R_d = [t(O)-t(CaO)]/623 h	(μm/h)	[2.39×10^{-3}]	5.56×10^{-3}	6.62×10^{-3}	8.96×10^{-3}
Chemical composition EDS analysis (film surface)	at.% Ca	85.0	77.35	80.60	82.03
	at.% Ti	0.08	0.000	0.000	0.000
	at.% V	14.84	22.65	19.40	17.97
	at.% Cr	0.000	0.000	0.000	0.000

Table 4. Thickness for the in-situ coating on V-4Cr-4Ti in 2.8 at. % Ca-Li exposure for 99 h at 700°C.

No.	O (Wppm)	Y-coated	Thickness Measured (μm)	Heat
79	as rec'd	no	4.3	US
D-1	2000	no	6.1	NISF
D-8	6000	no	8.5	NIFS

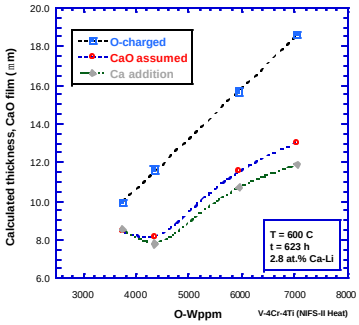

Fig. 1. Calculated thickness vs. O-content for the in-situ formed CaO film using the various weight change after exposure in 2.8 at. % Ca-Li at 600°C for 623 h. (See Table 3.)

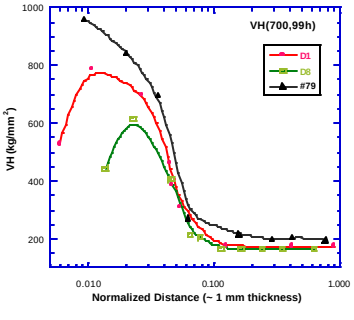

Fig. 2. Vickers hardness across the V-4Cr-4Ti exposed in 2.8 at.% Ca-Li at 700°C for 99 h with the D1, D8, and #79 samples.

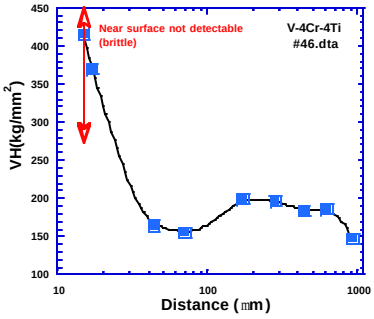

Fig. 3. Vickers hardness (VH) across the V-4Cr-4Ti (#46) exposed in 2.8 at. % Ca-Li at 600°C for 747.5 h. Near surface was very brittle.

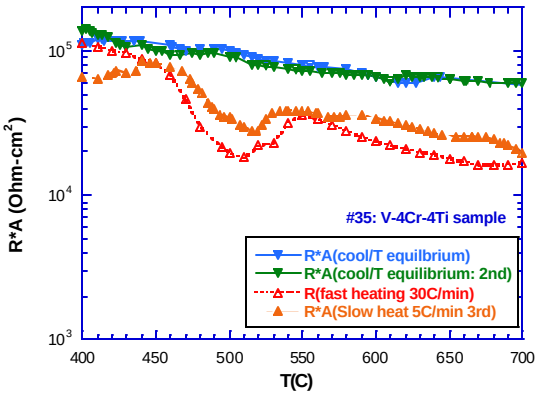

Fig. 4. Electrical resistance times area vs. temperature in an inert atmosphere for the film formed on the V-4Cr-4Ti (#35) after exposure in the 2.8 at. % Ca-Li at 600°C for 747.5 h.

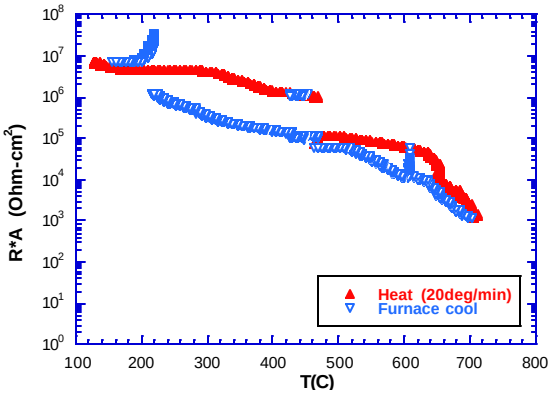

Fig. 5. Electrical resistance times area for the in-situ coated V-4Cr-4Ti in 2.8 at. % Ca-Li for 623 h (#7D3) (NIFS-II heat). For the heat cycled performance from heating and then cooling.

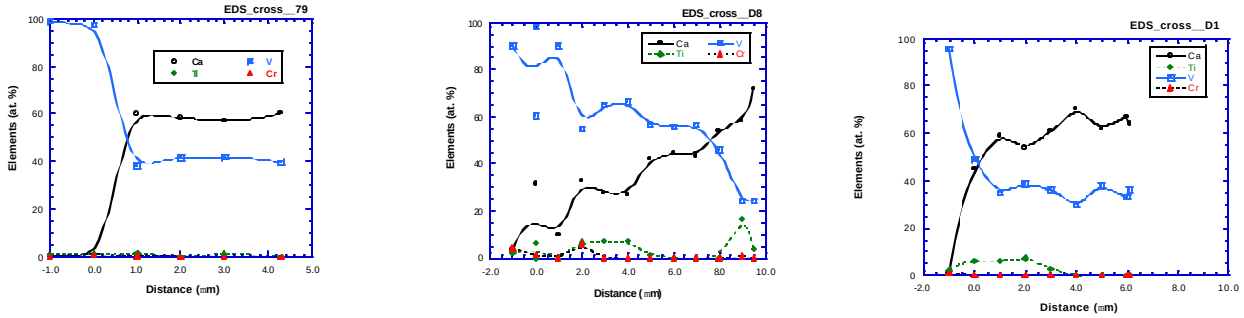

Fig. 6.
Cross-section EDS analysis near the interface of V-4Cr-4Ti/film. Samples were exposed in 2.8 at.% Ca-Li at 700ºC for 99 h, and the excessive Ca-Li dissolved in methanol for 20 h. Sample numbers are noted in the right top corner of each figure. Sample description is in Table 4.

Table 4. Thickness for the in-situ coating on V-4Cr-4Ti in 2.8 at. % Ca-Li exposure for 99 h at 700°C.

No.	O (Wppm)	Y-coated	Thickness Measured (μm)	Heat
79	as rec'd	no	4.3	US
D-1	2000	no	6.1	NISF
D-8	6000	no	8.5	NIFS

ACKNOWLEDGMENTS

P. Johnson and B. Tani of Argonne Analytical Chemistry Laboratory provided the X-ray diffraction.

REFERENCES

1. C. C. Backer et al., Tokamak Power Systems Studies FY 1985, Argonne National Laboratory Report ANL/FPP-85-2 (Dec. 1985).

2. J.-H. Park and T. F. Kassner, CaO insulator coatings and self-healing of defects on V-Cr-Ti alloys in liquid lithium system, J. Nucl. Mater. 233-237 476-481 (1996).

3. J.-H. Park, K. Natesan, and D. L. Smith, Fusion Materials Semiannual Report Vol. #31(2001).

STUDY OF THE LONG-TERM STABILITY OF MHD COATINGS FOR FUSION REACTOR APPLICATIONS -- B. A. Pint and L. D. Chitwood (Oak Ridge National Laboratory)

OBJECTIVE

The objective of this task is to assess the long-term, high-temperature compatibility of high electrical resistance coatings with lithium at high temperatures. Electrically insulating coatings on the first wall of magnetic confinement reactors are essential to reduce the magnetohydrodynamic (MHD) force that would otherwise inhibit the flow of the lithium coolant. Initial experimental work was conducted on bulk ceramics to determine basic lithium compatibility and maximum-use temperatures of candidate ceramics such as AlN and Y_2O_3. As the next step, coatings of Y_2O_3 are now being evaluated.

SUMMARY

Coatings of Y_2O_3 (12.5μm thick) were formed on V-4Cr-4Ti substrates using electron-beam assisted, physical vapor deposition (EB-PVD). The resistivity of the as-received, 12.5μm thick coatings was lower than literature values for bulk Y_2O_3, possibly due to cracks or pores in the coating. Coated substrates were exposed to Li in vanadium alloy capsules at 700° and 800°C for up to 1000h. One specimen was exposed to Li for three sequential 100h thermal cycles at 800°C and was cooled to room temperature between cycles. All of the exposed specimens were largely intact after exposure although x-ray diffraction indicated some reaction with the Li. The resistivity of several exposed coatings was measured to 500°C. The specimen exposed for 3, 100h cycles at 800°C showed no drop in resistivity after exposure while the specimen exposed for 1000h at 800°C showed a lower resistivity.

PROGRESS AND STATUS

Introduction

Previous work[1,2] where the Li compatibility of bulk ceramics was examined in capsule tests suggested that Y_2O_3 was an attractive MHD coating candidate. Polycrystalline Y_2O_3 specimens showed little mass change after 1000h exposures in Li at 700° and 800°C. Also, its resistivity at 700°C was sufficient for the MHD coating application.[3] Therefore, Y_2O_3 coatings were fabricated to examine their performance before and after exposure to Li.

Experimental Procedure

Current work focused on Y_2O_3 coatings made by EB-PVD at Lawrence Livermore National Laboratory by A. Jankowski and J. Hayes. Ten 12.5mm diameter x 1mm thick V-4Cr-4Ti substrates polished to a 1μm finish were coated with Y_2O_3 in two batches by rastering an electron beam over a pressed powder Y_2O_3 target. Using laser profilometry, the thickness of the as-received coatings was determined to be 12.5μm. The experimental procedure for lithium exposures has been outlined elsewhere.[4,5] Coated specimens were exposed for 100h and 1000h at 700° and 800°C. To check the adhesion of the coating in thermal cycling, one specimen was heated to 800°C for 100h and cooled to room temperature three times before the capsule was

opened and the specimen removed. Specimen dimensions and mass were measured before and after exposure (0.01mg/cm^2 accuracy). After exposure to Li, the first specimen was distilled in vacuum at 500-550°C to remove residual Li from the specimen. (The same procedure was used to clean the bulk specimens.) However, the V-4Cr-4Ti substrate oxidized due to a leak in the vacuum system. To avoid this problem, subsequent specimens were cleaned by submerging them in methanol for 24h at room temperature. Before and after exposure, the coated specimens were characterized using field emission gun, scanning electron microscopy (SEM), auger electron spectroscopy (AES) and x-ray diffraction (XRD) with 300kV Cu Kα radiation. The resistance was measured by sputtering a gold electrode (5.1mm diameter) and surrounding guard ring to limit current leakage on the surface of the coating. The specimen was then heated to 500°C in a vacuum system with a pressure of ≈10^{-6} Torr to limit oxidation of the V-4Cr-4Ti substrate. Voltages of 5-30V were applied with a Hewlett-Packard voltage source and current was measured as a function of temperature using a Keithley picoammeter.

Results and Discussion

As-received coating specimens were characterized using SEM and XRD. Figure 1 shows the as-received surface morphology which is typical of the EB-PVD process and indicates the coating grain size is <0.5µm. Figure 2a shows the coating's diffraction spectra from the coating which was a near perfect match with the Y_2O_3 standard (JCPDS card #41-1105). The resistivity of one coated specimen as a function of temperature is shown in Figure 3. It was significantly less than that reported for bulk Y_2O_3.[3] Two additional Y_2O_3 specimens were coated with an electrode to check the resistivity of the as-received coating. In both cases, a short circuit was measured suggesting that Au had infiltrated the coating and that cracks or pores in the as-received EB-PVD coating may have reduced its measured resistivity.

Three coatings have been exposed at 800°C for times of 100h, 3x100h and 1000h. The coating exposed for 1000h at 800°C showed a mass gain of 1.5mg but since an uncoated V-4Cr-4Ti

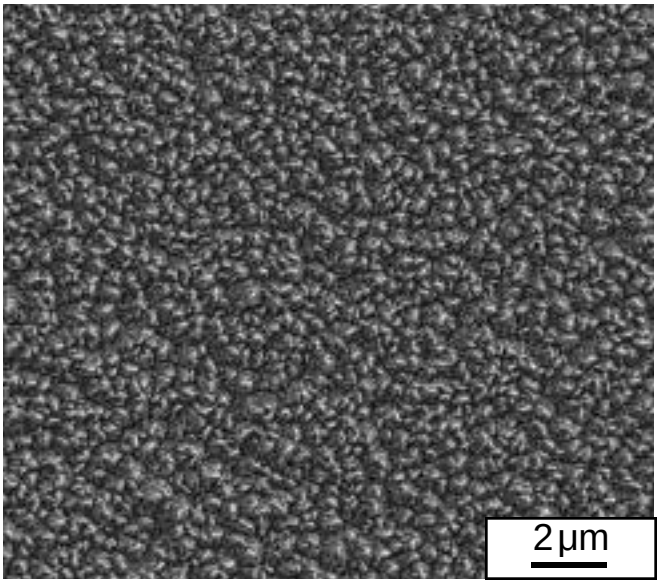

Figure 1. SEM secondary electron plan-view image of the as-received EB-PVD Y_2O_3 coating.

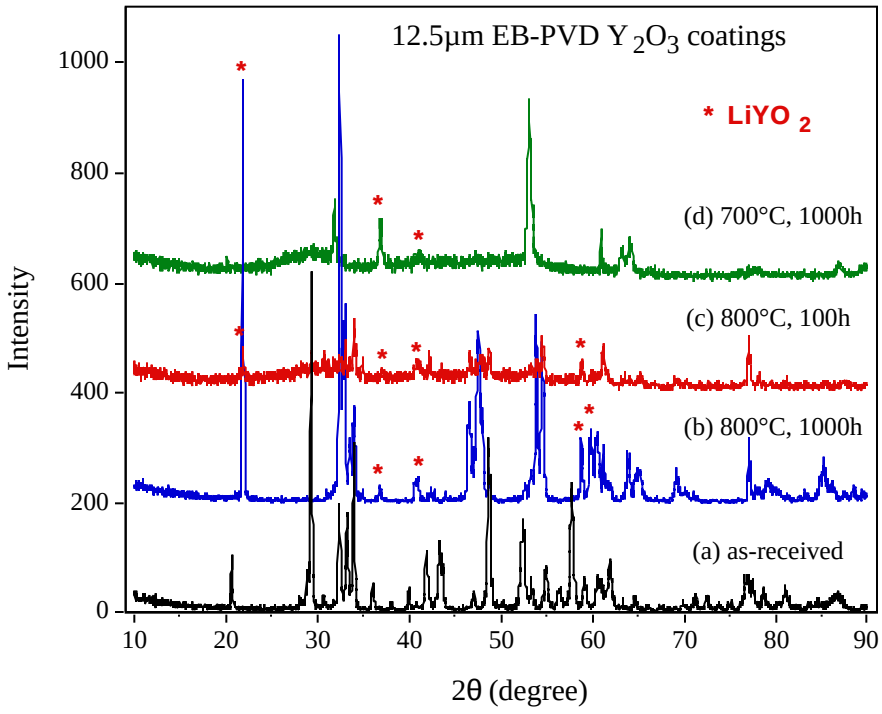

Figure 2. X-ray diffraction data from Y_2O_3 coatings (a) as-received and after exposure to Li for (b) 1000h at 800°C, (c) 100h at 800°C and (d) 1000h at 700°C. Asterisks mark $LiYO_2$ peaks.

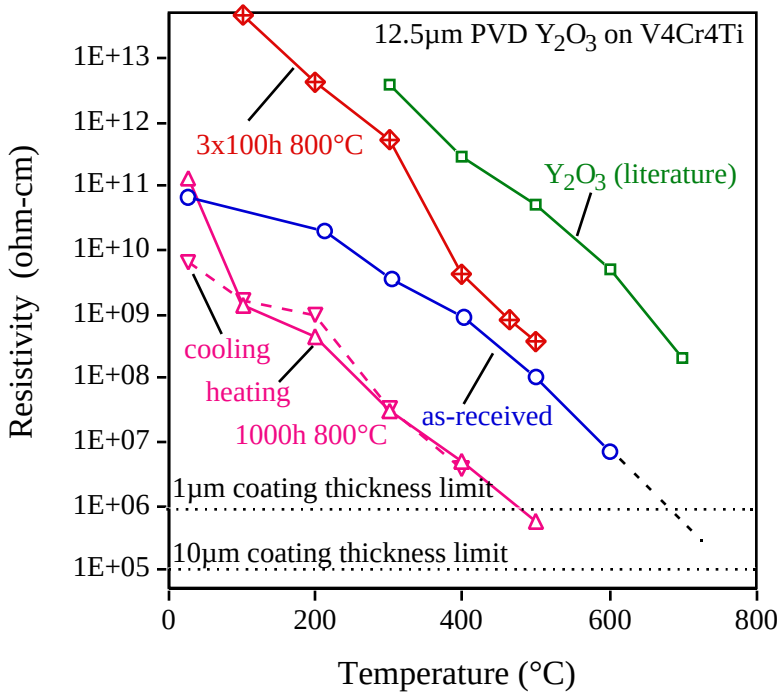

Figure 3. Resistivity as a function of temperature for EB-PVD Y_2O_3 coatings before and after exposure to Li at 800°C.

specimen has not been examined it was difficult to assess whether the mass gain was in the Y_2O_3 coating or the substrate. These specimens will be cross-sectioned at a later stage to better understand any changes in the coating microstructure.

The specimen was examined by AES and Li "nodules" were observed on the coating surface. These nodules were not present when the specimen was first introduced into the vacuum and therefore, must have grown during beam exposure. Their presence indicated that residual Li was present in the coating even after a second cleaning in methanol. Some regions contained only Y and O with no Li detected while other nodules contained Ti. The presence of Ti and Li may explain the specimen mass gain after exposure. The Ti could be from the substrate or the capsule walls. The as-received coating was checked by AES and no Ti was detected.

The specimen exposed for 1000h at 800°C also was examined by XRD and Figure 2b shows that many of the original Y_2O_3 peaks have disappeared and the coating has reacted with Li and possibly Ti to form additional phases. The large peak at 22° matches the pattern for $LiYO_2$ as do several other peaks, however, several of the other major peaks have not been conclusively identified. The observation of $LiYO_2$ is consistent with an earlier study of bulk Y_2O_3 in Li at 500°C.[6] The unidentified peaks could be from other Y-O or Y-Ti-O compounds. The specimen was then coated with a gold electrode to measure the resistivity. Compared to the as-received coating, the Li exposure for 1000h at 800°C appeared to show a significantly lower resistivity, Figure 3. On cooling to room temperature the measured current was significantly higher indicating a lower resistivity by more than an order of magnitude, Figure 3. However, examination of the specimen revealed that ≈30% of the electrode had disappeared. The degradation of the Au electrode has been attributed to a reaction with free Li in the coating, as observed by AES. Lithium readily dissolves Au. The resistance of this specimen will be remeasured with a layered Au-Ni electrode that may be more resistant to reaction with Li.

The specimen exposed for 100h also was examined by XRD, Figure 2c. Again, a mixture of Y_2O_3, $LiYO_2$ and unidentified peaks were observed but at somewhat different intensities than the 1000h exposure. Compared to the 1000h results, many of the $LiYO_2$ peaks were smaller after only a 100h exposure. This observation indicates there is a significant reaction with Li after only 100h and this reaction increases after longer exposures.

The resistivity of the specimen exposed for 3, 100h cycles at 800°C also was measured, Figure 3. In this case, the resistivity measured at low temperatures was higher than the as-received coating but the resistivity measured at higher temperatures was similar to the as-received coating at 400°-500°C. One difference with this measurement was that the voltage was maintained at 5V instead of varying it. By maintaining a constant, low voltage during heating, it was observed that there was less variation in the current measurements and more consistent results were obtained. This may be the reason that higher resistivity values were measured for this specimen. Additional resistance measurements need to be made in this manner with different voltages and dwell times in order to confirm these results.

Two specimens also were exposed at 700°C. The Y_2O_3 specimen exposed for 100h at 700°C showed no visual degradation, but the V-4Cr-4Ti substrate was oxidized during distillation and no further characterization was conducted. The XRD results for the specimen exposed for 1000h at 700°C are shown in Figure 2d. As with the specimens exposed at 800°C, the majority of Y_2O_3

peaks are missing and a few peaks match $LiYO_2$. However, the largest peak at ≈53° has not been identified. Unfortunately this specimen was damaged during handling in the diffractometer and no resistivity measurement was possible.

In terms of meeting the coating metrics of the U.S. Fusion Materials Program,[7] these results come close to showing that Y_2O_3 is a viable MHD coating candidate for Li loop testing. The Li capsule tests performed at 800°C are higher than the required 700°C exposure temperature. Yttria did not meet the requirement of limited (<10%) reaction with Li, but the remaining phases appear to have reasonable resistivity values. The resistivity measurements also need to be continued up to 700°C in order to satisfy the metrics. (The heating elements in the current system were not sufficient to heat the specimen and holder to 700°C. A smaller holder with higher temperature heating elements is being fabricated.) However, the effect of temperature appears to be consistent in each of the measurements suggesting that the current data can be extrapolated to 700°C, Figure 3. If this is done, the as-received coating would marginally meet the required resistivity as would the cycled specimen. However, the specimen exposed for 1000h at 800°C would not.

Based on these results, additional testing is being conducted on this set of coatings. Additional isothermal and cyclic tests are being conducted at 700°C. Because of the increased $LiYO_2$ peaks observed between 100 and 1000h at 800°C, a 2000h exposure at 800°C also is being conducted. The low resistivity of the as-received coating compared to literature values and the problems with measuring resistance on other as-received coatings suggests that the coating quality could be improved. This may result in improved resistivity performance. However, this coating did show good adhesion for a first attempt. Finally, the resistivity measurement was modified slightly for each specimen examined. This procedure needs to be standardized and verified to insure accuracy and reproducibility.

REFERENCES

1. B. A. Pint, J. H. DeVan and J. R. DiStefano, DOE/ER-0313/31 (2001) 132.
2. B. A. Pint, J. H. DeVan and J. R. DiStefano, J. Nucl. Mater. in press.
3. K. Natesan, C. B. Reed, M. Uz, J. H. Park and D. L. Smith, ANL/TD/TM00-10 (2000).
4. B. A. Pint, L.D. Chitwood, J. H. DeVan and J. R. DiStefano, DOE/ER-0313/27 (2000) 49.
5. B. A. Pint, L. D. Chitwood and J. R. DiStefano, J. Nucl. Mater. 289 (2001) 52.
6. T. Mitsuyama, T. Terai, T. Yoneoka and S. Tanaka, Fusion Eng. Design 39-4 (1998) 811.
7. B. A. Pint and J. R. DiStefano, DOE/ER-0313/32 (2002) in press.

8.0 BREEDING MATERIALS

No contributions.

9.0 RADIATION EFFECTS, MECHANISTIC STUDIES, AND EXPERIMENTAL METHODS

TENSILE PROPERTY ESTIMATES OBTAINED USING A LOW COMPLIANCE SHEAR PUNCH TEST FIXTURE – M. B. Toloczko and R. J. Kurtz (Pacific Northwest National Laboratory)* A. Katsunori and A. Hasegawa (Tohoku University, Japan)

OBJECTIVE

The objective was to further understand the nature of deformation in the shear punch test and to use this information to develop a new shear punch test fixture which would provide a better estimate of tensile properties.

SUMMARY

It has been previously shown that for a wide range of BCC and FCC metals, shear punch properties correlate well with uniaxial tensile properties from corresponding miniature tensile tests. However, recent studies of the shear punch test technique have revealed that by more directly measuring punch tip displacement during a shear punch test, the resulting effective shear stress versus displacement trace has a greater similarity to a corresponding tensile test trace. On the assumption that this would lead to shear punch properties that correlate even better with uniaxial tensile properties, shear punch tests were performed on a variety of unirradiated metals, and the shear punch properties were compared to tensile properties from corresponding miniature tensile tests.

Introduction

The shear punch test is a small specimen test technique for estimating uniaxial tensile properties from a transmission electron microscopy (TEM) disk [1-6] (and other sheet stock geometries). A 1 mm flat faced punch is driven through a TEM disk at a constant rate. In the past, some researchers, including the present authors, have assumed that crosshead displacement is approximately equal to the punch displacement, and the load has been plotted as a function of crosshead displacement. The resulting load versus crosshead displacement trace has many features common to a uniaxial tensile test trace including a region of linear loading, a yield point, a region of work hardening (or work softening), and an ultimate load [1,2]. Loads are converted to an effective[1] shear stress by dividing by $2\pi rt$ where "r" is the average of the radii of the punch and the receiving die, and "t" is the thickness of the specimen. The effective shear yield, defined as the point of deviation from linear loading, correlates well with uniaxial yield stress for a variety of materials [2]. The effective shear ultimate stress also correlates well with the uniaxial ultimate strength [2], and true uniform elongation can be correlated with shear punch test data [3].

Recent development of the shear punch test technique has focused on understanding the nature of the slope and intercept of the correlation between uniaxial yield and effective shear yield [7] as well as on identifying ways to reduce the material-to-material scatter in the correlation between uniaxial yield and effective shear yield [8]. Most recently, finite element analysis (FEA) was used to show that the compliance of test machines which have been used (and are typical for tensile tests) is much greater than the elastic compliance of a shear punch test specimen [8]. The FEA work suggested that by measuring displacement at the crosshead, the large test machine compliance would obscure the true load versus specimen displacement behavior. The FEA work also suggested that the correlation between uniaxial yield and shear yield would be improved if yield on a load versus punch tip displacement trace was measured at an offset shear strain in a manner analogous to measuring yield on a uniaxial tensile trace.

The conclusions of the FEA work were recently tested by constructing and using a low compliance shear punch test fixture which is fitted with a displacement measurement transducer that measures

---

* Pacific Northwest National Laboratory (PNNL) is operated for the U.S. Department of Energy by Battelle Memorial Institute under contract DE-AC06-76RLO-1830.

[1] The term "effective" is used because the stress state is known to not be pure shear [7,8]. However, for the sake of brevity, the term "effective" will be assumed for the remainder of this work.

displacement at approximately the top of the punch [9]. Shear punch tests were performed on a variety of materials, and the study firstly showed that there was indeed a large amount of compliance in the test fixture and load-train relative to the elastic compliance of a typical specimen tested in shear. A load versus punch displacement trace had a much different appearance than a corresponding load versus crosshead displacement trace due to the more direct measurement of specimen displacement. The load versus punch displacement traces always had a greater similarity to the corresponding uniaxial test traces. A particular benefit of using punch displacement traces was that it was now possible to measure shear yield at an offset shear strain in a manner analogous to that of a uniaxial tensile test where uniaxial yield is measured at an offset strain. Correlations between uniaxial yield and shear yield were made from crosshead displacement traces and punch displacement traces. Shear yield measured at a 1.0% offset shear strain on the punch displacement traces gave a slightly better correlation than did shear yield measured at deviation from linearity on the crosshead displacement traces.

In the present work, correlations between tensile properties and shear punch properties obtained using the new fixture are compared to correlations previously obtained using an older shear punch fixture with greater compliance [2]. The correlations examined were the yield correlation, the ultimate strength correlation, and the uniform elongation correlation.

Experimental

Testing

A schematic of the new shear punch fixture is shown in Figure 1. The key changes are the revised punch and the introduction of a displacement measurement transducer. The revised punch is estimated to be approximately 8 times stiffer than previous punches which were simply a 1 mm diameter pin, approximately 18 mm in length. Displacement was measured using a capacitive-based displacement measurement device (CDMD). The “stud” shown in Figure 1 is attached to the bottom half of the fixture, and serves as the reference point for the CDMD. As the CDMD is located inside of the “button”, the CDMD roughly measures the displacement of the top of the punch relative to the surface on which the specimen rests, and therefore, test fixture compliance contributions come mainly from the punch only.

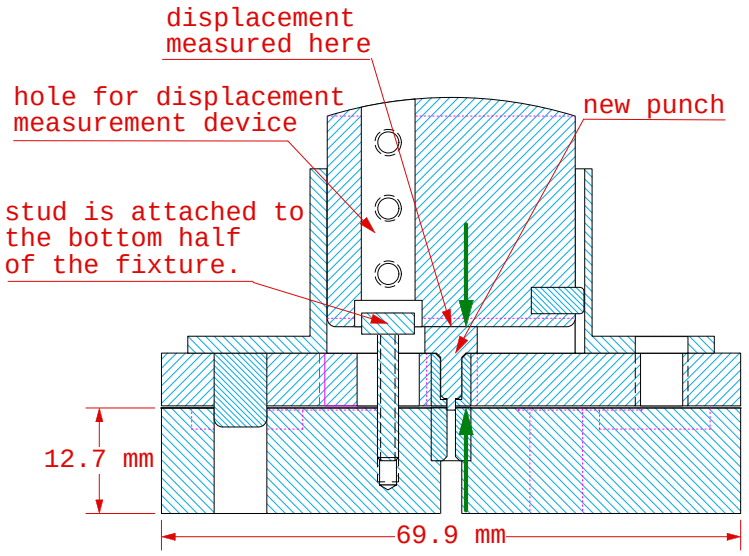

Figure 1. New shear punch fixture. Capacitive based displacement measurement probe measures its position relative to the top of the stud. Green arrows indicate the approximate displacement measurement reference points.

Table 1. Materials examined for this study and their thermomechanical treatments.

Alloy Class	Alloy	Thermomechanical Treatment
Al alloys	5000	0 (solution annealed), H38 (aged and cold-worked)
	6061	0 (solution annealed), T6 (aged)
Stainless steels	316 SS	2 different age and cold-work treatments
	HT9	2 different tempering treatments
Low carbon steel	1010	solution annealed, cold-worked
Brass	CDA-260	solution annealed, cold-worked
Cu alloys	$CuHfO_2$	cold-worked
	MZC3	precipitation strengthened

Materials and thermomechanical treatments used in this study are shown in Table 1. All specimens were electro-discharge machine (EDM) fabricated from sheet stock with a thickness of approximately 0.25 mm. A minimum of three shear punch tests and two tensile tests were performed per each unique combination of material and thermomechanical treatment.

The punch had a tip diameter of 0.98 mm while the receiving hole diameter was 1.04 mm. This gives a clearance, w, of 0.32 mm which is slightly larger than the previously used value of 0.25 mm. The initial shear strain rate, as calculated from

$$\dot{\varepsilon}_{rz} = \frac{1}{2}\frac{\dot{x}}{w} \tag{1}$$

where $\dot{x}$ is the punch displacement rate, was approximately $4x10^{-3}$ sec^{-1}. The factor of 1/2 in Eqn. 1 results from converting the shear strain to an engineering shear strain[2]. Displacement was simultaneously measured at the CDMD and at the crosshead. Load was converted to an effective shear stress by dividing by $2\pi rt$ where "r" is the average of the punch and receiving die radii, and "t" is the specimen thickness.

The S1 tensile geometry (1.2 mm gage width, 5 mm gage length) was used for the tensile specimens. The initial strain rate was approximately $1x10^{-4}$ sec^{-1}. Displacement was measured at the crosshead. Yield was measured at a 0.2% offset strain.

Correlation Development

Based on the FEA work [8], a 1.0% offset shear strain was used as the point at which shear yield strength (τ_y) was measured in the punch displacement traces from the new fixture. The shear yield values were empirically correlated with 0.2% offset uniaxial yield strength taken from the corresponding tensile tests. Shear ultimate strength (τ_m) was calculated at the point of maximum load on a shear punch test trace and was correlated with ultimate tensile strength. A strain hardening exponent, n_τ, calculated from the ratio of shear ultimate to shear yield, serves as a ductility parameter which was correlated with true uniform elongation from the corresponding uniaxial tensile tests [3]. The formula for calculating n_τ is given by:

[2] $\varepsilon_{rz} = \varepsilon_{zr} = 1/2(\gamma_{rz} + \gamma_{zr})$, $\gamma_{rz} = x/w$, $\gamma_{zr} = 0$

$$\left(\frac{n_\tau}{0.002}\right)^{n_\tau} = \frac{\tau_m}{\tau_y} \tag{2}$$

This equation results from combining the Power Law Strain Hardening equation with the equality that occurs between the strain hardening exponent and the true uniform elongation at the point of necking.

Results

It has been previously shown that the traces obtained from the new fixture more closely resemble the corresponding tensile traces than traces from older fixtures [9]. An example for a 5000 series Al alloy is shown in Figure 2 where it can be seen that the elastic loading slope of the punch displacement trace is steeper than that of the crosshead displacement traces. In general, it was observed that the greatest similarity between shear punch test traces and uniaxial tensile test traces occurred when the uniform elongation of the material was relatively low. This trend can be understood by considering that in a shear punch test, reduction in load bearing area is increasingly controlled by cutting of the material as punch displacement becomes very large. Thus, for materials which display low uniform elongation, cutting has a minimal effect on reduction in area in a shear punch test.

Yield Strength Correlation

The new correlation between uniaxial yield and 1.0% offset shear yield using the low compliance fixture is compared with a previously obtained correlation between uniaxial yield and shear yield at deviation from linearity using an older fixture with more compliance. These correlations are shown in Figures 3a and 3b, respectively, and are referred to as “2001” and “1994” correlations, respectively. Two sets of tensile tests and two sets of shear punch tests were performed to obtain the data, and many of the specimens for both correlations came from the same sheet stock. These materials can be inferred from the legends. The overall difference in the correlations is not great with the materials common to both correlations having the same relative positions on the plots. There is a difference in the slope of the correlations lines though, and this is due to differences in both shear yield values and uniaxial yield values for the tests conducted in 2001 and 1994.

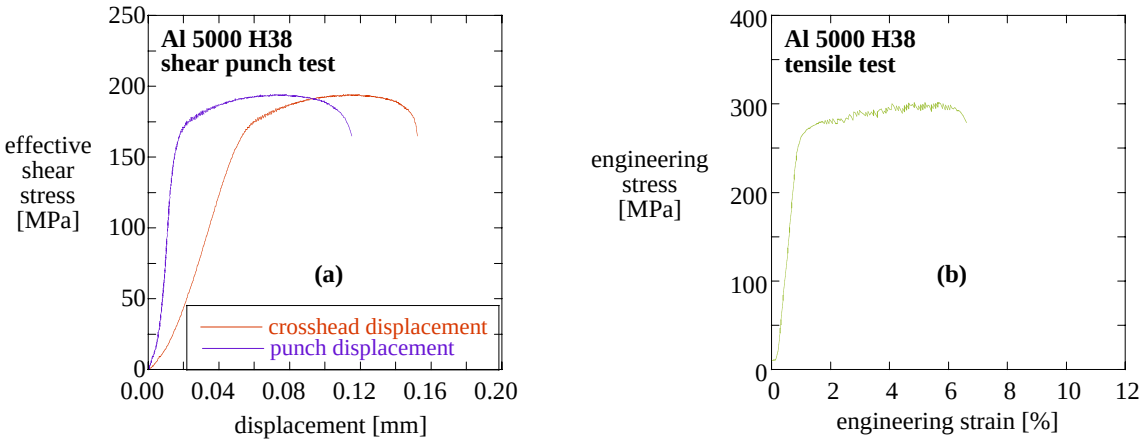

Figure 2. a) Shear punch and b) tensile traces for Al 5000-H38. Note that strain serrations are present in the shear punch test traces.

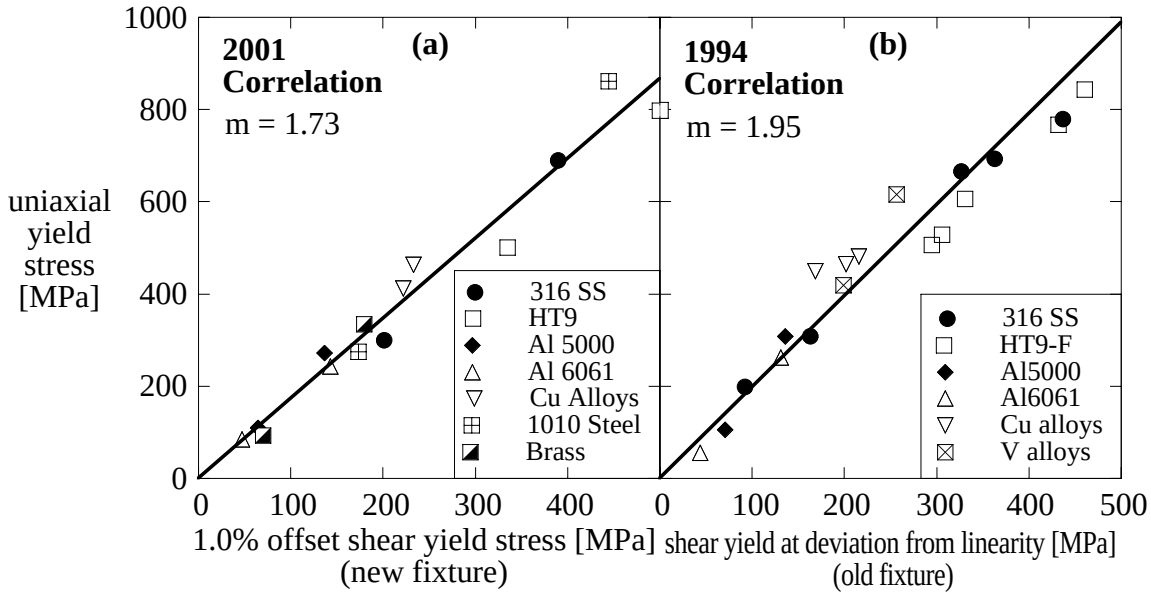

Figure 3. Correlation between uniaxial yield and shear yield for a) 1.0% offset shear yield on punch displacement traces using the new low compliance fixture and b) deviation from linearity on crosshead displacement traces using an older fixture with more compliance. Two sets of tensile tests and shear punch tests were performed to obtain this data. Many of the specimens for the two sets of tests came from the same sheet stock, and these can be inferred from the legends.

Ultimate Strength Correlation

The new correlation between uniaxial ultimate strength and shear ultimate strength is shown in Figure 4a and can be compared to the previous correlation shown in Figure 4b. For the materials which are present in both sets of correlations, the overall trends in the data are again similar, and a single trend line passing through the origin can adequately represent the data in both instances. However, the slope of the correlation lines is slightly different, and this is due to systematic differences in both the shear ultimate strength and the uniaxial ultimate strength values for the tests conducted in 2001 and 1994. The shear ultimate values for the tests performed in 2001 were, on average, slightly higher than those performed in 1994 while the uniaxial ultimate values for the tests performed in 2001 were on average slightly lower than the uniaxial ultimate values from the tests performed in 1994. It is logical to attempt to associate these differences with differences in test techniques, and there were some notable differences in test techniques between 2001 and 1994. For the shear punch tests, not only was a low compliance fixture used in 2001, but also the crosshead displacement rate was a factor of two lower. It would be expected that if the materials were strain rate sensitive, a lower crosshead displacement rate would lead to lower shear ultimate values, but in fact, the opposite occurred. Therefore, the reason for the slight increase in shear ultimate with the new fixture is not yet understood. For the tensile tests, the key difference is that a smaller specimen geometry was used for the tests performed in 1994. It has been observed that UTS values from miniature sheet type specimens are often higher than values from larger size sheet type specimens [10], so the differences in the tensile data can reconciled.

Ductility Correlation

Based on previous studies of the shear punch test, it was found that n_τ correlates best with the true uniform elongation measured in corresponding uniaxial tensile tests [3]. Shown in Figure 5a is the correlation between true uniform elongation and n_τ for shear punch tests performed using the low

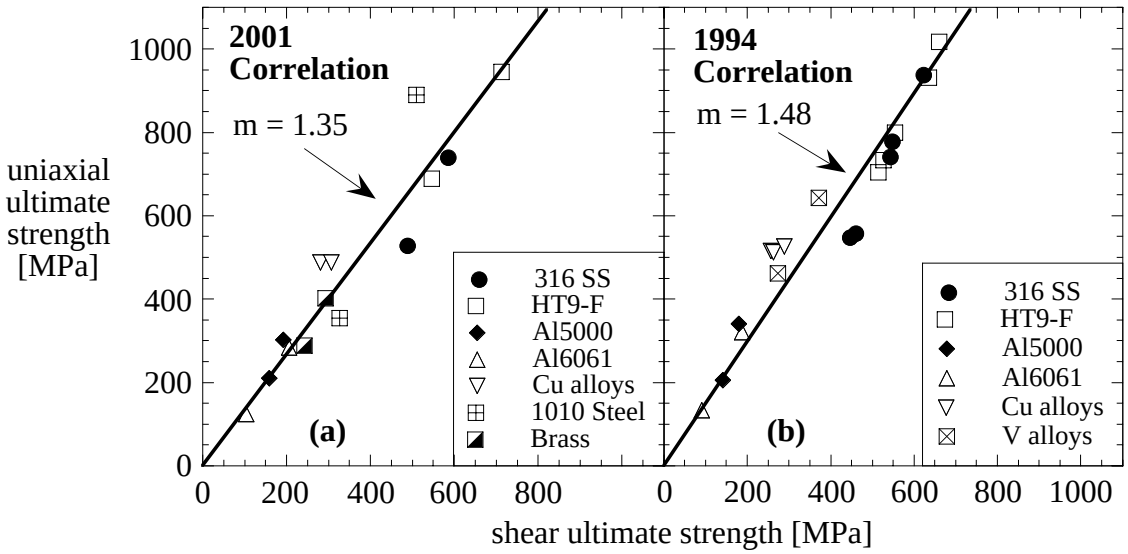

Figure 4. a) Correlation between uniaxial ultimate and shear ultimate using a reduced compliance fixture and b) a previous correlation between uniaxial ultimate and shear ultimate constructed using an older fixture with greater compliance. While some of the materials were the same for the correlations, both uniaxial and shear strength values came from two sets of tests with one set of tests performed in 1994 and the other set performed in 2001.

compliance fixture. Figure 5b shows a correlation between true uniform elongation and n_τ for shear punch tests performed in 1994 using an older fixture with more compliance. Overall, the correlations are largely similar with both correlations having approximately the same slope and same intercept. The values for the slope and the intercept have been previously explained [3]. The correlation constructed using the low compliance fixture does however, show more scatter about the trend line. As with the UTS correlation, there were small differences between the ε_u values and the n_τ values for the tests performed in 2001 and 1994 which led to increased scatter at the higher ductility values. Because there were differences in the values of both ε_u and n_τ for the two sets of tests, the increased scatter is not due to changes in the shear punch test technique alone but also the tensile test technique, again showing that the correlation is sensitive to the shear punch test and the tensile test technique.

Discussion

The FEA simulations of the shear punch test [8] suggested that the 2001 yield strength correlation would have much less scatter than the 1994 yield strength correlation, but in fact, the magnitude of the scatter was comparable. In a previous study of the new fixture, some of the predicted changes in the shear yield values from the FEA study were observed in the actual shear punch tests using the new fixture, but the changes were not as large as were predicted [9]. Perhaps this is because the finite element model did not incorporate deviations from ideal test behavior such as a slightly off-center punch or a slightly tilted punch. Or perhaps it is because some aspect of the deformation behavior of the test materials was not modeled as accurately as possible, such as the fact that the deformation behavior was assumed to be isotropic.

The high degree of similarity between the 2001 and 1994 ultimate strength correlations is understandable in that the ultimate load on a shear punch test can be determined unambiguously irrespective of the method by which displacement is measured. The one factor that could have made a difference between the shear ultimate strength values for the 2001 and 1994 tests is that the crosshead speed was a factor of two lower for the 2001 shear punch tests. This does not appear to have had an effect because if there

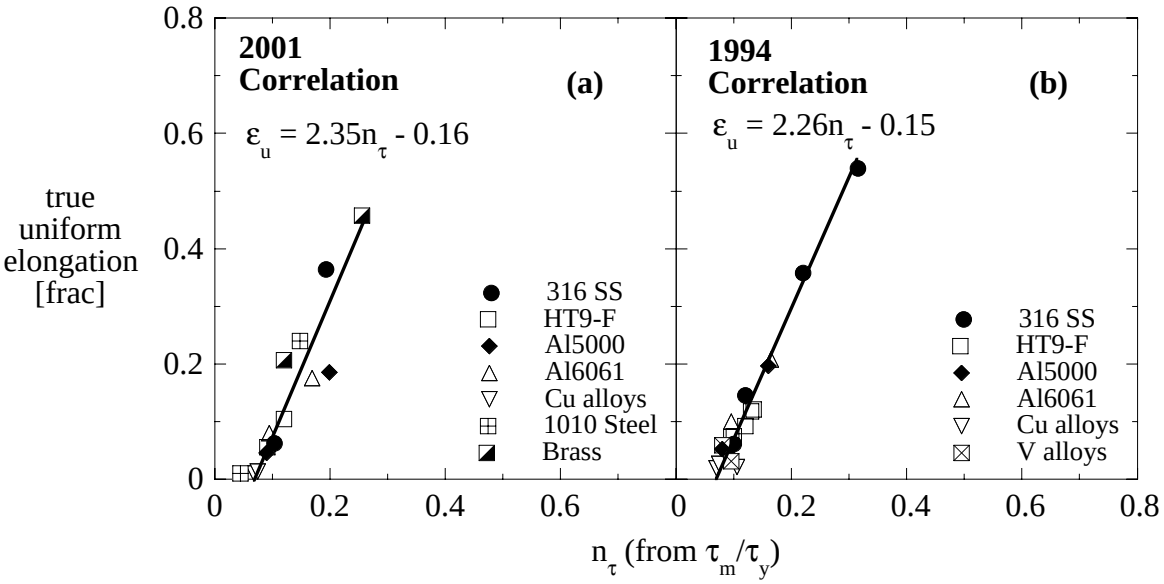

Figure 5. a) Correlation between true uniform elongation and n_τ using a reduced compliance fixture. b) A previous correlation between true uniform elongation and n_τ constructed using an older fixture with greater compliance. While some of the materials were the same for the correlations, the data came from two sets of tests with one set of tests performed in 1994 (higher compliance fixture) and the other set performed in 2001 (low compliance fixture).

were a strain rate effect, it should have been to reduce the shear ultimate values for the 2001 correlation relative to the 1994 correlation, but the opposite occurred.

As for the ductility correlation, it is understandable that the 2001 and 1994 ductility correlations are similar because both the shear yield and the shear ultimate values for the 2001 and 1994 correlations were only slightly different, and the shear punch ductility parameter is calculated from the ratio of these two values.

Because the correlations derived from the low compliance fixture are largely similar to the previously obtained correlations using an older fixture with more compliance, it would seem that there is no benefit to using a lower compliance fixture. However, there are other aspects of the shear punch test to consider. The low compliance fixture produces a test trace that better represents the deformation behavior of the specimen, and the test trace shape has a greater similarity to a corresponding tensile test. This is beneficial because it shows that the shear punch test reveals the same basic material behavior that would be observed in a tensile test. Further, by displacement at the punch, it has become possible to rationalize a shear strain in the early stages of a shear punch test which permits an unambiguous measurement of shear yield at an offset shear strain.

Summary and Conclusions

A new shear punch fixture with lower compliance and having a method for more direct measurement of crosshead displacement was constructed and evaluated. Yield strength, ultimate strength, and ductility correlations derived from shear punch tests using the new fixture along with corresponding tensile tests were compared to yield strength, ultimate strength, and ductility correlations obtained previously from shear punch tests using an older fixture with more compliance and a corresponding set of tensile tests. The correlations from the new shear punch fixture were largely similar to their respective correlations from the older shear punch fixture with more compliance. There were, however, some small differences in the

new and old correlations, and these differences were found to be due to small changes in both the shear punch values and the tensile values.

While the low compliance fixture did not have a big impact on the correlations, the new fixture is an improvement over the older fixture because the new fixture produces a shear punch test trace that has a greater degree similarity to a corresponding tensile test trace, and with the new fixture, shear yield can be measured unambiguously at an offset shear strain in a manner analogous to a tensile test.

REFERENCES

[1] G. E. Lucas, G. R. Odette, and J. W. Sheckard, The Use of Small-Scale Specimens for Testing of Irradiated Material, ASTM STP 888, 1986, pp. 112-140.

[2] M. L. Hamilton, M. B. Toloczko, and G. E. Lucas, Miniaturized Specimens for Testing of Irradiated Materials, IEA International Symposium, P. Jung and H. Ullmaier, eds., Forschungszentrum Jülich GmbH, 1995, pp. 46-58.

[3] M. B. Toloczko, M. L. Hamilton, and G. E. Lucas, Journal of Nuclear Materials, Vols. 283-287, 2000, pp. 987-991.

[4] M. L. Hamilton, M. B. Toloczko, D. J. Edwards, W. F. Sommer, M. J. Borden, J. A. Dunlap, J. F. Stubbins, and G. E. Lucas, Effects of Radiation on Materials: 17th International Symposium, ASTM STP 1270, 1996, 1057-1067.

[5] G. L. Hankin, M. B. Toloczko, M. L. Hamilton, F. A. Garner, and R. G. Faulkner, Journal of Nuclear Materials, Vols. 258-263, 1998, pp. 1657-1663.

[6] M. L. Hamilton, G. L. Hankin, M. B. Toloczko, F. A. Garner, and R. G. Faulkner, Effects of Radiation on Materials: 19th International Symposium, ASTM-STP 1366, 1999, pp. 1003-1017.

[7] G. L. Hankin, M. B. Toloczko, K. I. Johnson, M. A. Khaleel, M. L. Hamilton, F. A. Garner, R. W. Davies, and R. G. Faulkner, Effects of Radiation on Materials: 19th International Symposium, ASTM STP 1366, 1999, 1018-1028.

[8] M. B. Toloczko, K. Abe, M. L. Hamilton, F. A. Garner, and R. J. Kurtz, Fourth Symposium on Small Specimen Test Techniques, ASTM STP 1418, January 23-25, 2001, to be published.

[9] M. B. Toloczko, R. J. Kurtz, A. Hawegawa, and K. Abe, “Shear punch tests performed using a new low compliance fixture”, presented at the *10th International Conference on Fusion Reactor Materials*, held in Baden-Baden, Germany, Oct. 14-19, 2001, to be published in the *Journal of Nuclear Materials*.

[10] N. F. Panayotou, S. D. Atkin, R. J. Puigh, and B. A. Chin, “Design and Use of Nonstandard Tensile Specimens for Irradiated Materials Testing”, *The Use of Small-Scale Specimens for Testing Irradiated Material, ASTM STP 888*, W. R. Corwin and G. E. Lucas, Eds., American Society for Testing and Materials, PA, 1986, pp. 201-219.

10. DOSIMETRY, DAMAGE PARAMETERS, AND ACTIVATION CALCULATIONS

Surprisingly Large Generation and Retention of Helium and Hydrogen in Pure Nickel Irradiated at High Temperatures and High Neutron Exposures - L. R. Greenwood, F. A. Garner, and B. M. Oliver (Pacific Northwest National Laboratory)*, M. L. Grossbeck (Oak Ridge National Laboratory), and W. G. Wolfer (Lawrence Livermore National Laboratory)

OBJECTIVE

The objective is to predict and measure gas production in fusion relevant materials.

SUMMARY

Hydrogen and helium measurements in pure nickel irradiated to 100 dpa in HFIR at temperatures between 300 and 600°C show higher gas concentrations than predicted from fast-neutron reactions and the two-step $^{58}Ni(n,\gamma)^{59}Ni$ (n,p and n,α) reactions. This additional gas production suggests previously unidentified nuclear sources of helium and possibly hydrogen that assert themselves at very high neutron exposure. The elevated hydrogen measurements are especially surprising since it is generally accepted that hydrogen is very mobile in nickel at elevated temperatures and therefore is easily lost, never reaching large concentrations. However, it appears that relatively large hydrogen concentrations can be reached and retained for many years after irradiation at reactor-relevant temperatures. These new effects may have a significant impact on the performance of nickel-bearing alloys at high neutron fluences in both fission and fusion reactor irradiations.

PROGRESS AND STATUS

Introduction

Until recently, the production and retention of helium and hydrogen in nickel, iron, and stainless steels was thought to be well predicted by the combination of fast neutron (n,He) and (n,H) reactions as well as the well-known two-step $^{58}Ni(n,\gamma)^{59}Ni$ (n,p and n,α) reactions. The ^{59}Ni reaction is a prolific source of helium that has been used to achieve helium to dpa (displacements per atom) ratios that simulate fusion reactor conditions in mixed-spectrum fission reactor irradiations. Earlier helium measurements in the High Flux Isotopes Reactor (HFIR) appeared to be in good agreement with calculations and neutron dosimetry measurements up to thermal neutron fluences of about $4x10^{22}$ n/cm^2. [1-2] Recently, however, new helium measurements at much higher thermal neutron fluences up to $1.1x10^{23}$ n/cm^2 show an excess of helium over the predictions. Furthermore, measurements using a new hydrogen system developed recently at PNNL [3], have shown that pure nickel samples irradiated to the same high fluences also have more hydrogen than would be predicted. These elevated hydrogen measurements are especially surprising since hydrogen is thought to be very mobile at the temperatures of the HFIR experiments so that the hydrogen would diffuse out of the samples, never reaching the levels observed in our measurements.

Impact on Materials Research

The two-step nickel reaction can produce high levels of helium and hydrogen in stainless steels and Inconel in fission reactor components irradiated to high neutron fluences. These reactions are also widely used to produce helium in stainless steels in mixed spectrum fission reactor irradiations in order to simulate the helium to dpa ratios expected for a fusion reactor. In both cases, confident prediction of the gas production, as well as the increased dpa due to the energetic recoils, is clearly required for the understanding of material property effects that may arise from the trapped helium. It is well known that helium and other gases stabilize small vacancy clusters to form bubbles and void cavities, thereby accelerating the onset of void swelling. Recently, it has been proposed that hydrogen can also perform

* Pacific Northwest National Laboratory (PNNL) is operated for the U.S. Department of Energy by Battelle Memorial Institute under contract DE-AC06-76RLO-1830.

this role. [4] Furthermore, it has been suggested that hydrogen may influence the development of irradiation assisted stress corrosion cracking, although no convincing evidence of hydrogen's direct role has yet been provided. The high levels of hydrogen seen in these measurements strongly suggest that hydrogen may be trapped in the voids and cavities along with the helium. [4]

Neutron Irradiations and Reactor Dosimetry

All of the samples used for the hydrogen and helium measurements were high purity nickel wires used for neutron dosimetry in various HFIR materials irradiation experiments for US and Japanese fusion reactor materials programs. [5] Typically, reactor dosimetry capsules containing small milligram-sized wires of Fe, Ni, Ti, Nb, and Co-Al alloy were placed at various elevations in materials irradiation assemblies located in either the peripheral target position or removable beryllium positions of HFIR. These wires were analyzed to determine activation rates that were used to adjust the neutron fluence spectra at each location of the reactor dosimetry capsules. Consequently, the neutron exposures are very well known for all of the samples used to measure helium and hydrogen that are cited in this paper. It is important to note that both the thermal and fast neutron fluences must be well-known since the total gas production in nickel is due to both the $^{58}Ni(n,\gamma)^{59}Ni(n,p$ and $n,\alpha)$ two-step thermal reactions as well as the more conventional fast neutron (n,hydrogen) and (n,helium) reactions, which include all fast neutron reactions that lead to gas production. Since the reactor dosimetry measurements are non-destructive, the nickel dosimeters could be used subsequently to measure both the helium and the hydrogen contents.

Helium Measurements

The helium was measured with high accuracy by isotope dilution mass spectrometry at PNNL. Samples were slightly acid etched to remove surface effects, then melted in a furnace to release all of the helium gas. A known ^{3}He spike was added and the ratio of ^{3}He to ^{4}He was used to determine the absolute number of ^{4}He atoms in the samples. Some of the helium data at lower neutron fluences [1] was originally measured at Rockwell International prior to the move of the helium analysis system from Rockwell to PNNL in 1996. All of the helium measurements for pure nickel samples irradiated in HFIR are shown as a function of the thermal neutron fluence in Figure 1. The measured helium values range up to about 35,000 appm or about 3.5 at%. The stainless steel dpa values are shown near each helium measurement since stainless steel dpa is typically used as an exposure parameter for the HFIR irradiations. The dpa values for the pure nickel samples would be considerably higher, up to about 100 dpa, due mainly to the extra dpa from the high energy recoil from the $^{59}Ni(n,\alpha)$ reaction. The Ni dpa values are 59, 78, and 104 for the corresponding stainless steel values of 34, 44, and 59 dpa shown on

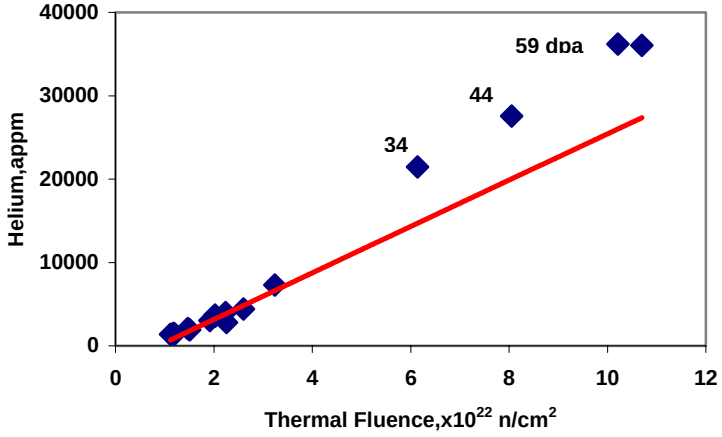

Figure 1. Measured and calculated helium production from nickel irradiated in HFIR. The solid line is calculated using the evaluated ^{59}Ni cross sections.

Figure 1. The line in Figure 1 represents the standard calculation of helium from nickel, as will be discussed in more detail below.

Hydrogen Measurements: A new hydrogen analysis system was developed at PNNL in 1999. [3] This system heats samples to approximately 1200^{o}C to release the hydrogen without melting or vaporizing the samples. Hydrogen leak standards are used to calibrate the system. In addition to rapid hydrogen release at a fixed temperature, hydrogen can also be measured as a function of increasing temperature. Figure 2 shows that most of the hydrogen in pure irradiated nickel is released by 700^{o}C, well below the maximum temperature used to extract the hydrogen from the irradiated nickel samples. The hydrogen measurements for pure nickel irradiated in HFIR are shown in Figure 3. The diamonds show the measured values while the circles show the calculations using the standard model, as described below. The dpa values shown on the figure again refer to stainless steel rather than nickel since the HFIR experiments involved mainly stainless steel samples. As can be seen, the measured hydrogen values exceed the predicted values in all cases over the range of temperatures from 300 to 600^{o}C. It should be noted that the excess hydrogen seen in the samples could be due to environmental sources rather than simply nuclear production. The HFIR samples are not in contact with water, which is known to produce copious amounts of hydrogen through radiolysis in water reactors. However, at the elevated temperatures of the HFIR experiments, hydrogen is very mobile so that the samples have a flux of hydrogen moving through them during the experiment. The main point is that some of this hydrogen must be retained at the end of the experiment, contrary to our usual expectations. It should also be mentioned that the exact temperature values are not known since the dosimetry capsules were located between experimental capsules that had temperature monitoring. The dosimeters are believed to have temperatures between the values of the adjacent experimental assemblies, although exact values are not available.

Calculated Helium and Hydrogen Production in Nickel: The production of helium and hydrogen in nickel, iron, and stainless steel has been discussed previously. [1,2] The fast and thermal neutron (n,H) and (n,He) cross sections for natural nickel were obtained from the ENDF/B-VI data files, which include ^{59}Ni as well as the natural isotopes.[6] The cross sections for individual nickel isotopes, are shown in Figures 4, 5, and 6. It is noteworthy that the gas production cross sections for natural nickel are not appropriate for these high fluence irradiations in HFIR since there is significant transmutation both between the various nickel isotopes as well as the production of many non-nickel isotopes. Figure 7 shows a schematic representation of the isotopes that are produced by high fluence thermal neutron irradiations of pure nickel, including both stable and radioactive products. Gas production calculations at high neutron fluences must then take into effect the transmutation between the various Ni isotopes as well as transmutation to isotopes of other elements.

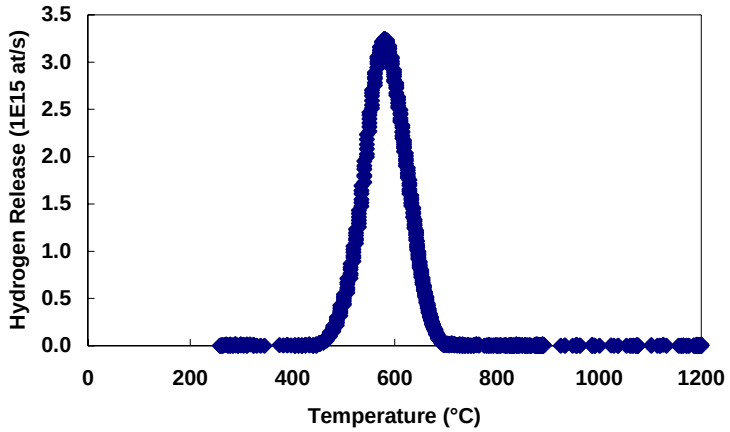

Figure 2. Hydrogen release from irradiated nickel sample as a function of temperature.

Most of the transmutation, as shown in Figure 7, that occurs in these high fluence irradiations consists of neutron capture (n,γ) reactions that have the effect of increasing the isotopic abundances of the higher-mass nickel isotopes as well as the radioactive isotopes ^{59}Ni and ^{63}Ni. As can be seen from Figures 5 and 6, the burnout of ^{58}Ni to ^{59}Ni increases the net fast neutron gas production, as well as the

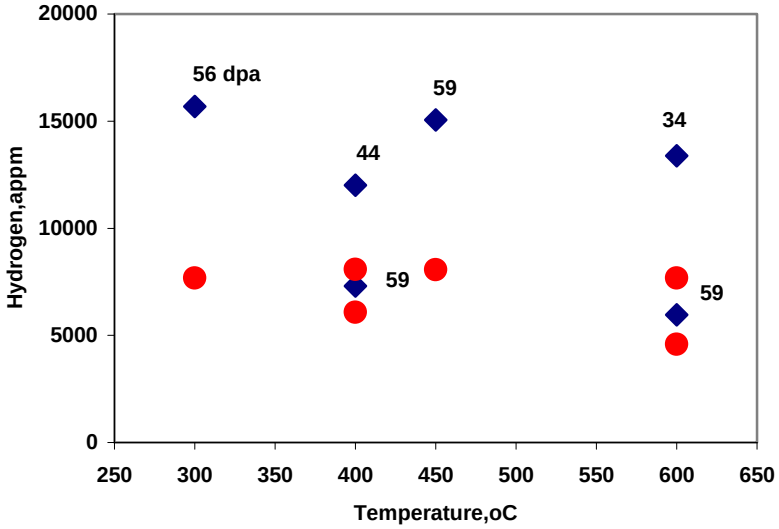

Figure 3. Measured (diamonds) and calculated (dots) hydrogen in nickel irradiated in HFIR to various 316SS dpa values.

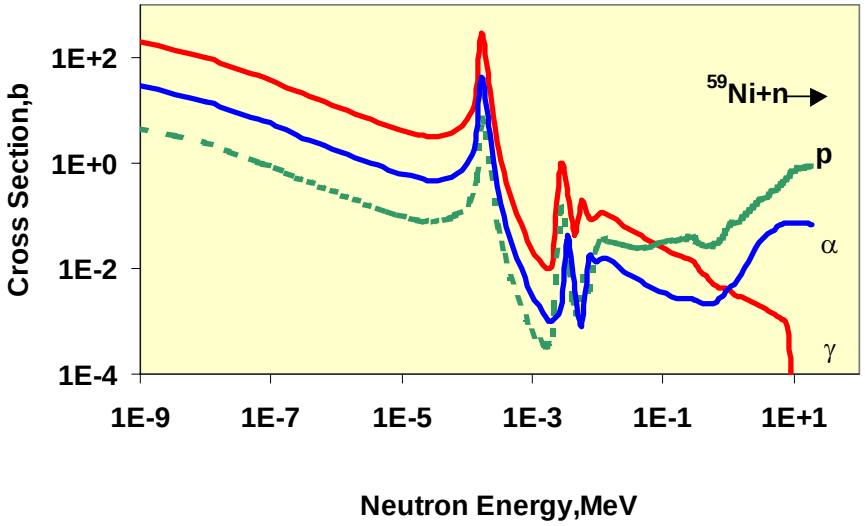

Figure 4. Evaluated neutron cross sections for ^{59}Ni from ENDF/B-VI.

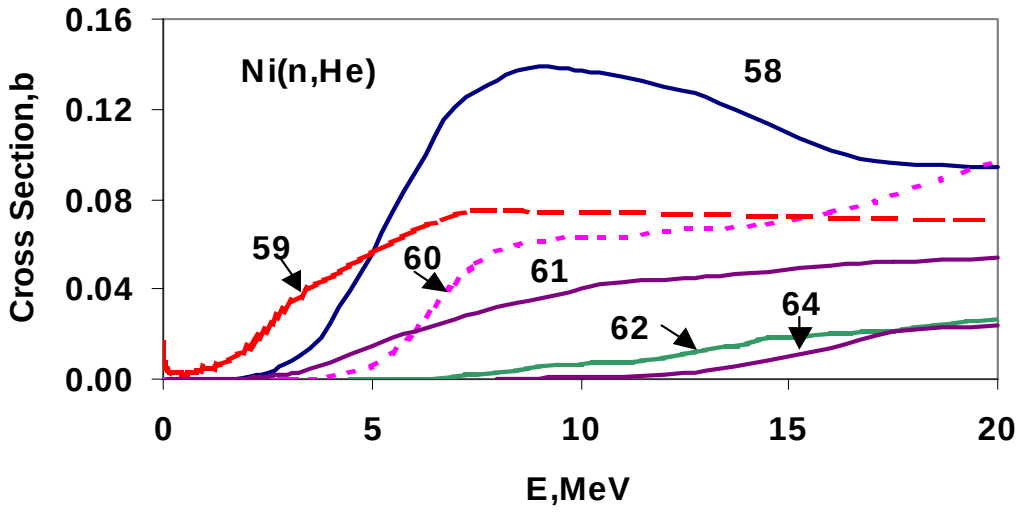

Figure 5. Total helium production cross sections for the nickel isotopes.

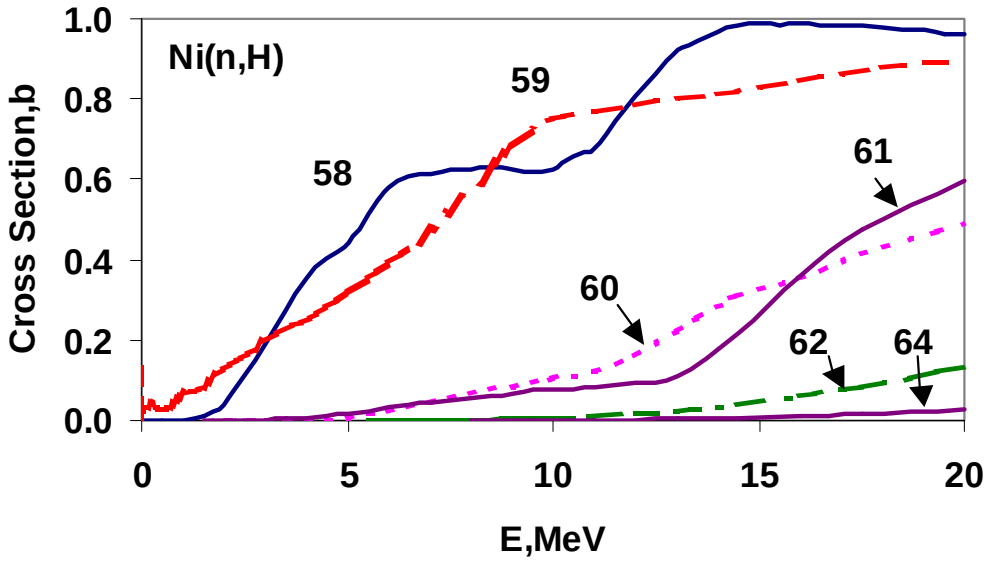

Figure 6. Total hydrogen production cross sections for the nickel isotopes.

thermal neutron production. However, at increasingly higher neutron fluences, as both the ^{58}Ni and ^{59}Ni are consumed, the net fast neutron gas production from Ni will actually decrease since the higher mass nickel isotopes have lower cross sections. The gas production from ^{63}Ni has not been measured or calculated. However, based on the Q-values, these reaction cross sections are thought to be similar to those for the other, higher mass nickel isotopes. All of the hydrogen and helium calculations were performed by integrating the various cross sections in figures 4-6 over the HFIR neutron energy spectra, then combining the fast neutron and ^{59}Ni reactions to get the total gas production.

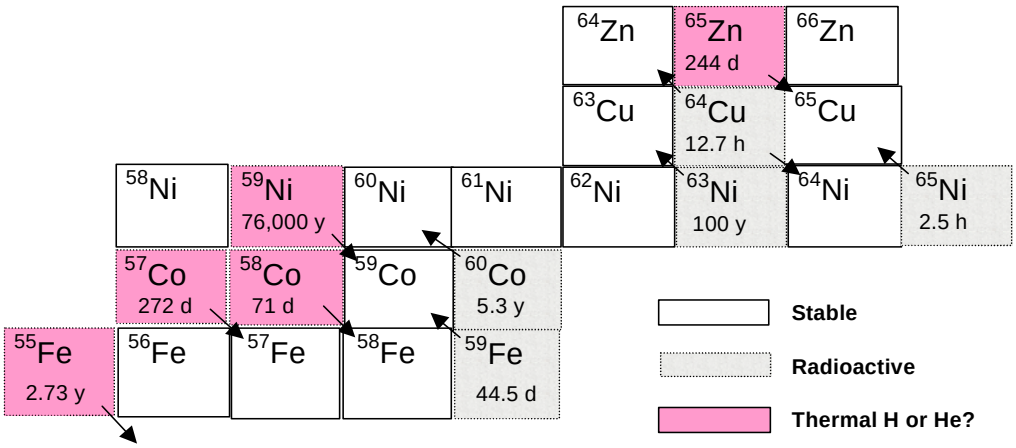

Figure 7. Table of isotopes surrounding nickel region showing stable (white), radioactive candidates for thermal neutron helium cross section (gray), and radioactive isotopes that are not candidates (light gray).

Comparison of Calculated and Measured Gas Production

Figures 1 and 3 show the calculated production of helium and hydrogen in pure nickel from both the thermal neutron reactions for ^{59}Ni as well as the transmutation between the nickel isotopes for the fast neutron gas production. As can be seen, both the helium and the hydrogen measurements are significantly higher than the calculations at the higher neutron fluences. As mentioned above, the net transmutation to higher mass nickel isotopes with increasing neutron exposure has little effect on the net gas production since the various nickel isotopes have similar cross sections and, more importantly, gas production is dominated by the ^{59}Ni reactions. Since the excess hydrogen is most likely due to environmental sources, only the excess helium production needs to be explained.

The discrepancy between the helium measurements and calculations may be due in part to uncertainties in the nuclear reaction cross sections for both ^{58}Ni and ^{59}Ni as well as the neutron dosimetry measurements. The production of helium or hydrogen from the two-step nickel reaction ^{58}Ni(n,γ)^{59}Ni (n,p or n,α) is given by:

$$N(x)/N_o(Ni) = \quad 0.6808\ \sigma_X \{\sigma_\gamma(1-e^{-\sigma_T \phi t}) - \sigma_T(1-e^{-\sigma_T \phi t})\} / \sigma_T\ (\sigma_\gamma - \sigma_T) \qquad (1)$$

Where N(x) = atoms of H or He, N_o(Ni) = initial atoms of Ni, 0.6808 is the abundance of ^{58}Ni, σ_x = spectral averaged reaction cross section for p or α from ^{59}Ni, σ_γ = cross section for ^{58}Ni(n,γ), σ_T = total absorption cross section for ^{59}Ni, and ϕt = the total neutron fluence.
Although the calculations averaged these reaction cross sections over the entire HFIR neutron spectrum, the largest contribution is due to the thermal neutrons. Hence, we can determine the sensitivity of the helium production to the uncertainties in the cross sections by varying only the thermal neutron cross sections. Table 1 lists the evaluated thermal neutron cross sections for ^{58}Ni and ^{59}Ni.

Table 1. Thermal Neutron Cross Sections for Ni Gas Production

Reaction	Cross Section, barns
^{58}Ni(n,γ)^{59}Ni	4.6 $\pm$ 0.3
^{59}Ni(n,γ)^{60}Ni	77.7 $\pm$ 4.1
^{59}Ni(n,p)^{59}Co	2.0 $\pm$ 0.5
^{59}Ni(n,α)^{56}Fe	12.3 $\pm$ 0.6
^{59}Ni(n,total absorption)	92.0 $\pm$ 4.0

The uncertainties in the ^{59}Ni cross sections listed in Table 1 cannot explain the differences seen between the measured and calculated helium data, especially in light of new ^{59}Ni measurements presented below. Uncertainties in the neutron fluences determined by the reactor dosimetry measurements are also too small to explain the excess helium production; especially since all of the HFIR data have the same systematic sources of uncertainty.

Mass Spectrometry Measurements of ^{59}Ni

In order to rigorously test the ^{59}Ni total absorption cross section, the nickel isotopic ratios were measured by thermal ionization mass spectrometry for the nickel samples irradiated to high exposures in HFIR and the results are listed in Table 2. The samples were dissolved in acid and the nickel fraction was separated by ion exchange reactions. The separated nickel fractions were then loaded onto filaments and heated to measure the nickel isotopic ratios. An unexpected interference from copper was seen at mass 63 and 65. Consequently, ^{63}Ni was measured separately by liquid scintillation counting to properly normalize the data. The net uncertainty on the ^{59}Ni content of the samples is estimated to be only 1%.

The ^{59}Ni content only depends on the production cross section from ^{58}Ni and the total absorption or burnup cross section and decay of ^{59}Ni. As shown in Table 1, the ^{58}Ni(n,γ)^{59}Ni cross section is quite well known. Consequently, the ^{59}Ni data in Table 2 rigorously tests the ^{59}Ni total absorption cross section. Table 2 also lists the calculated ^{59}Ni content in the samples using the evaluated cross sections, as explained above. As can be seen, the ^{59}Ni measurements and the calculations are in excellent agreement with C/M = 1.017$\pm$0.009, much better agreement than might be expected from the uncertainties in the cross sections listed in Table 2. The measured data and calculations are also in excellent agreement (within $\pm$2%) for ^{58}Ni and ^{60}Ni, as shown in Figure 8. The fit to the data can be improved slightly by raising the ^{59}Ni total absorption cross section by 1.6% to 93.5 barns. However, this adjustment is within the estimated 2% 2-σ uncertainty in the TIMS data and is not justified considering the other uncertainties in the calculation due to both the ^{58}Ni cross section as well as the neutron fluence measurements. Furthermore, increasing the ^{59}Ni absorption cross section lowers the helium production from nickel, increasing the discrepancy with the helium measurements. The conclusion is that the ^{59}Ni nickel cross sections predict concentrations that are in excellent agreement with the ^{59}Ni measurements. Consequently, uncertainties in the nickel cross sections cannot explain the discrepancy between the helium measurements and calculations.

Other Possible Sources of Helium: Since we have demonstrated that the ^{59}Ni cross sections correctly predict the isotopic concentrations, the most probable explanation for the excess helium production at high neutron fluences is that a daughter or granddaughter isotope produced by transmutation from natural nickel may produce helium. Figure 7 shows a section of the table of isotopes surrounding nickel. The blank isotopes are stable, those shown in gray and pink are radioactive, and those shown in pink are the best candidates for an unknown source of helium or hydrogen. In order to compete with the ^{59}Ni reactions, a candidate isotope would need to have a significant thermal neutron (n,α or n,p) reaction.

Table 2. Measured and Calculated ^{59}Ni Content of Irradiated Ni in HFIR

Nickel Sample	Thermal Fluence, x10^{22} n/cm^2	Measured ^{58}Ni Atom%[a]	Measured ^{60}Ni Atom%[a]	Measured ^{59}Ni Atom%[a]	Calculated ^{59}Ni Atom%	^{59}Ni Ratio C/M
Natural	0	68.1	26.2	0		
JP15-42	6.14	53.2	34.2	2.59	2.66	1.03
JP12-24	8.05	48.8	37.1	2.46	2.48	1.01
JP15-41	10.21	44.9	39.0	2.26	2.28	1.01
JP12-39	10.70	43.8	39.6	2.19	2.24	1.02

[a]Measurements by thermal ionization mass spectrometry are accurate to $\pm$1%.

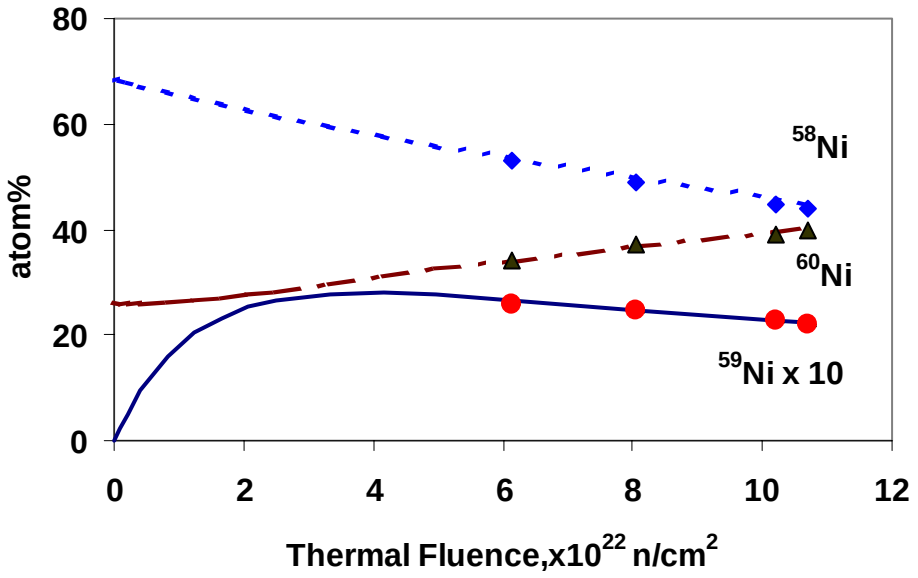

Figure 8. Comparison of measured and calculated nickel isotopic concentrations as a function of the thermal neutron fluence. Note that the ^{59}Ni values are multiplied times 10.

All known isotopes that have thermal neutron (n,α) or (n,p) cross sections lie on the proton-rich side of the line of stability on the Chart of the Nuclides. Furthermore, a candidate isotope must have a large positive Q-value for the reaction of interest, as shown in Table 3. These criteria lead to the selection of ^{55}Fe, ^{57}Co, ^{58}Co, and ^{65}Zn as the only possible candidates. All of the other radioactive isotopes in Figure 7 (besides ^{59}Ni) are either too short-lived or have unfavorable Q-values. ^{65}Zn is known to have a thermal neutron cross section for helium and most likely for hydrogen, as well. [7] However, the production of ^{65}Zn from nickel is much too small to explain the excess gas seen in our experiments. Similarly, ^{55}Fe is thought to have a small thermal (n,α) cross section of about 0.011 barns [8]; however, again the production of ^{55}Fe is not enough to explain the excess gas production. This leaves only ^{57}Co and ^{58}Co as reasonable candidates. The (n,α) Q-value is too low for ^{57}Co, although this isotope could be a source of additional hydrogen. ^{58}Co is known to have a very high (n,γ) cross section of 1900 barns and the Q-values are high enough that it could produce H and He, as well. However, the (n,α) and (n, p) thermal neutron cross sections would have to be very large in order to compete with the rapid elimination of ^{58}Co due to decay (78 day) and transmutation to ^{59}Co.

Table 3. Thermal Neutron Q-Values and Cross Sections

Isotope	(n,α) Helium Reactions		(n,p) Hydrogen Reactions	
	Q,MeV	Thermal σ,b	Q,MeV	Thermal σ,b
Ni-59	5.096	12.0	1.855	1.96
Zn-65	6.481	4.7	2.134	?
Fe-55	3.584	0.011	1.014	?
Co-58	3.511	?	3.089	?
Co-57	1.858	?	1.618	?

FUTURE WORK

Additional measurements are needed to determine the production of hydrogen and helium from nickel at high neutron fluences. The data in Figure 1 could be used to make an empirical correction to high fluence predictions, but only in the fluence range shown. In order to confidently predict helium production at much higher neutron fluences, a more detailed understanding of the reaction mechanisms will be required. If a daughter or granddaughter isotope produces the excess gas, then the effect may be very non-linear, as is the case for ^{59}Ni. Gas measurements are needed at higher neutron fluences, especially for separated nickel isotopes as well as daughter or granddaughter isotopes in order to explain the excess gas production that we have measured.

ACKNOWLEDGEMENTS

This work was supported by the U.S. Department of Energy, Office of Fusion Energy, under Contract DE-AC06-76RLO 1830. Pacific Northwest National Laboratory is operated for DOE by Battelle Memorial Institute. This work was also performed under the auspices of U.S. DOE by the University of California, Lawrence Livermore National Laboratory under contract N. W-7405-Eng-48.

REFERENCES

[1] L. R. Greenwood, *Journal of Nuclear Materials*, 115, pp. 137-142, 1983.

[2] L. R. Greenwood, D. W. Kneff, R. P. Skoronski, and F. M. Mann, *Journal of Nuclear Materials,* 123, pp. 1002-1010, 1984.

[3] B. M. Oliver, F. A. Garner, L. R. Greenwood, and J. A. Abrefah, High-Sensitivity Mass Spectrometer System for the Determination of Hydrogen in Irradiated Materials, *Journal of Nuclear Materials* 283-287, pp. 1006-1010, 2000.

[4] F. A. Garner, B. M. Oliver, L. R. Greenwood, D. J. Edwards, and S. M. Bruemmer, 10th International Conference on Environmental Degradation of Materials in Nuclear Power Systems, 2002; submitted for publication in *Journal of Nuclear Materials*.

[5] L. R. Greenwood and C. A. Baldwin, *Fusion Materials Semiannual Progress Report for Period Ending December 31, 1997*, DOE/ER-0313/23, pp. 301-304, 1998.

[6] Evaluated Nuclear Data File, Version VI, National Nuclear Data Center, Brookhaven National Laboratory.

[7] D. W. Kneff, L. R. Greenwood, D. W. Skowronski, and F. M. Mann, *Radiation Effects,* Vols. 92-96*,* pp. 553-556, 1986.

[8] L. R. Greenwood, D. G. Graczyk, and D. W. Kneff, *Journal of Nuclear Materials 155-157*, p. 1335, 1988.

11. MATERIALS ENGINEERING AND DESIGN REQUIREMENTS

No contributions.

12. IRRADIATION FACILITIES AND TEST MATRICES

No contributions.